In vivo Observation of the Release of Norepinephrine and *In Vivo* Optical Studies on the Direct and Indirect Paths of the Striatum

Samuel Clark

Submitted in partial fulfillment of the
requirements for the degree of Doctor of
Philosophy under the Executive
Committee of the Graduate School of
Arts and Sciences

COLUMBIA UNIVERISTY

2018

ABSTRACT

In vivo Observation of the Release of Norepinephrine and *in vivo* Optical Studies on the Direct and Indirect Paths of the Striatum

Samuel Clark

This thesis focuses on my work using optical techniques to study different brain regions *in vivo*. The ability to optically study neurons and the circuits they comprise in vivo is an important method to better understand their role in the healthy brain and their dysfunction in disease.

The first part of my thesis focuses on my work using on a collaborative project using a new optical probe to study norepinephrine synapses *in vivo*. In this work we were able to observe the effects of amphetamine on norepinephrine release *in vivo* and observed some evidence of potential silent synapses.

I also describe a new method of cranial window surgery I developed for optical imaging. This technique called PHASOR, is faster, and has a higher success rate, than traditional surgical methods. The improvements demonstrated in this new surgical technique may enable more widespread use of optical imaging methods.

In the second part of my thesis, I used optical techniques to study the dorsal striatum *in vivo* in awake behaving mice. The direct and indirect paths of the dorsal striatum play an important role in motor behavior and motor learning. Dysfunction in these paths has been implicated in motor diseases as well as in mood disorders. In this thesis, I provide a review of the anatomy and physiology of the neurons that comprise the dorsal striatum, and the circuits that they form. The next chapters describe my work using optical techniques to record from these neurons in vivo.

In my first set of experiments, I recorded from the direct and indirect paths during a behavioral task of anxiety and observed differential firing depending on the anxiety state of the mouse.

Finally, in a preliminary set of experiments, I record from the direct and indirect paths during tasks of motor learning. I found that both paths show changes in firing during motor learning and that these changes differ between the dorsolateral and dorsomedial striatum.

TABLE OF CONTENTS

LIST OF FIGURES

Acknowledgements

First, I would like to thank Dr. David Sulzer who has been an amazing mentor. He provided excellent support and always encouraged scientific curiosity. Dave has maintained an open door policy and has always been easy to approach and to discuss scientific projects at any time of the day. I appreciated Dave's flexibility, interest in my work, and invaluable input into all of the different ideas we discussed. I enjoyed working in Dave's lab and he has motivated me to develop my scientific creativity.

I would like to thank the members of my thesis committee, Drs. Steven Siegelbaum, Atila Losonczy, and Rui Costa for their extremely valuable advice that helped guide me through these projects. I would also like to thank the external member of the thesis committee, Dr. Mark Wightman for joining the committee and sharing his valuable expertise. I would also like to thank all of the undergraduate students in the Sulzer lab who helped contribute to the work described in this thesis. I would like to thank Dr. Timothy Chen and Dr. Clay Lacefield for providing me with invaluable help in analyzing the data in this thesis. Finally, I would like to thank Ellen Kanter from the Sulzer lab for helping manage the technical logistics and protocols necessary for these experiments.

Dedication

I would like to dedicate my dissertation to my family. The support and encouragement of my parents and three sisters has been invaluable in enabling me to pursue higher education.

PART 1: IN VIVO STUDY OF NOREPHINEPHRINE

CHAPTER 1: GENERAL INTRODUCTION TO NOREPINEPHRINE AND FFNS

OVERVIEW

In this chapter I provide a brief review of the role of norepinephrine (NE) in the CNS and its dysfunction in disease. I also introduce a new optical method to enable direct observation of release *in vivo*. The following chapters describe the collaborative studies I and other members of the Sulzer, Sames, and Kandel labs performed on this system. These studies provide the first optical observation of release *in vivo* and the first optical observation of the effects of amphetamine *in vivo*.

THE ROLE OF NOREPINEPHRINE

NE plays important roles in both the central nervous system (CNS) and peripheral nervous system (PNS). It is synthesized from dopamine (DA) by DA beta hydroxylase (DBH). In the cortex and hippocampus, NE modulates cognitive functions including working memory, attention, decision making, and sensory processing (Mehta et al. 2001, Clayton et al. 2004, Sara 2009). The major CNS population of neurons that release NE reside in the locus coeruleus (LC) in the brain stem and project to both cortical and subcortical areas, and can release DA as well as NE (Berridge and Waterhouse 2003, Kempadoo et al. 2016).

NE signals through three major G-protein coupled receptors, known as alpha 1, alpha 2, and beta receptors. Alpha 1 receptors are located post synaptically and increase calcium influx through Gq signaling, while alpha 2 receptors are chiefly located presynaptically and function as auto receptors to reduce NE release (Nguyen et al. 2017). The neurons of the LC exhibit tonic firing that modulate arousal levels and wakefulness. In response to salient stimuli, the LC neurons display phasic bursting (Berridge and Devilbiss 2011). NE released through phasic bursting plays an important role in attention through actions in the prefrontal cortex (PFC). Rodent studies of lesions of the NE projections to the PFC have shown deficits in cognitive processing. In primates, reduced NE release by application of an alpha 2 agonist impairs attention and working memory (Ramos and Arnsten 2007).

Both DA and NE play important roles in modulating attention through activity at the PFC (Campo et al. 2011). NE and the NE transporter (NET) work to modulate DA signaling and attention. Interestingly, DA binds to the NET transporter with a higher affinity than to the DA transporter DAT. In the PFC, there are very low levels of DAT and high levels of NET that modulate extracellular DA levels (Moron et al. 2002). In addition, the enzyme catechol-o-methyltransferase (COMT) breaks down DA in the PFC (Scheggia et al. 2017). Thus, DA signaling is regulated by both COMT mediated breakdown as well as by NET mediated reuptake.

NOREPINEPHRINE DYSFUNCTION IN DISEASE

NE dysfunction plays an important role in the cognitive deficits of several disorders. Parkinson's disease is characterized by the loss of DA neurons in the substantia nigra pars compacta (SNc), resulting in the loss of the nigrostriatal DA path. This results in changes in output of the medium spiny neurons of the dorsal striatum and severe motor deficits (Hoehn and Yahr 1967, Dickson et al. 2009). However, Parkinson's disease also results in severe cognitive deficits such as impairment in attention, working memory, and cognitive flexibility (Halliday et al. 2008, Leverenz et al. 2009). These cognitive symptoms can precede the motor symptoms by many years (Keri 2010). In addition to the loss of dopaminergic neurons, there is also substantial loss of the NE neurons of the LC (Sulzer and Surmeier 2013). It is thought that the loss of the NE neurons projecting to the frontal cortex plays a significant role in the cognitive symptoms of Parkinson's disease (Vazey and Aston-Jones, 2012).

Individuals with genetic DBH deficiency from birth possess normal NE receptors, but lack the ability to synthesize NE. This results in problems with the autonomic nervous system and symptoms such as hypotension and dizziness. Interestingly, cognitive tests in DBH deficient individuals have not found any cognitive deficit. This suggests that if NE is absent from birth, other neurotransmitter systems are able to completely compensate in cognitive processing (Jepma et al. 2011).

Attention deficit hyperactivity disorder (ADHD) is the most common childhood mental disorder affecting, 5% of children in the US (Danielson et al. 2017). One of the most commonly prescribed first line treatments is amphetamine (AMPH) (administered as Dexedrine or Adderall), a stimulant with both therapeutic effect and a high potential for abuse and addiction. While amphetamine's potential for abuse

is dependent on its action on the dopaminergic synapses of the striatum, it also exerts potent actions at noradrenergic synapses of the cortex.

NOREPINEPHRINE AND AMPHETAMINE

It has been hypothesized that AMPH's ability to increase cortical levels of NE and, indirectly cortical DA, is due to actions at the NE transporter (NET), and that this may underlie much of its therapeutic effect for ADHD (Berridge and Devilbiss 2011, Campo et al. 2011) in a manner independent from its effects on striatal DA levels.

The mechanism by which AMPH increases DA levels has been extensively studied. The major mechanism by which AMPH raises DA levels is by redistributing vesicular DA to the cytosol, followed by reverse transport of cytosolic DA through DAT, and to more controversially, by causing vesicular fusion, as well as blocking reuptake through DAT and NET (Sulzer 2011). Despite its widespread therapeutic use, the mechanism by which AMPH raises cortical levels of NE is controversial. This controversy led a recent review (Berridge and Devilbiss 2011) to conclude that at clinically relevant concentrations, AMPH only increases NE levels by reuptake blockade, and that only very high concentrations can AMPH cause NE release. In contrast, other studies show that AMPH responses in vivo are consistent with driving NE release. The effects of AMPH occur quickly and increase NE levels far beyond traditional NE uptake blockers (up to 450%) followed by a rapid decrease (Heal et al. 2013).

This controversy spans several decades. In one of the first studies of the mechanism of AMPH on NE, Raiteri (1975) used radiotracers to show that AMPH had little effect on NE release compared to DA. They concluded that reuptake block was amphetamines primary mechanism by which it increases NE, while AMPH acts on DA terminals to both inhibit reuptake as well as to stimulate release.

Kuczenski and Segal (1992), used in vivo microdialysis to show that AMPH causes an increase in NE at dosages of 2.5mg/kg. They conclude that this may be mostly due to reuptake block and possibly release, but only at very high dosages. Florin (1994) used microdialysis in rats to measure NE levels. They administered clonidine, an alpha2 receptor agonist, and AMPH to examine AMPH induced increases in NE. They concluded that at 0.5mg/kg, clonidine reduced NE neuronal firing, and that AMPH-induced

increase in NE levels was dependent on AMPH blockade of reuptake. In contrast, higher dosages of 5.0 mg/kg were not sensitive to clonidine, and they concluded that AMPH caused NE release from vesicular storage sites at these concentrations. In contrast, Rothman (2001) used in vitro measurement of radiolabeled NE in synaptosomes prepared from rat caudate tissue. By administering AMPH in the presence and absence of reserpine, they found that AMPH caused NE release. However, these in vitro results were not verified *in vivo*.

FLUORESCENT FALSE NEUROTRANSMITTERS

Many of the mechanisms governing NE release and the action of AMPH have not been addressed *in vivo* due to previous limitations of *in vivo* tools for imaging neurotransmission (NT) (**Figure 1**). FFNs are fluorescent substrates for the catecholamine/serotonin vesicular transporters (VMATs), and for some FFNs including FFN270, for DAT and NET. FFNs including 270 are thus accumulated into the presynaptic synapse and loaded into synaptic vesicles. When concentrated in the vesicle, they fluoresce brightly, providing a means for visualization of their accumulation into the presynaptic bouton. When vesicle fusion occurs, the FFNs are released into the synaptic cleft and diffuse from the synapse, causing destaining of the bouton. This allows imaging of NT from dopaminergic and noradrenergic synapses in real time (Gubernator et al. 2009). The use of FFNs overcomes several limitations common to other *in vivo* techniques. For instance, *in vivo* microdialysis provides a bulk measurement of the overall sum of synaptic release and reuptake in an area over a slow time frame (typically > 20 min per sample). While cell-based neurotransmitter fluorescent engineered reporters (CNiFERs) have rapid response times, they provide a summed measurement of DA or NE in the area of the implanted reporter cell (Muller et al., 2014). Cyclic voltammetry *in vivo* may measure release of hundreds of synapses and therefore does not allow for single synapse resolution, nor can it distinguish between DA and NE, both of which are present in the mPFC. Finally, calcium indicators (GCaMPs and GECIs) provide a measure of cell firing rate, and an indirect measure of calcium transients in axon terminals, but do not show the kinetics of synaptic vesicle fusion and neurotransmitter release (Chen et al. 2013).

While FFNs have been used in acute brain slice preparations (Rodriguez et al. 2013, Pereira et al. 2016), their use *in vivo* is a novel application. In this research project, I optimized the use of fluorescent false

neurotransmitters (FFNs) *in vivo* and have characterized AMPH-induced release of DA and NE in wild type (WT) mouse cortex. Here we report the first in vivo optical observation of synaptic vesicle exocytosis in the mammalian brain, as well as a means to determine AMPH's action at noradrenergic synapses with single synapse resolution.

Technique	Single synapse resolution?	Realtime kinetics?	Real measure of synaptic vesicle fusion?
In vivo microdialysis	✗	✗	✓
2P Calcium imaging	✓	○	✗
2P Voltage indicators	✓	○	✗
In vivo Cyclic voltammetry	✗	✓	✓
Cnifers	✗	○	✓
MRI/SPECT/PET	✗	✗	○
FFNs	✓	✓	✓

Figure 1. Limitations of different *in vivo* imaging techniques. *In vivo* microdialysis measures a signal from numerous synaptic sites and at best has a temporal resolution of minutes. Multiphoton calcium imaging has single synapse resolution but measures calcium as a proxy for neuronal activity. Similarly, voltage indicators do not measure actual synaptic vesicle fusion. In vivo cyclic voltammetry does not have single synapse resolution. Cnifers signal from multiple synapses and lack real time kinetics. Other imaging methodologies such as MRI, SPECT, and PET measure activity over large brain regions. Only FFNs can resolve single synapses with real time kinetics. Because they are released when vesicles fuse, they have the potential to measure vesicle fusion.

CHAPTER 2: PRELIMINARY AND CONTROL STUDIES WITH FFNS

OVERVIEW

In this chapter, I describe several preliminary experiments that I performed to optimize the technique of using FFNs *in vivo*. Because FFNs had not previously been used in vivo, there were a number of preparations that were necessary to optimize this novel system.

FFN LOADING

FFN270 can be loaded into the brain through a chronic implanted optical glass window**.** For this set of experiments, I used the novel FFN, FFN270. This new FFN was designed to have a high specificity as a substrate for the NE transporter (NET). The first step to optimize FFN270 for use in vivo was to develop an optimal method by which they could be introduced into the brain tissue prior to imaging. Multiphoton

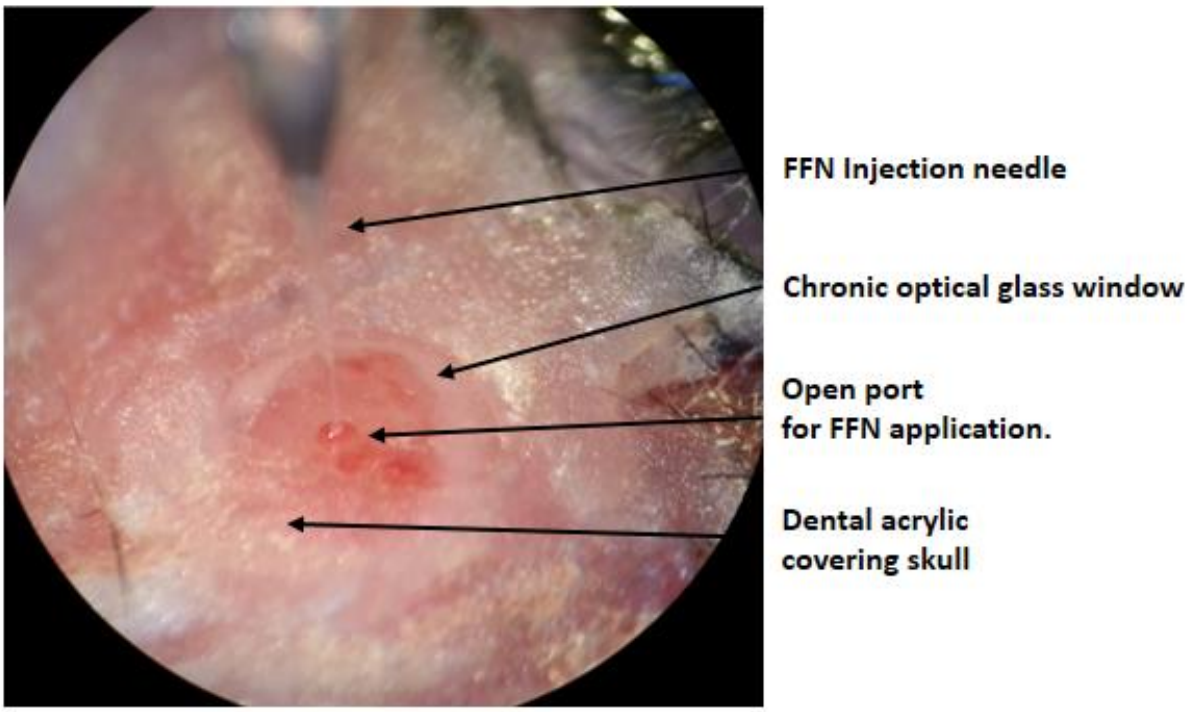

Figure 2. Diagramed image of an implanted cranial window with a chronic glass port for nanoinjecting FFN. The FFN injection needle is lowed through the open port in the optical glass window allowing loading of the FFN. The window is affixed to the skull with dental acrylic.

imaging through a cranial window often uses a surgically implanted glass coverslip. However, this coverslip would impair the loading of the FFN via nanoinjection into the tissue. This problem was solved by using a diamond tipped drill bit to bore a hole into the cranial window glass coverslip. This allowed the FFN to be loaded through the microwindow into the brain tissue (**Figure 2**). The hole in the cranial window was then plugged with silicone glue that could be removed allowing reloading of the FFN at different time points and chronic imaging experiments.

Novel fluorescent cocaine analogue ECN127 pretreatment blocks loading of FFN270

The next *in vivo* experiment was conducted in collaboration with members of the Sames lab. We performed a control experiment to verify that loading of the FFN could be blocked by pretreatment with a NET inhibitor. We nanoinjected FFN270 twenty minutes after we first pre-injected a fluorescent NET antagonist ECN127 (**Figure 3**). This control allowed realtime visualization of the specificity of FFN270 for NET, allowing us to visualize if FFN270 would load into the puncta through other mechanisms that were not mediated by NET. ECN127 is a rhodamine fluorophore linked to a tropane analog of cocaine. The resulting compound is a fluorescent DAT/NET inhibitor. We found that pretreatment with ECN127 blocked FFN270 loading (**Figure 4**). This confirmed specificity of FFN270 loading to NET.

Targeting the LC with a viral vector

Finally, we performed an experiment to verify that we could target the LC with a viral vector. In a later experiment channelrhodopsin was injected into the LC and we released FFN270 from the cortex with optical stimulation. The details of the channelrhodopsin experiment are described in chapter 3. In this preliminary experiment we injected AAV virus expressing a hemagglutinin (HA) tag. We then performed immunostaining against tyrosine hydroxylase (TH) and hemagglutinin to double label the brain sections and verify expression of the virus in the LC. We found that we were able to successfully target the LC and achieve 40% colocalization with TH (**Figure 5**).

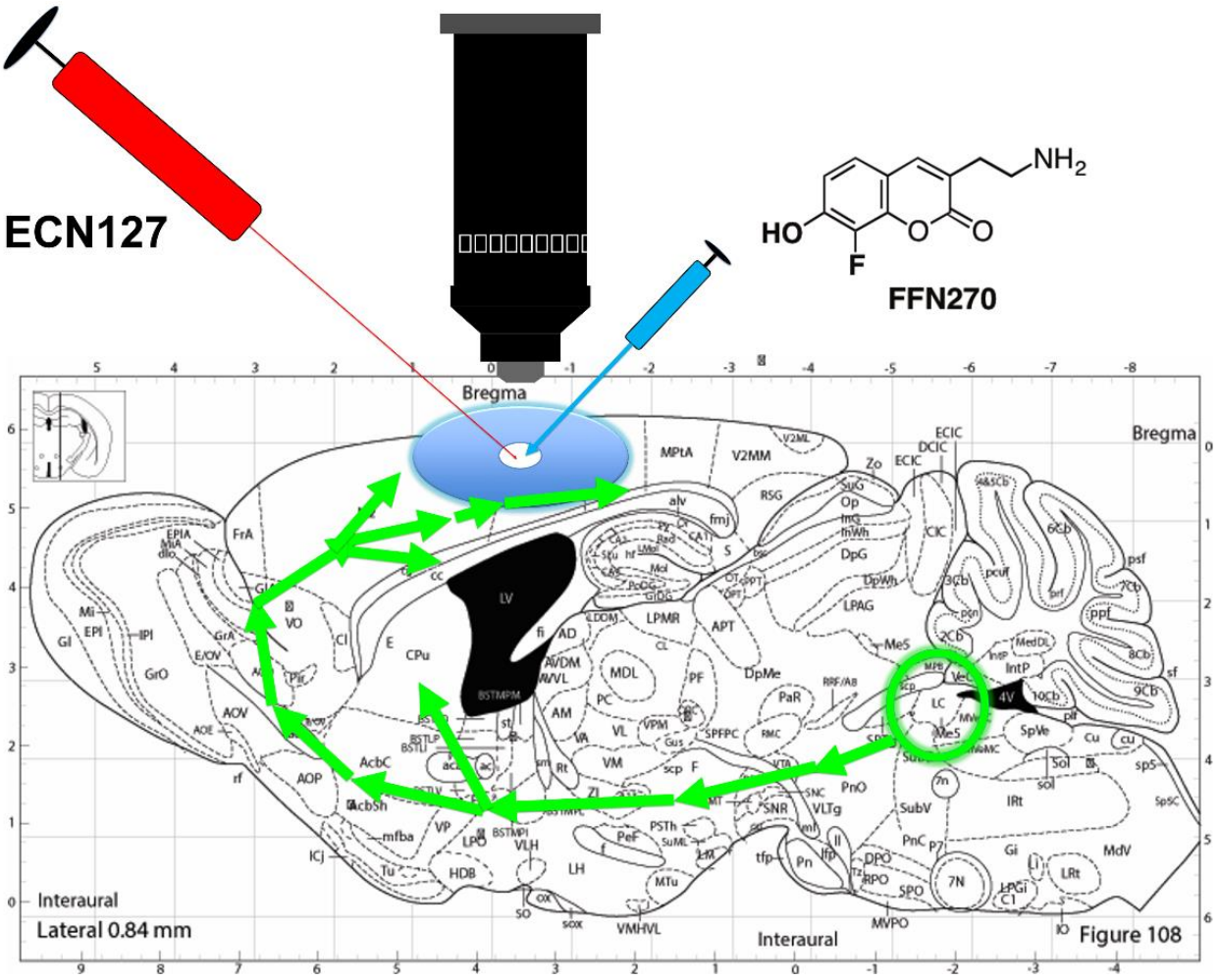

Figure 3. Diagram of ECN127 experiment. The NE projections to the cortex from the LC are shown in green. A cranial window was performed an ECN127 was injected into the cortex prior to FFN270. (modified from the Mouse Brain Atlas, Panxinos and Franklin 2001).

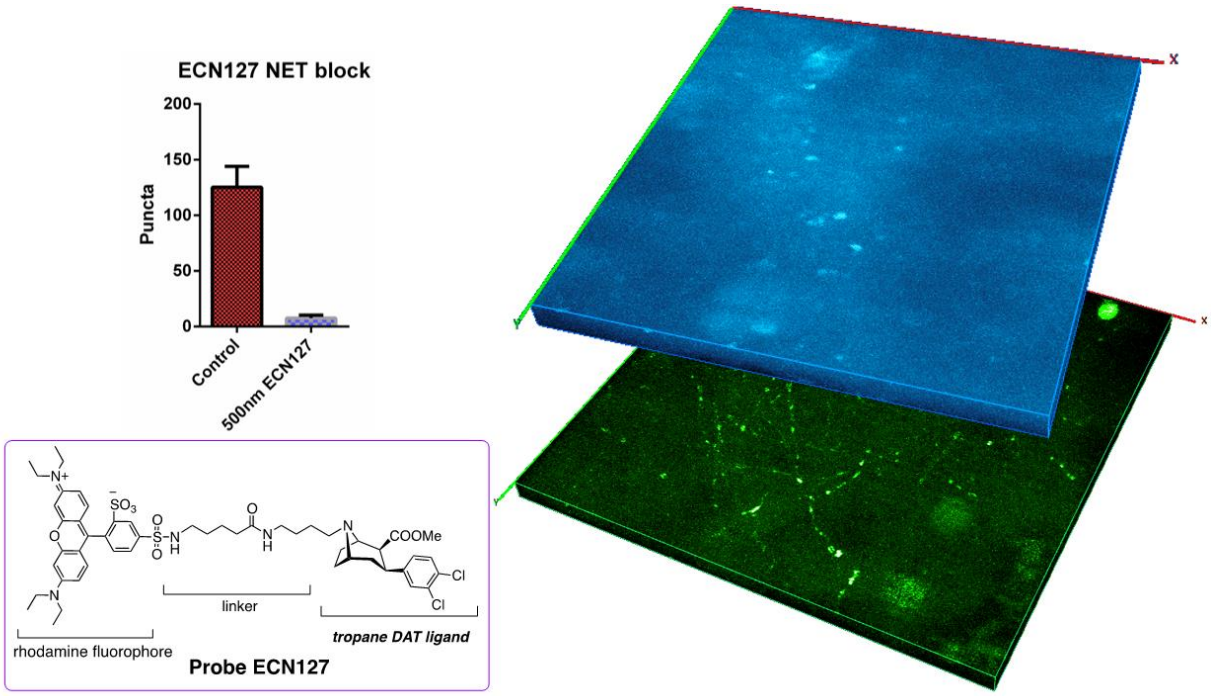

Figure 4. Pretreatment with NET inhibitor ECN127 blocks FFN270 loading. Pretreatment with ECN127 results in fewer visualized FFN270 puncta than a control animal injected with only FFN270 (top left). Brain tissue injected with ECN127 (blue 3D projection) shows very few puncta. In contrast, brain tissue injected with only FFN270 shows significant amounts of puncta (green 3D projection). ECN127 is comprised of a rhodamine fluorophore linked to a tropane DATA/NET ligand (bottom left).

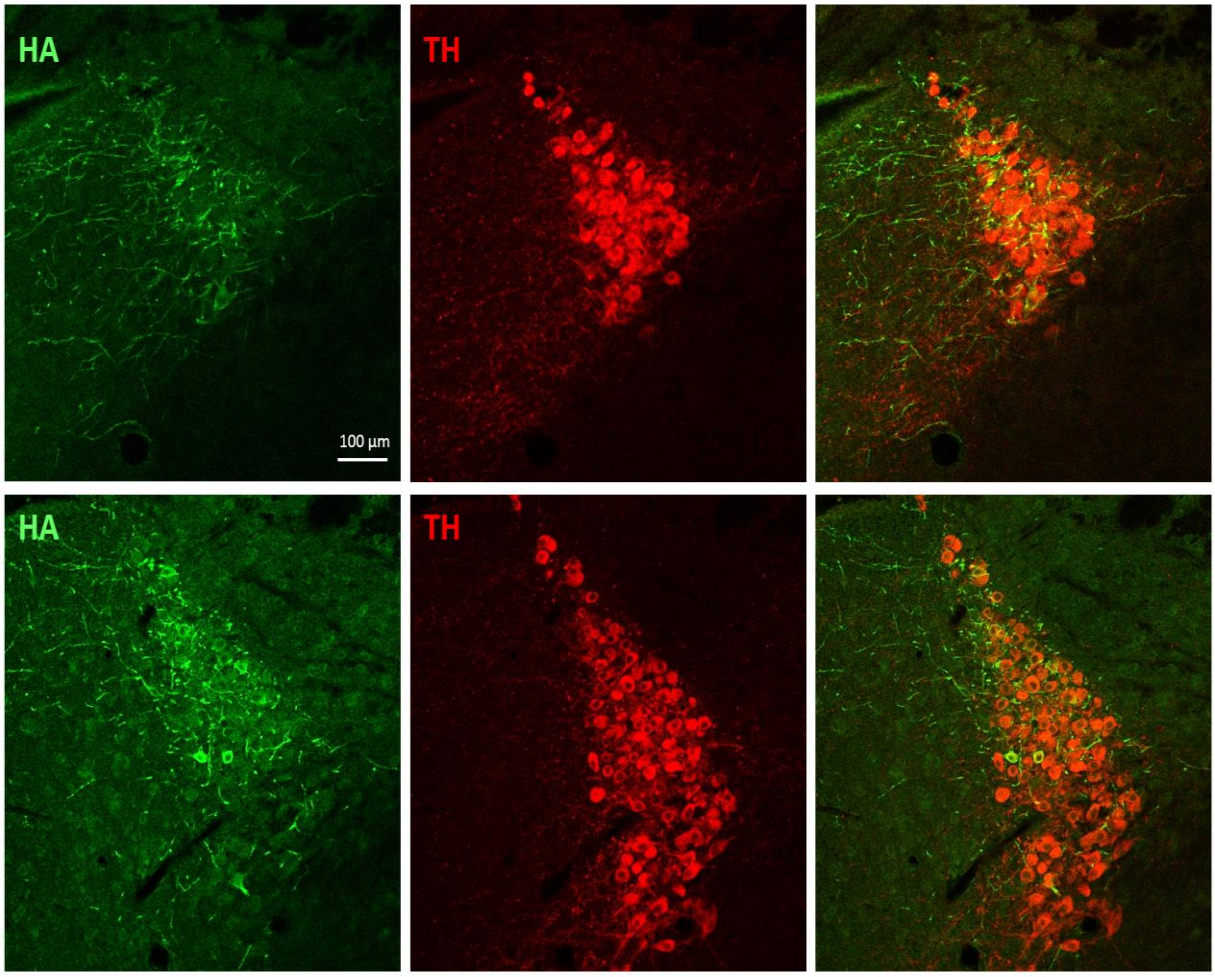

Figure 5*.* Immunostaining of viral injection into the LC. A viral vector expressing the epitope HA was injected into the LC. Six weeks post injection, the mice were perfused and the brain was sectioned. Sections were immunostained for HA (left) and TH (middle). The right panels show the overlap between the two signals. We found approximately 40% colocalization between HA and TH (right).

METHODS

Mice

Adult 8 week old male wild type C57BL/6J mice were used for the imaging experiments here. . All procedures were conducted in accordance with Institutional Animal Care and Use Committee (IACUC) of the New York State Psychiatric Institute.

Cranial window surgery

Mice were anesthetized with isoflurane (1-4%). The depth of anesthesia was monitored by both the animal's response to toe-pinch every 5 min and observation of respiratory rate. Once the proper depth of anesthesia was reached, the animal was placed in a small animal stereotactic apparatus on top of a heating pad and Puralube vet ointment was applied to the eyes to prevent vision loss. All surgical procedures were performed in a sterile manner. Marcaine (0.5%) with saline 1:2 (0.25%) (2 mg/kg), was injected subcutaneously along the midline of the scalp as a local anesthetic. Before the incision, the hair over the scalp area was removed with NAIR and sterilized with a gentle scrub with Betadine on a sterile cotton swab, followed by 70% ethanol, repeated 3 times. The scalp was then removed with surgical scissors, membranes over the skull were removed by scraping, and the exposed bone was dried with compressed air. A 3 mm cranial imaging window was then made over the barrel cortex with a high speed dental drill (Midwest Stylus 360). The meninges were inspected to make sure there was no damage. Any bleeding from the bone was stopped with an application of collagen foam (Avitene Ultrafoam, Bard Davol). A cranial window with a microinjection port was then affixed over the window with dental acrylic. A glass pipette attached to a Nanoject II (Drummond Scientific) was filled with a 1 500nnM solution of ENC127 and was then injected through the microinjection port in the cranial window into the brain at coordinates AP: -0.9 mm to -1.0 mm and ML: 3.0 mm, over several depths (DV: 100 µm, 50µm, and 20 µm) with 3 minutes of delay per depth. After 30 minutes, 100 nl of 1mM solution of FFN270 diluted in ACSF was then injected into the same coordinates. The glass pipette was then withdrawn from the brain and the mouse was then injected with ketamine (100 mg/kg) and xylazine (10 mg/kg) i.p. and then weaned off of isoflurane while making sure to maintain depth of anesthesia. The mouse was then

headfixed under the multiphoton microscope for imaging. The body temperature of the mouse was maintained for the duration of imaging with a heating pad.

Viral injection surgery

Mice were injected with buprenorphine (0.05- 0.1 mg/kg) prior to anesthesia and anesthetized with isoflurane (1-4%). Marcaine diluted 50% in saline was injected under the scalp to provide local anesthetic. The body temperature of the mouse was maintained for the duration of imaging with a heating pad. The depth of anesthesia was monitored by both the animal's response to toe-pinch every 5 min and observation of respiratory rate. Once the proper depth of anesthesia was reached, the animal was placed in a small animal stereotactic apparatus on top of a heating pad and Puralube vet ointment was applied to the eyes to prevent vision loss. All surgical procedures were performed in a sterile manner. Marcaine (0.5%) with saline 1:2 (0.25%) (2 mg/kg), was injected subcutaneously along the midline of the scalp as a local anesthetic. Before the incision, the hair over the scalp area was removed with NAIR and sterilized with a gentle scrub with Betadine on a sterile cotton swab, followed by 70% ethanol, repeated 3 times. The scalp was then removed with surgical scissors, membranes over the skull were removed by scraping, and the exposed bone was dried with compressed air. A 1 mm hole was then made over the dorsal striatum with a high speed dental drill (Midwest Stylus 360). Any bleeding from the bone or dura was stopped with an application of collagen foam (Avitene Ultrafoam, Bard Davol). A glass pipette attached to a Nanoject II (Drummond Scientific) was filled with AAV virus expressing hemagglutinin (300 nl of 10^{13} viral units/ml), and attached to the stereotax. A volume of 300ul of virus was injected into the LC with 3 minutes of delay per depth. The glass pipette was then withdrawn from the brain and the scalp was sutured closed. The mouse was then transferred to a heated cage to recover.

Immunohistochemistry

Brain tissue preserved with paraformaldehyde was cut into 100um sections on a vibratome. Immunohistochemistry was performed as described in Clark et al. 2017.

Discussion

We found that FFN270 could successfully be utilized to study NE terminals in the mouse barrel cortex *in*

vivo through a cranial window. We also found that FFN270 labeling of puncta could be blocked by pretreatment with a novel fluorescent DAT/NET antagonist. Finally, we were able to successfully transfect the LC with an AAV viral vector, which is the first step before attempting viral transfection with channelrhodopsin expressing viruses. The experiments described here formed the basis for the more advanced studies described in the following chapter. Through this preliminary work, we were able to introduce FFN270 into an in vivo system and perfect the technique.

Chapter 3: Design of a Norepinephrine Optical Tracer for Imaging Individual Noradrenergic Synapses and Their Activity *in vivo*

Matthew Dunn*,[1] Adam Henke*,[1] Samuel Clark*,[2,3,4] Yekaterina Kovalyova,[1] Kimberly A. Kempadoo,[5] Richard J. Karpowicz, Jr.,[1] Eric R. Kandel,[3,5,6,7] David Sulzer†,[2,3,4] Dalibor Sames†[1]

*** These authors contributed equally.**

†Corresponding authors: ds43@columbia.edu and sames@chem.columbia.edu

[1] Department of Chemistry, Columbia University, New York, NY 10027, USA.

[2] Department of Neurology, Columbia University, New York, NY 10032, USA.

[3] Department of Psychiatry, Columbia University, New York, NY 10032, USA.

[4] Department of Pharmacology, Columbia University, New York, NY 10032, USA.

[5] Department of Neuroscience, Columbia University, New York, NY 10032, USA.

[6] Kavli Institute for Brain Science, New York, NY 10032, USA.

[7] Howard Hughes Medical Institute, New York, NY 10032, USA.

ABSTRACT

NE is a monoamine neurotransmitter with a wide repertoire of physiological roles in the peripheral and central nervous systems. Despite major strides in understanding the noradrenergic system, there are no experimental means to study functional properties of individual noradrenergic synapses in the brain. As learning and behavior adaptation depend on the ability of specific synapses to undergo changes in transmission efficiency, development of new approaches for imaging synaptic neurotransmission is of

fundamental importance. Here we introduce fluorescent false neurotransmitter 270 (FFN270), an organic dye-based tracer of NE that integrates key structural features of NE with the coumarin fluorophore. FFN270 is a fluorescent substrate of the NE transporter and vesicular monoamine transporter, and thus labels noradrenergic neurons and their synaptic vesicles. FFN270 enables imaging of synaptic vesicle content release from single release sites in living rodents. Combining FFN270 imaging and optogenetic stimulation, we found heterogeneous release properties of noradrenergic synapses in the somatosensory cortex, identifying populations of low and high releasing synapses. We also observed rapid release of synaptic vesicle content induced by systemic AMPH administration, yielding insight into the drug's effect on cortical noradrenergic synapses.

INTRODUCTION

NE is the major neurotransmitter of the sympathetic peripheral nervous system and regulates most visceral organs and glands, thermoregulation, and the immune system NE is also a key neurotransmitter in the central nervous system (CNS) (Wassall 2009). Brain NE neurons primarily originate in the locus coeruleus (LC) and project axons throughout the CNS, including to the cortex, hippocampus, hypothalamus, amygdala, cerebellum, and spinal cord (Fig. 1C) (Foote et al 1983, Schroeter et al. 2000, Berridge and Waterhouse 2003 Accordingly, the NE system plays numerous physiological roles, such as brain-wide regulation of neurovascular coupling and cerebrospinal fluid flux (Bekar 2012), and local effects such as modulation of cortical neuronal circuitry (Sara 2012).

While it is well established that the LC-NE system regulates stress responses, arousal, and sleep-wake cycles, more recent reports also suggest specific functions in cognition (Sara 2007, Sara and Bouret 2012). Shifts in LC neuronal firing between tonic and phasic activity control decision-making processes and facilitate optimization of behavior in a changing environment. In the "adaptive gain and behavior optimization hypothesis," LC neuronal firing controls the balance between exploitation of the ongoing task versus exploration of new ones (Aston-Jones and Cohen 2005) NE synaptic inputs reset the activity states and firing patterns of ensembles of cortical neurons, presumably by modulating the responsiveness of these cells via activation of adrenergic receptors (Sara and Bouret 2012).

The NE system has also been implicated in numerous neurodegenerative and psychiatric disorders. For example, in Parkinson's disease, degeneration of LC-NE neurons often precedes loss of DA neurons in the substantia nigra; (Vazey and Aston-Jones 2012) in Alzheimer's disease, the most extensive loss of sub-cortical neurons occurs in the LC (Zarow et al. 2003, Braak and Del Tredici 2011, Iba et al. 2015). Modulators of NE neurotransmission represent an important class of widely used therapeutics, including adrenergic receptor agonists/antagonists, and modulators of NE storage, release, and reuptake. For example, the antidepressant mirtazapine is an α2 receptor blocker, and the antidepressant reboxetine is an inhibitor of the plasma membrane NE transporter, NET (Moret and Briley 2011, Zhou 2004). AMPH, presently administered under the tradename Adderall, is used for treating attention deficit hyperactivity disorder (ADHD) (Zhour 2004), and is prescribed to hundreds of thousands of children in the US, and self-administered by millions worldwide (Degenhardt and Hall 2012). AMPH enhances NE (and DA) transmission (Amara 1998, Rothman and Baumann 2003, Ventura et al. 2003), although, whether the effects are due to NET inhibition or the redistribution of stored NE content (e.g. via reverse transport) at physiological concentrations has long been debated (Rothman et al. 2001, Spencer 2015). However, despite the growing importance of the LC-NE system, there previously have been no experimental tools to study NE release at the level of discrete synapses, and thus the release properties of sparse cortical NE axons and synapses *in vivo* remained unknown.

The synaptic hypothesis of learning – which posits that ongoing alteration of synaptic transmission underlies an organism's ability to learn and change behaviors – is gathering experimental support (Nabavi 2014). Further, even individual synapses formed by the same axon (Bamford et al. 2004), are presumably regulated by ongoing expectation and experience to be more or less likely to participate in subsequent neurotransmission. To determine how behavior and sensory input alter specific synapses, novel tools to measure neurotransmission at individual synapses *in vivo* must be developed and implemented.

The current approaches for measuring NE lack the spatial and temporal resolution to discern individual synapses in the living brain. While electrochemical detection can distinguish DA from NE in some contexts (Park et al. 2011, Bian et al. 2010, Lu et al. 2004), these approaches have insufficient

spatial resolution to detect NE release from individual synapses (Sames et al. 2013), and are not useful in sparsely innervated regions of the CNS like the neocortex (Herr et al. 2012). New fluorogenic cell-based sensors can detect changes in the cortical NE *in vivo* with high sensitivity; however, these approaches also lack the spatial resolution to distinguish individual synapses (Nguyen et al. 2010, Muller et al. 2014). Fluorogenic receptor-based sensors have been developed to selectively detect glutamate concentration changes in the brain with single synapse resolution (Marvin et al. 2013, Namiki et al. 2007, Okubo et al. 2010, Hires et al. 2008), but similar sensors for monoamine neurotransmitters have not yet been developed. Chemical labels can be used for detection of NE with adequate spatial resolution, such as glyoxalic-acid-induced fluorescence histochemistry in fixed tissues (Carelsson et al. 1962, Lindvall and Bjorklund 1974) and more recently, fluorogenic chemosensors that react with NE in large dense core vesicles of cultured cells(Secor and Glass 2004, Hettie et al. 2013), but these techniques have not been adapted to living tissue.

Here we introduce the use of the fluorescent false neurotransmitter (FFN) concept to provide an optical tracer of NE neurotransmission (Gubernator et al. 2009). Several generations of fluorescent DA mimetics have been developed in our laboratories, which revealed the heterogeneous nature of dopaminergic presynaptic activity in mouse brain tissue (Rodriguez et al. 2013, Pereira et al. 2016). FFN102 is an exemplar dopaminergic FFN (Fig. 6), deriving its labeling selectivity for dopaminergic neurons as a substrate of the plasma membrane DA transporter (DAT) (Rodriguez et al. 2013, Lee et al. 2010). As shown below, however, FFN102 is not a substrate for the NET, and thus a poor optical tracer for NE.

We now expand the scope of the FFN concept by introducing the first NE-FFN, probe FFN270 (Fig. 6). This compound is designed as a fluorescent NET substrate and also a substrate of the neuronal vesicular monoamine transporter (VMAT2), the transporter responsible for packaging neurotransmitter in monoaminergic synaptic vesicles. The probe is taken up along with NE into synaptic vesicles within NE axonal varicosities and enables measurement of synaptic vesicle content release by destaining during exocytosis. FFN270 enables both an examination of noradrenergic microanatomy and an observation of synaptic activity in the cortex of intact neuronal circuits *in vivo*. The use of FFN270 also demonstrated

that exposure to pharmacologically relevant concentrations of AMPH has a dramatic effect on cortical NE axons, providing new insights to the drug's mechanism of action.

METHODS

Synthesis and Preparation of NE-FFN Leads

Detailed synthetic routes and confirmation of compound identities is included in *Supplementary Information*.

Photophysical Characterization and Measurement of log D values

General – Photon absorption and emission spectra were measured using a BioTek H1MF plate reader on bottom read mode.

Absorption - UV absorption spectra were taken by adding probe (4 µL of 10 mM stock solution in DMSO) to 996 µL of PBS buffer at different pH values (final probe conc. = 40 µM) in a clear-bottom white 96-well plate.

Emission/Excitation - Excitation/emission spectra were taken by adding probe (5 µL of 40 µM solution in PBS) to 995 µL of PBS buffer of different pH values (final probe conc. = 0.2 µM) in a clear-bottom white 96-well plate.

pK_a - The pK_a values of probes were determined from the absorption spectra. The absorbance $\lambda_{abs,\,max}$ of the red-shifted peak was plotted versus pH of the PBS solution; the data were fit to a sigmoid curve using GraphPad Prism 5 software to determine the pK_a value.

log D - The log *D* values were determined by a traditional shake flask method. Each measurement was performed in duplicate as follows. First, 20 µM probe solution in 1 mL PBS (pH 7.4) was prepared to which 1 mL of *n*-octanol was added and mixed thoroughly. The mixture was kept in dark for 3 days for complete equilibrium, and the concentrations of probe in each layer were determined based on the UV absorbance. Log *D* values were determined based on the following equation; log $D = \log[\text{probe}]_{oct} - \log[\text{probe}]_{PBS}$, where $[\text{probe}]_{oct}$ and $[\text{probe}]_{PBS}$ are the concentrations of the probe in *n*-octanol and PBS, respectively.

Characterization and Measurement of probe uptake in transfected cell culture

Fluorometric assay for evaluation of hNET substrate activity

Stably hNET-transfected HEK cells were seeded at a density of 0.08-0.09 x 10^6 cells/well in white solid-bottom 96-well plates and allowed to proliferate in growth medium for ~2 days at 37 ºC to reach confluence. On the day of the experiment, the complete growth medium was aspirated, wells were washed with 200 µL PBS, and treated with 100 µL experimental medium with DMSO (vehicle, 0.02% v/v) or nomifensine (2µM). The cells were incubated for 60 min at 37 °C, and experimental compounds (100 µL /well of 10 µM solution in experimental medium with DMSO (vehicle) or nomifensine 2µM) was added for a final concentration of 5µM compound in wells. Cells were then incubated for 30 min at 37 ºC. The experiment was terminated by two rapid PBS washes (200 µL/well) followed by addition of fresh PBS buffer (120 µL/well). The fluorescence uptake in cells was immediately recorded using a BioTek H1MF plate reader (3x3 area scan, bottom read mode) with excitation and emission wavelengths set at 370 nm and 460 nm respectively.

Quantification of hNET substrate activity

Substrate activity was determined using signal to basal ratio (S/B): mean fluorescence uptake (with DMSO vehicle) divided by that in the presence of nomifensine. Data presented as normalized uptake ± SEM from three independent experiments (eight separate measurements per condition per experiment).

Fluorescence microscopy imaging of probes in hNET-HEK cells

hNET-HEK cells or their respective controls, HEK293, were plated onto poly-D-lysine (Sigma Aldrich, conc. = 0.1 mg/mL) coated clear bottom six-well plates at a density of 0.15-0.20 x 10^6 cells per well and grown at 37° C in 5% CO_2. Following ~4 days of growth, the cells had reached 80-90% confluence. The culture medium was removed by aspiration, and the cells were washed with PBS (Invitrogen, 1.0 mL/well). To investigate the inhibitory effects of nomifensine maleate salt (Sigma-Aldrich) and cocaine hydrochloride salt (Sigma-Aldrich) on probe uptake, cells were incubated in 0.9 mL of experimental media containing the inhibitor (2 µM prepared from 10 mM stock solution in DMSO) or DMSO vehicle as a control at 37° C in 5% CO_2 for 1 h. The compound uptake was initiated by adding 0.1 mL of experimental media containing probe (200 µM, prepared from a 10 mM stock solution in DMSO, with a final probe

concentration of 20 µM in the uptake assay) with and without nomifensine (2 µM) or cocaine (1 µM). Following incubation at 37° C in 5% CO_2 for 30 min, the media was removed by aspiration and the cells were washed with PBS (1 mL/well) and maintained in fresh experimental media (1 mL/well). Fluorescence images (at least 3 images/well in duplicate wells) were acquired with a Leica FW 4000 imaging system (Leica Microsystems) equipped with a Chroma custom filter cube (ex = 350 ± 25 nm, em = 460 ± 25 nm; Chroma Technology Corporation) and a Leica DFC-360FX camera. Fluorescence and bright field images were acquired with exposure time set at 600 ms and 37 ms respectively. All images were adjusted using the same contrast and brightness level using ImageJ software (National Institutes of Health).

Fluorescence microscopy imaging of probes in VMAT-HEK cells

Epifluorescence microscopy of the small library of experimental coumarins reported here was conducted as previously reported using VMAT-HEK and control tetR-HEK cells. Briefly, VMAT-HEK and TetR-HEK cells were plated at a density of 0.15-0.20 x 10^6 cells per well on poly-D-lysine coated 6-well optical plates (Falcon) and grown at 37° C in 5% CO_2. Following ~4 days of growth, the cells had reached 80-90% confluence. The culture medium was removed by aspiration, the cells were washed with PBS (Invitrogen, 1.0 mL/well), and the wells were pretreated with experimental medium with or without the VMAT2 inhibitors reserpine (1 µM, Sigma-Aldrich) or dihydrotetrabenazine (DTBZ, 2 µM; Sigma-Aldrich) for approximately 60 minutes. To initiate uptake, solutions of experimental probe with or without inhibitor were added to the appropriate wells for a final concentration of 20µM probe with or without reserpine (1 µM) or DTBZ (2 µM). Cells were incubated at 37˚C for 2 h, at which point the probe solutions were removed by aspiration and wells were gently washed with PBS (2 mL). Wells were maintained in fresh experimental medium and were imaged as described above.

Quantification of VMAT2 substrate activity

The Multiple Thresholds ImageJ plug-in (created by Damon Poburko, Simon Fraser University, Burnaby, BC, Canada) was used for quantification of fluorescent puncta in images of VMAT2-HEK cells obtained from fluorescence microscopy. Puncta were identified as objects conforming to defined parameters: brightness (> 0.6 SDs above background), appropriate size (0.5 – 4 μm^2)**,** rounded shape (min circularity: 0.6), and well delimited boundaries. Data presented as mean intensity of these puncta structures per

image, normalized to uptake by tetR-HEK cells as background ± SEM from four independent experiments (six images per condition per experiment).

Determination of FFN Loading and Release in Acute Murine Brain Slices

Preparation of acute murine brain slices

All animals used for slice preparation were C57BL/6 mice obtained from the Jackson Laboratory (Bar Harbor, ME). For slices containing the locus coeruleus, animals were sacrificed at 20 days due to peak NET expression at an early age (Sanders et al. 2005). For all other experiments mice were used at 7-9 weeks. All animal protocols were approved by the IACUC of Columbia University. Mice were decapitated and acute 300 µm thick coronal slices were cut on a Leica VT1200 vibratome (Leica Microsystems) at 4^{o}C and allowed to recover for 1 h in oxygenated (95% O_2, 5% CO_2) artificial cerebrospinal fluid (ACSF) containing (in mM): 125 NaCl, 2.5 KCl, 26 $NaHCO_3$, 0.3 KH_2PO_4, 2.4 $CaCl_2$, 1.3 $MgSO_4$, 0.8 NaH_2PO_4, 10 Glucose (pH 7.2-7.4, 292-296 mOsm/l). Slices were then used at room temperature for all imaging experiments.

Application and 2-photon imaging of FFNs

Slices were incubated with the FFN (10 µM) for a 30 min bath incubation and then transferred to an imaging chamber (QE-1, Warner Instruments, Hamden, CT) and held in place by platinum wire and nylon string custom made holder and superfused (1 ml/min) with oxygenated ACSF (Wong et al. 2011). Slices were allowed to wash in the perfusion chamber for at least 10 min before imaging. For any inhibition experiments, slices were first pre-incubated with the inhibitor (1 µM nomifensine or 500 nM reboxetine) for 15 min, and then co-incubated with the FFN for the 30 min loading period. Inhibitor was also added to the perfusing ACSF solution. Fluorescent structures were visualized at depths of at least 25 µm from the slice surface using a Prairie Ultima Multiphoton Microscopy System (Prairie Technologies, Middleton, WI) with a titanium-sapphire Chameleon Ultra II laser (Coherent) equipped with a 60 X 0.9 NA water immersion objective. FFN270 was excited at 760 nm and 440-500 nm light was collected. Images were captured in 16-bit 112 x 112 µm^2 field of view at 512 x 512 pixel^2 resolution and a dwell time of 10 µs/pixel using Prairie View software. For imaging the sparse noradrenergic cortical projections 20 µm thick z-stacks (1 µm/image) were collected and then compressed using a maximum z-projection.

Colocalization of FFN270 and TH-GFP

Colocalization of FFN270 and noradrenergic structures was performed in animals that express GFP under the tyrosine hydroxylase promoter (TH-GFP) (Sawamoto et al. 2001). Acute slices from the LC or barrel cortex were incubated with FFN270 as described above and imaged using interlaced scanning with two separate lasers. FFN was imaged using 740 nm excitation and an emission range of 435-485 nm, and GFP was imaged using 920 nm excitation and an emission range of 500-550 nm. To quantify the number of GFP-positive cells in the LC that colocalize with FFN, cells were manually selected if they contained fluorescence in either channel that was greater than 2 standard deviations above background, and reported as the percentage of GFP-positive cells that also contain FFN270 signal. Quantification of the colocalization of noradrenergic projections in the barrel cortex was determined by identifying FFN270 puncta using the Multiple Thresholds plug-in for the ImageJ software. Any ROIs that corresponded to fluorescence in blood vessels were manually discarded. The identified ROIs were then considered to positively colocalize if greater than 50% of the pixels overlapped with GFP signal that was greater than 2 standard deviations above background, and reported as the number of visibly discernable GFP axons with FFN270-postive puncta.

Electrical stimulation of FFN270 loaded cortical projections

For better temporal resolution (15 s/frame), imaging during electrical stimulation experiments used a smaller 54 x 54 μm^2 area and 5 µm thick z-stack. At the start of electrical stimulation, a 10 Hz stimulation train (6 min total, each pulse 200 ms x 180-200 mA) was applied locally to the barrel cortex by a bipolar stainless steel electrode using an ISO-Flex stimulus isolator triggered by a Master-8 pulse generator (AMPI, Jerusalem, Israel). Quantification of fluorescent changes in destaining puncta was performed as described in a previous publication from our laboratory using a custom made Matlab script available from our laboratory's website at http://sulzerlab.org/.[41] The kinetics of release were then determined from the fluorescent traces using GraphPad Prism 5 by fitting with a single exponential decay function.

Channelrhodopsin-2 expression, colocalization, and release

Channelrhodopsin-2 (ChR2) was selectively expressed in noradrenergic neurons using TH-IRES-Cre (Jackson Laboratory) animals and a Cre-Lox adenoassociated virus (AAV/2/5.EF1a.DIO.hChR2(H134R)-EYFP.WPRE.hGH, obtained from Penn Vector) injected into the locus coeruleus (AP: -5.45, ML: +1.30,

DV: -3.80) unilaterally as described by our laboratories previously.[54] Animals were then allowed to recover for 4 wk prior to use in FFN experiments. To measure colocalization in the barrel cortex, FFN270 was imaged using 760 nm excitation and an emission range of 435-485 nm, and EYFP was imaged using 950 nm excitation and an emission range of 500-550 nm. Quantification of colocalization between EYFP-positive axons and FFN270 puncta was conducted as described above and reported as percentage of FFN axons that also contain EYFP signal greater than 2 standard deviations above background. Stimulation of ChR2 was achieved using a 470 nm LED source (LED4D067 and DC4100 driver, Thorlabs) to provide blue light pulses (10 Hz, 5 ms duration, 2,400 pulses total) locally to the brain slice. Due to the overlap between FFN270 emission and the ChR2 excitation source, changes in fluorescence were measured only before and after stimulation. The before and after image stacks were registered using the Correct 3D Drift plug-in (Parslow et al. 2014). For quantification, puncta from the pre-stimulation stack were selected using the Multiple Threshold plug-in. The mean fluorescence from puncta of a visually continuous axon were then compared to the mean fluorescence post-stimulation. Each FFN270-positive axon was then grouped based on whether there was colocalization with EYFP signal as determined by signal greater than 2 standard deviations above background. Slices from both the injected and non-injected brain hemispheres were used for analysis.

AMPH release in acute brain slice

To measure changes in FFN270 following AMPH treatment, acute brain slices containing the barrel cortex were prepared and loaded with FFN270 as described above. 20 µm thick z-stacks were imaged every 60 s for 15 min total. AMPH (10 µM) was added to the ACSF and then perfused over the slice starting at 5 min. These z-stacks were then registered using the Correct 3D Drift plugin and the AMPH-dependent fluorescent changes were quantified by both the number of puncta selected by the Multiple Threshold plug-in and the average fluorescent intensity of those puncta over time.

FFN270 Loading and Release *in vivo*

FFN270 loading in vivo

Mice were anesthetized with isoflurane (1-4%). The depth of anesthesia was monitored by both the animal's response to toe-pinch every 5 min and observation of respiratory rate. Once the proper depth of

anesthesia was reached, the animal was placed in a small animal stereotactic apparatus on top of a heating pad and Puralube vet ointment was applied to the eyes to prevent vision loss. All surgical procedures were performed in a sterile manner. Marcaine (0.5%) with saline 1:2 (0.25%) (2 mg/kg), was injected subcutaneously along the midline of the scalp as a local anesthetic. Before the incision, the hair over the scalp area was removed with NAIR and sterilized with a gentle scrub with Betadine on a sterile cotton swab, followed by 70% ethanol, repeated 3 times. The scalp was then removed with surgical scissors, membranes over the skull were removed by scraping, and the exposed bone was dried with compressed air. A 3 mm cranial imaging window was then made over the barrel cortex with a high speed dental drill (Midwest Stylus 360). The meninges were inspected to make sure there was no damage. Any bleeding from the bone was stopped with an application of collagen foam (Avitene Ultrafoam, Bard Davol). A glass pipette attached to a Nanoject II (Drummond Scientific) was filled with a 1 mM solution of FFN270 diluted in ACSF and attached to the stereotax. 100 nL of FFN270 was injected into the brain at coordinates AP: -0.9 mm to -1.0 mm and ML: 3.0 mm, over several depths (DV: 100 µm, 50µm, and 20 µm) with 3 minutes of delay per depth. The glass pipette was then withdrawn from the brain and a plastic ring was glued around the window with Loctite 454 to hold ACSF for imaging. A metal headmount was then glued to the nearby exposed bone with Loctite 454. The mouse was then injected with ketamine (100 mg/kg) and xylazine (10 mg/kg) i.p. and then weaned off of isoflurane while making sure to maintain depth of anesthesia. The mouse was then headfixed under the multiphoton microscope for imaging. The body temperature of the mouse was maintained for the duration of imaging with a heating pad.

Channelrhodopsin-2 stimulated release in vivo

ChR2 animal preparation, blue light stimulation parameters, and analysis were conducted as described above for acute brain slice experiments. The ChR2-positive animals that were used for ChR2 colocalization and FFN270 release in brain slice were also used for the *in vivo* experiments. Due to a larger degree of z-shift that was present *in vivo*, the imaging parameters for this experiment were modified slightly to collect from a larger z-stack (30 µm, 1 µm/image), while all other imaging parameters remained the same. The noradrenergic projections of the barrel cortex were then locally stimulated 35 min post FFN270 injection (waited 30 min after initial injection to allow NET-dependent accumulation and natural clearance of unloaded FFN270 probe from background tissue, followed by 2 pre-stimulation image

stacks). For these experiments, cranial windows were only created on the same hemisphere as the viral injection, and the data from both the ChR2-positive and -negative populations came from the same hemisphere.

AMPH induced FFN270 release in vivo

For AMPH experiments, after FFN270 was loaded, 30 µm z-stacks were collected every 5 min starting from 30 min post-FFN270 injection. After 2 image stacks, AMPH (0, 1, or 10 mg/kg) in Dulbecco's phosphate-buffered saline was injected into the intraperitoneal cavity. Images stacks were collected for 30 min post-injection. These stacks were registered using the Correct 3D Drift plug-in, and then puncta were selected using the Multiple Threshold plug-in using ImageJ. For the z-planes that remained consistent across the entire time course, the number of identified puncta were compared for each time point and normalized to the z-stack collected just before AMPH injection.

Statistics

Data is presented as mean ± SEM and standard parametric tests were used for statistical analysis. For the comparison of two different conditions a two-tailed t-test was used, while a one-way ANOVA was used for comparing conditions of three or more. A two-way ANOVA was used to compare changes between two different traces over time. The sample size was chosen based on similar studies in the field and based on our previous studies, the exact sample size for each result is incorporated in the text. To determine the normality of a particular distribution we used the D-Agostino & Pearson test. Data collection and analysis were not randomized or performed blind to the conditions of the experiments.

RESULTS

Design, lead identification, synthesis, and photophysical properties of NE-FFNs.

We approached the global design of NE-FFN probes by incorporating the key structural feature of NE, the arylethylamine fragment, into the coumarin fluorophore (Fig. 1A). We chose this design as the FFN probe must act as a substrate of both NET on the plasma membrane of NE neurons and VMAT2 on

the NE synaptic vesicles. Selective binding of these compounds to their protein targets is not sufficient; they need to be actively transported like the native neurotransmitter across the plasma and vesicular membrane via ion gradient-coupled processes. Thus, a major portion of the structural space of molecular fluorophores was not applicable owing to their large size. The relatively small coumarins, however, proved excellent fluorophores for this purpose due to their high brightness-to-size ratio, photostability, and biocompatibility. Aided by the relative substrate permissiveness of NET (Rothman 2003, Bonisch et al. 1999, Rorres et al. 2003), we pursued the discovery of coumarin-based NET substrates.

Lead identification was initiated by examining the DA-FFNs, FFN102 and FFN202, which have been successfully used to study dopaminergic projections in the striatum of acute murine brain slices (Rodriguez et al. 2013). To test the applicability of FFNs *in vivo*, the compounds were applied (50 µM, 30 min) to the frontal cortex of mice through exposed cranial windows. Whereas FFN102 showed no appreciable uptake above background, we observed numerous punctate axonal strands with FFN202 (Supplementary Fig. S2). Since FFN102 did not label these same axons, we hypothesized that they did not express DAT, but instead the closely related NET, and thus represented NE axons. Indeed, NET activity of FFN202 was confirmed using human embryonic kidney cells stably transfected with human NET (hNET-HEK). Further, the simpler analog **201**, sharing the 3-aminoethyl core of FFN202, was identified as an excellent substrate for NET (Fig. 6E). Despite its favorable transporter properties at NET, **201** is not a well-suited fluorescent probe for brain tissue, due to its insufficient brightness and due to the pK_a of the phenolic group (pK_a = 8.0) being outside of the desired physiological pH range to allow distinction between localization in the vesicles (pH 5.5) and the extracellular space (pH 7.4). Both limitations can be addressed by introducing an electron-withdrawing group in the adjacent position to the coumarin phenol, thus providing the rationale for the development of a series of related, halogen-substituted coumarins.

Synthesis of this library of fluorophores with desirable photophysical properties and phenol pK_a values was accomplished with a 5-step synthetic sequence using 2- and 4-haloresorcinols as commercially available starting materials (Fig. 6D). The presence of an electron-withdrawing chlorine or fluorine atom in the 6- and 8- position (Fig. 6E) increased acidity of the phenolic group (pK_a = 5.9 – 6.3)

and shifted the pK_a to the desired physiologically relevant pH range (5.5-7.4, Supplementary Table S1). At the cytosolic pH of ~ 7.4, the haloanalogs are mostly in a phenolate form, which is considerably brighter than the protonated phenol form. As a result of this acidification, all newly prepared FFN candidates bearing a halogen atom displayed greater brightness than FFN201 (pK_a = 8.0). These compounds, including FFN270, exhibit two resolved absorption/excitation maxima depending on solvent pH (FFN270 ex: 320 nm or 365 nm, em: 475 nm, Supplementary Fig. S1) and thus can function as ratiometric fluorescent pH-sensors.

Development of fluorescent coumarin substrates of NE transporter

The collection of 7-hydroxycoumarin compounds (Fig. 6E) was examined for possible NET substrates using a multi-well fluorometric assay to measure NET-dependent uptake in hNET-HEK cells. The cells were grown in 96-well plates and incubated with the experimental compounds (5 µM, 30 min) in the absence and presence of the NET inhibitor, nomifensine (2 µM). The activity of the compounds at NET was determined by comparing the fluorescence intensity between the uninhibited wells (signal S; NET-dependent and independent/nonspecific uptake) and the inhibited wells (basal signal B; only NET-independent/non-specific uptake) and expressed as a signal-to-basal ratio (S/B) (Fig. 6F).

The 4-series hydroxycoumarin fluorophores (bearing the aminoethyl group in the 4-position of coumarin), including the dopaminergic tracer FFN102 (Rodriguez et al. 2013, Pereira et al. 2016, Lee et al. 2010), showed insignificant activity at NET; whereas **201**, the parent compound of 3-series regioisomers, showed robust transporter-dependent fluorescence accumulation (~ 10-fold S/B, Fig. 6). Introducing the fluorine atom in position 6 of the 3-series coumarin ring, affording compound **093**, improved the photophysical properties, but negatively affected the ability of the fluorophore to act as a substrate for NET. Increasing size of the halogen atom in this position caused a further decrease in NET activity (H (**201**) > F (**093**) > Cl (FFN202)), with FFN202 showing only weak NET uptake (< 2-fold S/B). In contrast, placing the fluorine atom in position 8, generating FFN270, led to a small reduction in specific uptake (8.5 ± 0.4) compared with the lead compound **201** (9.9 ± 0.4, n = 3, p = 0.04, Fig. 6F), while still improving photophysical properties (pK_a = 6.25). However, additional increase in size of the halogen atom at position 8 eliminated NET activity (**269**, < 2-fold S/B).

To confirm the hNET substrate activity of FFN270 demonstrated in the fluorometric study, we used epifluorescence microscopy to visually compare cellular uptake and labeling morphology of uninhibited and inhibited hNET-HEK cells using nomifensine (2 μM) or cocaine (1 μM), as well as control HEK293 cells. In hNET-transfected cells, FFN270 exhibited a homogeneous staining pattern indicative of cytosolic distribution (Fig. 6G), while only negligible uptake was found in nomifensine treated (Fig. 6H), cocaine treated (Supplementary Fig. S3), and null-transfected cells (Supplementary Fig. S3), confirming the NET-dependent uptake identified from the initial screen. We also examined hDAT and hSERT-transfected HEK cells, and found that FFN270 is selective for hNET (Supplementary Fig. S4)

.**FFN270 is also a substrate of the Vesicular Monoamine Transporter-2**

To determine the potential of FFN270 to load NE synaptic vesicles and therefore trace NE neurotransmission, we examined VMAT2-dependent transport using a protocol employing HEK cells stably transfected with rat VMAT2 (VMAT2-HEK). This system, where VMAT2 is expressed and active on acidic intracellular organelles of HEK cells, has been employed extensively by our laboratories. (Adam, Edwards, & Schuldiner, 2008; Hu et al., 2013; Lee, Gubernator, Sulzer, & Sames, 2010) VMAT2 activity was evaluated using wide-field epifluorescence microscopy, which enables visualization of individual cells and the intracellular distribution of the fluorescent compounds (Fig. 7C-F). In comparison to NET-HEK cells, these cells do not over-express NET on the plasma membrane, and as a result, higher concentrations of the probe (20 μM) and longer incubation times (2 h) are used in this experiment to facilitate passive diffusion.

VMAT2-HEK cells that were treated with FFN270 displayed a bright punctate fluorescent pattern consistent with accumulation of the compound in acidic organelles expressing VMAT2 (Fig. 7C). This VMAT2-dependent accumulation was expressed as normalized total puncta fluorescence (number of puncta multiplied by average puncta fluorescence intensity, Fig. 7A). In contrast, only general cytosolic fluorescence was observed in the null-transfected HEK cell line (not expressing VMAT2, Fig. 7F) or in VMAT2-HEK cells pretreated with a VMAT inhibitor, either dTBZ (2 μM, Fig. 2D) or reserpine (2 μM, Fig. 7E). Comparing the VMAT2-uptake of FFN270 with FFN102, a previously confirmed VMAT2 substrate

used to measure DA vesicular exocytosis *ex vivo* (Lee et al. 2010), confirmed that FFN270 accumulated in acidic organelles in a VMAT2-dependent manner with similarly normalized intensity ($n = 4$, $p = 0.26$, Fig. 7A), indicating that this probe is a dual NET-VMAT2 substrate.

FFN270 labels NE neuronal soma and axons in murine brain tissue ex vivo

After reaching the *in vitro* criteria of an NE-FFN – including dual transporter substrate activity (NET and VMAT2), favorable photophysical properties (sufficient brightness and phenol pK_a within vesicle physiological pH range), and low basal cellular labeling – we examined whether FFN270 is suitable for labeling neurons by applying the probe to the LC region of acute mouse brain slices (Fig. 8), the primary region for noradrenergic cell bodies in the brain. Using a mouse line expressing green fluorescent protein (GFP) under the tyrosine hydroxylase promoter (TH-GFP) (Matsushita et al. 2002), GFP is expressed in catecholamine neurons, and can be used as a reference marker for noradrenergic neurons in the LC, since this region does not contain dopaminergic cell bodies (Ungerstedt 1971). We observed that 72% of noradrenergic cells expressing GFP were also labeled with FFN270 (greater than 2x SD of the background, 62/86 cells, 6 animals, Fig. 8B-D), while previous generation DA-FFN probes, such as FFN102, showed no measurable uptake by any GFP-labeled cells in this region (Fig. 8E-G).

We next determined the degree to which FFN270 labels the projections of these noradrenergic cell bodies by measuring uptake in the outer layers (Layer 1-3) of the barrel cortex (Fig. 9A). This brain region receives extensive noradrenergic innervation (Robertson et al. 2013), and NE-dependent neuromodulation has been shown to affect the strength and temporal patterns of sensory input-activated barrel cortical networks (Devilbiss and Waterhouse 2004, Constantinople and Bruno 2011, Motaghi et al. 2006). After FFN270 incubation in acute brain slice, we observed significant staining of noradrenergic axons, as well as some blood vessels (Fig. 9B). Due to the relatively sparse density of labeled projections, the representative 2D images shown are maximum Z-projections of 20 µm thick volumes. Consistent with observations in the LC, FFN102 did not label these cortical noradrenergic projections (Fig. 9C), and as predicted by preliminary *in vivo* results, FFN202 showed minor uptake (Supplementary Fig. S5). FFN270 loading of these structures was inhibited with nomifensine (2 µM), or the selective NET

inhibitor reboxetine (500 nM, Fig. 4D and E), indicating that NET-dependent transport was required for FFN270 uptake into these projections. This inhibition of uptake was quantified by comparing the number of puncta in the presence of nomifensine (11%, n = 3, p = 0.004) or reboxetine (24%, n = 3, p = 0.007, Fig. 9F) to untreated slices.

We further confirmed that the FFN270-labeled projections in the barrel cortex were noradrenergic using TH-GFP animals as a fluorescent marker. We observed significant axonal colocalization between GFP and FFN270 (88.9%, 154/176 axons, 4 animals, Fig. 9G-I). We quantified colocalization by measuring the fraction of GFP-labeled axons that also contained significant FFN labeling (> 2x SD of background). Unlike the LC, however, there is potentially some dopaminergic innervation in this area (Gurevich and Joyce 2000), and GFP in this transgenic mouse line does not distinguish between dopaminergic and noradrenergic projections. Consequently, we examined colocalization in TH-Cre animals that were injected only in the LC with a virus that expresses the fluorescent marker, enhanced yellow fluorescent protein (EYFP) in the presence of Cre recombinase (AAV/2/5.EF1a.DIO.hChR2(H134R)-EYFP.WPRE.hGH, Supplementary Fig. S6) (Kempadoo et al. 2016). In these animals, we observed substantial EYFP expression in cortical noradrenergic projections of the barrel cortex, and a high degree of colocalization between the fluorescent marker and FFN270 (72.4%, 92/127, 6 animals, Fig. 10C-E). The fraction of FFN projections that do not contain EYFP is consistent with our TH-GFP colocalization when accounting for our measured viral transduction efficiency (90-96%),[54] indicating less than 10% of FFN270-labeled axons could be dopaminergic.

FFN270 reveals NE axonal release sites and their functional heterogeneity

We next examined whether the punctate fluorescence in the noradrenergic axons represented the uptake and storage of FFN270 in synaptic vesicles, and whether FFN270 could be released using electrical and channelrhodopsin-mediated stimulation techniques. Using electrical stimulation (10 Hz, 3,000 pulses), we observed a single exponential decay in background-subtracted puncta fluorescence over time with a half-life of 34.6 s, a significant increase in FFN release when compared to the non-stimulated control slices (Fig. 10A, 2-3 slices per animal, 3 animals). The rate of FFN270 release from puncta was comparable to the release rate observed with other FFNs in dopaminergic synapses.[41]

Repeating the electrical stimulation while inhibiting calcium channels using Cd^{2+} (200 μM) led to a 92% reduction in the number of identified destaining puncta, confirming that FFN270 release was due to calcium-dependent stimulated vesicle exocytosis (2-3 slices per animal, 3 animals).

Using a complementary optogenetic system in which mice unilaterally express channelrhodopsin-2 (ChR2) and EYFP in noradrenergic neurons (viral delivery as described above), we also measured activity-dependent FFN270 vesicular release triggered by 470 nm light stimulation (10 Hz, 2,400 pulses). As local ChR2 activation selectively excites noradrenergic axons, these results exclude potential local circuit effects that may result from electrical stimulation of the acute brain slice. Since the FFN emission wavelength overlaps with the stimulation light, we could not monitor FFN fluorescence during the stimuli, and therefore measured fluorescence before and after. We compared the change in fluorescence of individual FFN-labeled axons that colocalized with the ChR2-EYFP signal (ChR+) to axons that did not express ChR2-EYFP (ChR–). In the absence of ChR, there was a baseline 27.6 ± 3.3% loss in fluorescence after 4 min of stimulation. In puncta with ChR, the loss in fluorescence was 57.4 ± 5.9%, a 2.1-fold increase (2-3 slices per animal, 5 animals, $p < 0.0001$, Fig. 5C-F).

We also compared the FFN release between individual NE axons within the ChR+ and ChR– populations. FFN destaining from the noradrenergic axon population of the ChR– group fit a normal distribution (D-Agostino & Pearson test, $p = 0.3$), but the ChR+ group did not ($p = 0.003$, Fig. 5G). As reported with dopaminergic FFNs,[41] by tracing neurotransmitter release with single synapse resolution, a trend of low releasing or “silent” presynaptic sites and a separate high releasing population was apparent. The fluorescent changes of the ChR+ group were well fit by the sum of two normal distributions with distinct peaks ($R^2 = 0.91$). While some of the ChR2+ axons (34%) only released 15.1 ± 2.2% of their fluorescent content, the majority of axons (66%) almost fully destained, releasing 75.4 ± 10.9% (Fig. 5G). We confirmed this is not an artifact of particular acute brain slices by repeating the normality test on the same ChR+ axons grouped by slice and observed a normal distribution between slices ($p = 0.2$).

To examine the axons with remaining FFN signal post-electrical or optogenetic stimulation, we then exposed slices to AMPH (10 μM), which produced a nearly complete loss of puncta after 5 min (90.8 ± 3.2%, 2-3 slices per animal, 3 animals, Supplementary Fig. S7), suggesting that the remaining

fluorescence in these “silent” boutons was located in healthy noradrenergic axons that express functional NET and/or VMAT2 and can undergo AMPH-induced reverse transport. The remaining 9.2% of puncta that did not destain after the entire time course likely represented the nonspecific signal of FFN270 in acute brain slices, and were comparable to the number of puncta that remained in slice after inhibition with nomifensine (7.2 ± 0.7%).

Together, the results in acute mouse brain slices confirm that FFN270 is actively accumulated into noradrenergic synaptic vesicles and provides the first probe capable of quantifying noradrenergic synaptic release with single synapse resolution in brain tissue, and the first insight into functional properties of NE synapses in CNS.

FFN270 is an optical tracer of NE *in vivo*

We next used two-photon imaging of the superficial cortical layers through a cranial window to characterize the potential of FFN270 to study noradrenergic axons in the brain of living animals. For *in vivo* experiments, an imaging window in the skull over the barrel cortex was created, and FFN270 (100 pmol) was injected through the window into the anesthetized animal at depths from 100 to 20 µm from the surface of the brain. In contrast to our original *in vivo* FFN lead, FFN202, we observed a dramatically increased number of FFN-labeled axons using FFN270, with a better signal to background fluorescence ratio that persisted over 2 hours (Fig. 11).

We found that FFN270 could be used to study evoked NE release *in vivo* using the virally expressed ChR2 system described above (Fig. 11D-F). We measured the change in FFN fluorescence of loaded axons before and after 470 nm light stimulation (10 Hz, 2,400 pulses), and compared the changes observed in axons that did (ChR+) and did not (ChR–) colocalize with the ChR2-EYFP signal. We observed a 2.5-fold increase in the amount of released FFN from ChR+ axons (46.2 ± 8.3%) compared to ChR– axons (18.13 ± 4.8%, n = 6 different animals, p = 0.006, Fig. 11C). With FFN270 we could clearly distinguish the differences in firing rates between noradrenergic axons undergoing the slow tonic firing observed in anesthetized animals (Aston-Jones and Bloom 1981), and those that were optogenetically stimulated. In the living animal we also observed differences in the distribution of FFN release from individual axons with and without ChR2. The ChR– population was well fit by a normal distribution (D-

Agostino & Pearson, p = 0.38) while the ChR+ population did not (p = 0.002), suggesting that axons with ChR2 can possess different release properties *in vivo*. In contrast to results in the brain slice, however, we were unable to fit the *in vivo* ChR+ axons to a double Gaussian with well-defined low and high releasing populations. This may be due to differences and added difficulties of imaging discrete structures *in vivo*, combine with the limitations of only collecting before and after images when using a blue light activated ChR. Alternative stimulation techniques or red-shifted ChRs provide potentially improved approaches for measuring FFN release concurrently with noradrenergic excitation.

We then used FFN270 to examine the effect of acute AMPH treatment on the noradrenergic system of a living mammal. While AMPH is currently used to treat ADHD in hundreds of thousands of patients (and abused by millions of people), there is a debate on how AMPH treatment affects individual noradrenergic projections in the cortex (Berridge and Stalnaker 2002, Blanc et al. 1994). Using the same *in vivo* FFN270 loading and imaging technique, we measured changes in FFN content during two AMPH treatments (1 and 10 mg/kg) administered through intraperitoneal injection (i.p.) (Salahpour et al. 2008). Over 25 min, we observed significantly more FFN released in each AMPH condition compared to saline-injected controls (Fig. 12). After 5 min, we observed decreases of 63.2 ± 9.9% (1 mg/kg, n = 6 different animals) and 81.4 ± 5.2% (10 mg/kg, n = 5 different animals) in the number of FFN-positive structures after AMPH treatment, compared to 12.2 ± 7.3% for saline injected controls (n = 7 different animals, $p < 0.001$ for both AMPH treatments, Fig. 12D). After 15 min, AMPH-induced FFN270 destaining was largely complete, with almost total release from all FFN270 loaded noradrenergic projections (> 95% reduction in puncta).

FIGURES

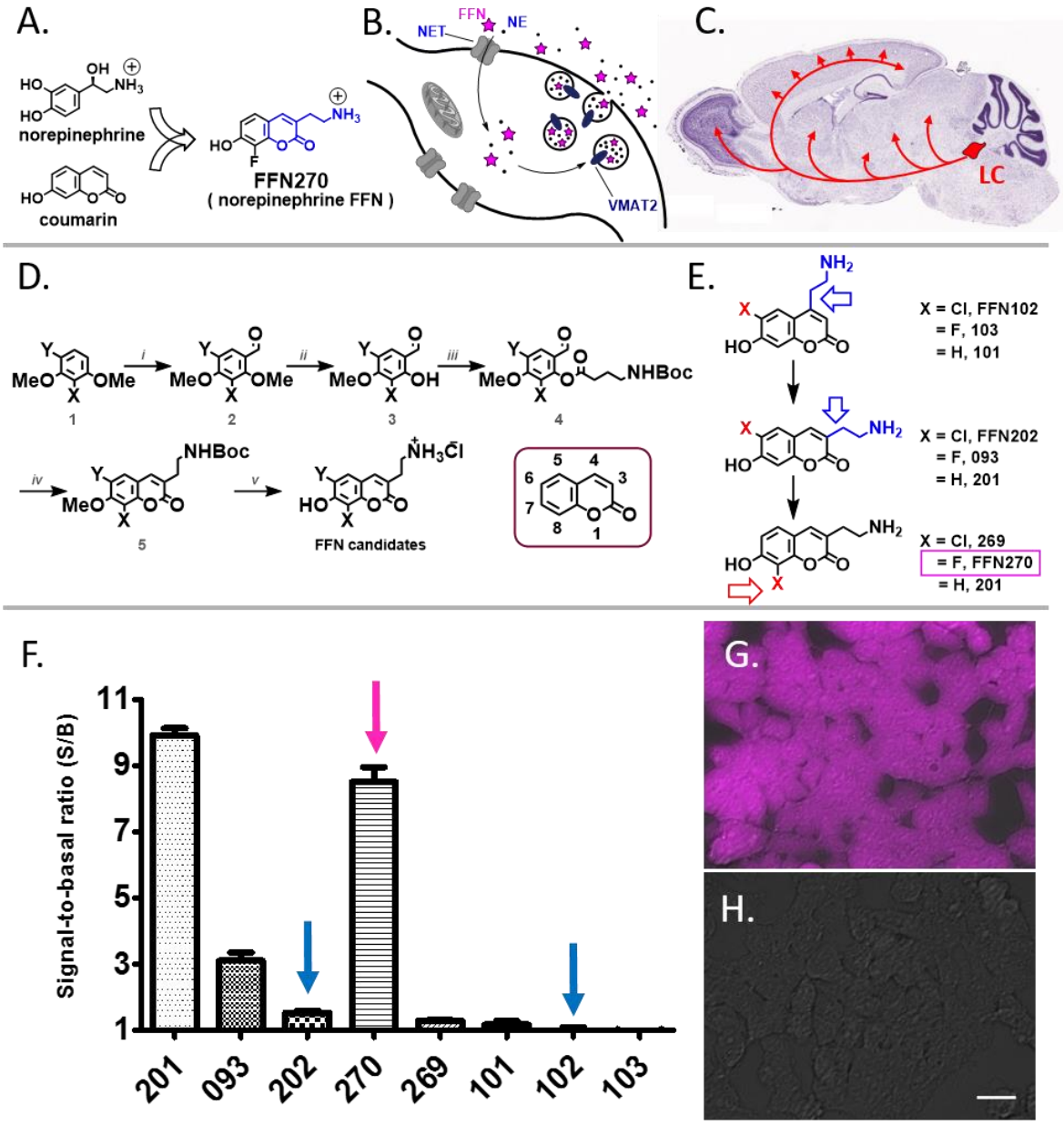

Figure 6. Design of NE-FFNs. A) Design of NE-FFNs combines structural features of NE with the coumarin fluorescent core. B) NE-FFNs trace NE uptake from the extracellular space, packaging into vesicles, and exocytosis as they are designed to be substrates of NET and VMAT2. C) Representative illustration of NE neuron distribution in the brain (Allen Brain Atlas). Neurons originate from the locus coeruleus (LC) and project to the majority of brain regions. D) General synthetic scheme for preparation of 3- and 4-series aminoethyl-7-hydroxycoumarins as potential NE-FFN candidates. See Methods for experimental conditions. E) Library of candidate NE-FFNs. F) Total cellular fluorescence after loading of candidates (5 µM) in hNET-HEK cells. Signal to Basal ratio (S/B) was determined by comparing FFN fluorescence in the presence and absence of 2 µM nomifensine after a 30 min incubation period. Highlighted in blue are the previously described DA-FFNs, and in magenta is FFN270, the leading pH-sensitive NE-FFN candidate (S/B: 8.5 ± 0.4, n = 3). Representative images of FFN270 without inhibitor (G) and with inhibitor (H). Scale bar: 20 µm. (work by Adam Henke and Richard Karpowicz)

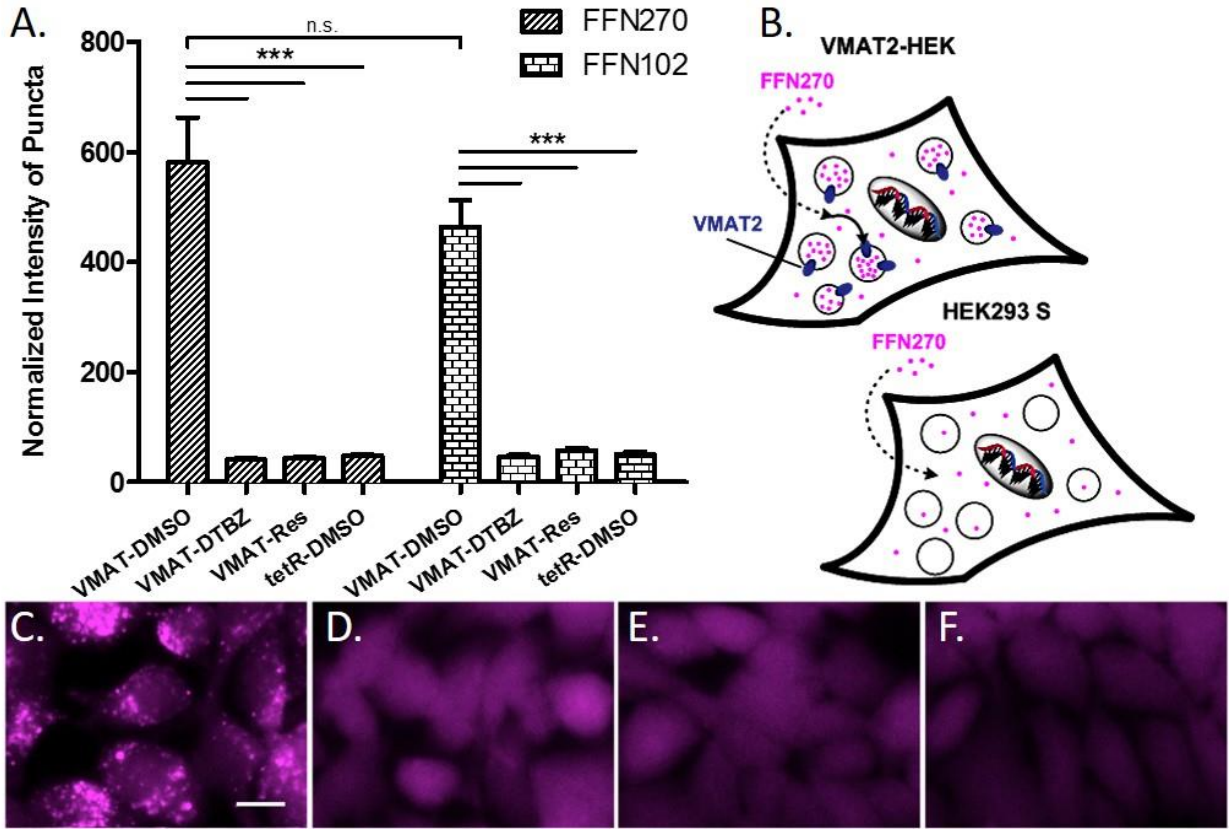

Figure 7. FFN270 is a VMAT2 substrate. A) VMAT2-dependent loading of FFN102 and FFN270 were compared using the normalized intensity of puncta (number of puncta multiplied by average fluorescence intensity) in VMAT2-HEK cells after a 2h incubation (20µM) under different conditions. B) Representative schematic depicting the rationale for intracellular punctate fluorescence with active VMAT2, and general cytosolic labeling in null-transfected or inhibited conditions. The probes passively diffuse through the plasma membrane were they are then actively concentrated in acidic compartments only when there is active VMAT2. Without active VMAT2 (inhibition or null-transfected) intracellular fluorescence is only resultant from equilibrative passive diffusion. Representative images of FFN270 in (C) VMAT2-HEK cells, (D) dTBZ (2 µM) inhibited or (E) reserpine (2 µM) inhibited VMAT2-HEK cells, and (F) null-transfected HEK293 cells. Scale bar: 10 µm (work by Yekaterina Kovalyova).

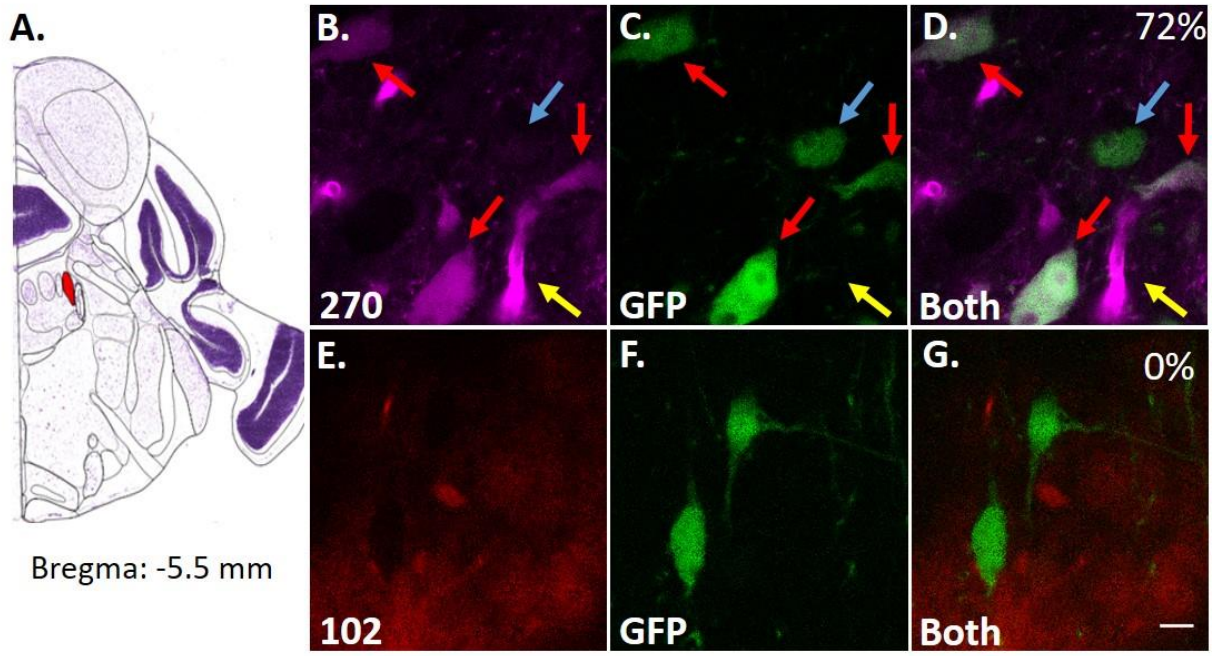

Figure 8. FFN270, but not FFN102, labels noradrenergic neurons in the locus coeruleus (LC). A) Atlas image highlighting in red the location of the LC in the mouse brain (Bregma: -5.5mm, Allen Brain Atlas). B-D) FFN270 (B) strongly colocalized with the noradrenergic label TH-GFP (C), resulting in a 72% colocalization of noradrenergic cell bodies (labeled by red arrows, 62/86 cells, 6 animals). Cells that did not colocalize are highlighted with a blue arrow, and blood vessels are highlighted with a yellow arrow. E-G) When repeated with FFN102 (E), no colocalization was observed with TH-GFP (F). Images obtained by 2-photon microscopy in acute mouse brain slice (for imaging parameters, see Methods). Scale Bar: 10 µm. (Work by Matt Dunn)

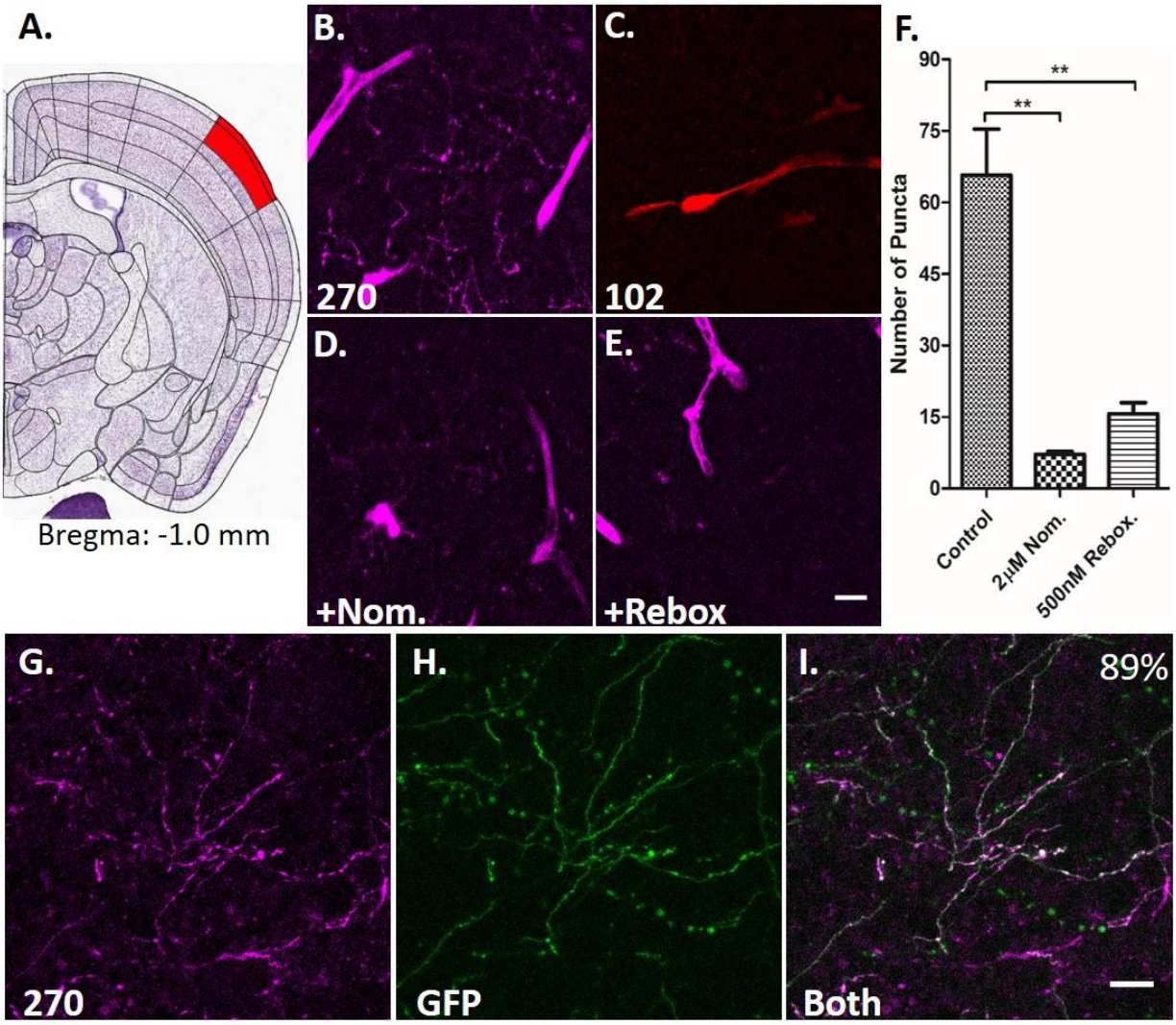

Figure 9. FFN270 is located in NE axons of the barrel cortex. Representative images FFN270 (B) and FFN102 (C) loaded into layer 1 of the barrel cortex (A, Bregma: -1.0 mm, Allen Brain Atlas) of acute murine brain slices (10 µM, 30 min, 20 µm Z-projections, 2-photon microscopy images). Expected noradrenergic axons appeared as long strings with punctated release sites, while blood vessels appeared as wider tube structures. FFN270 axonal labeling in Layer 1 of the barrel cortex could be inhibited with nomifensine (D, 2 µM, Nom.) or reboxetine (E, 500 nM, Rebox.). F) The average number of puncta was significantly higher in control conditions (68.5 ± 22) compared to Nom. (7.7 ± 0.7) and Rebox. (17.5 ± 3.5) conditions (one-way ANOVA Bonferroni test, n = 3, average of 2 slices per condition from 3 different animals). Blood vessel labeling was not inhibited. G-I) FFN270 (G) labeling also highly colocalizes (88.9%, 154/176 axons, 4 animals) with TH-GFP signal (H). Scale Bar: 10 µm (work by Matt Dunn).

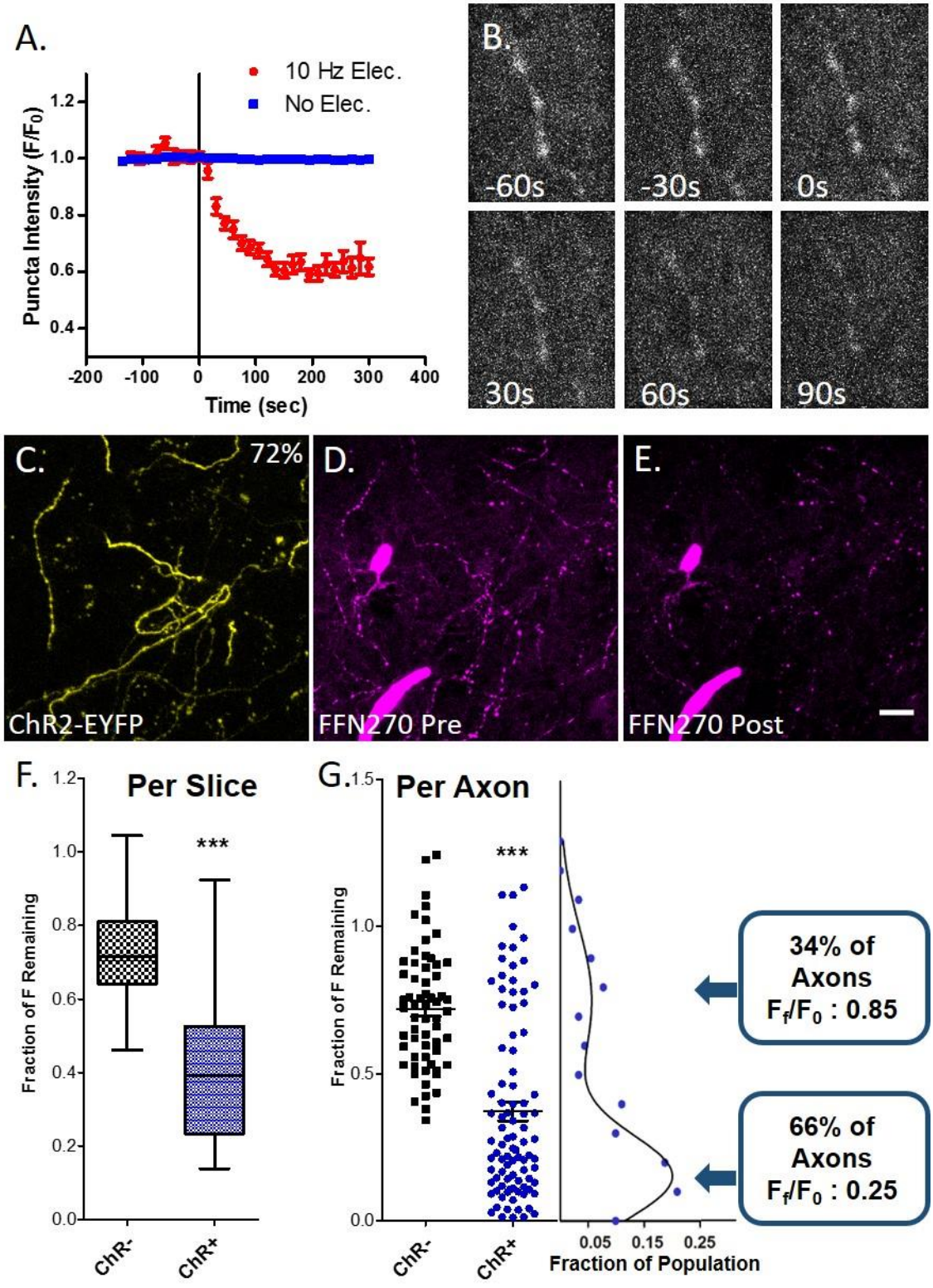
A.
10 Hz Elec.
No Elec.
Puncta Intensity (F/F0)
Time (sec)
B.
-60s
-30s
0s
30s
60s
90s
C.
72%
ChR2-EYFP
D.
FFN270 Pre
E.
FFN270 Post
F.
Per Slice
Fraction of F Remaining
***
ChR-
ChR+
G.
Per Axon
Fraction of F Remaining
***
ChR-
ChR+
Fraction of Population
34% of Axons Ff/F0 : 0.85
66% of Axons Ff/F0 : 0.25

Figure 10. Axonal FFN270 release under electrical and optogenetic stimulation reveals two populations of NE release sites in the cortex. A) Change in FFN270 puncta fluorescence in the barrel cortex of acute slice during the course of a locally applied electrical stimulation (10 Hz, 3000 pulses, starts at t: 0 min). In red are destaining puncta identified during electrical stimulation ($t_{1/2}$: 34.6 s), and in blue are puncta during no stimulation (n = 2-3 slices per animal, 3 animals for each condition). B) A representative noradrenergic axon labeled with FFN270 during electrical stimulation. FFN270 (D) also strongly colocalized with the ChR2-EYFP signal (C, 72.4%, 92/127, 6 animals) in TH-Cre animals injected with floxed-ChR2-EYFP in the LC. The ChR2 was then locally stimulated with 470 nm light (10 Hz, 2400 pulses), and the change in FFN270 signal was measured. F) There was a significant decrease in remaining FFN270 signal in axons that colocalized with ChR2-EYFP (ChR+, 42.6 ± 5.9%) compared with axons that did not (ChR–, 72.4 ± 3.3%, 2-3 slices per animal, 5 animals, $p < 0.0001$). G) The individual axons that comprise the ChR– population follow a normal distribution (D-Agostino & Pearson test, $p = 0.3$), while the ChR+ population does not ($p = 0.003$). The ChR+ population closely follows a double Gaussian distribution (Right panel histogram, $R^2 = 0.91$) with high (66%, 0.25% F remaining) and low releasing (34%, 0.85% F remaining) populations. Scale Bar: 10 µm. (Work by Matt Dunn and Kimberly Kempadoo)

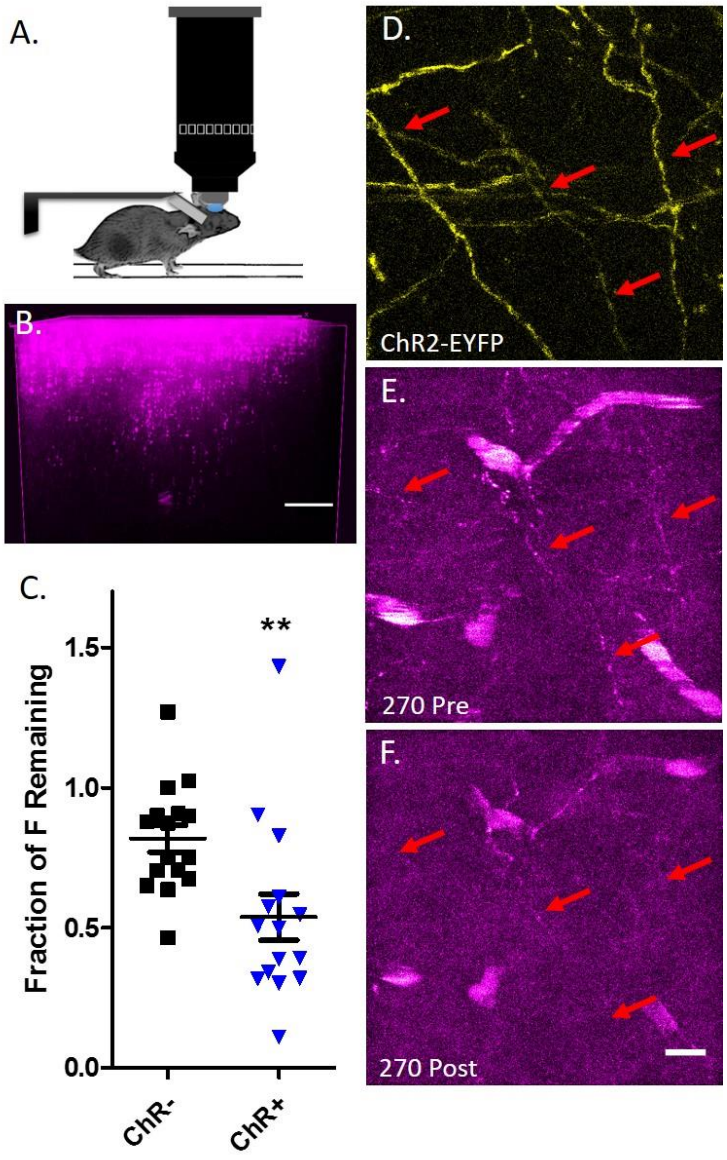

Figure 11. Examining NE axons and release sites in living animals. A) Representative *in vivo* setup using an anesthetized head-fixed animal to image Layer 1 of the barrel cortex with 2-photon microscopy. B) A representative 3-D reconstruction of FFN270 labeling (50 µM locally applied) in Layer 1 of the barrel cortex *in vivo*. Scale Bar: 20 µm. C). FFN270 loaded into NE axons with ChR2 can be released with local 470 nm light stimulation (10 Hz, 2,400 pulses). There is a significant increase in FFN270 released from axons that colocalize with ChR2 (ChR+, 46.2 ± 8.3%) compared to axons that do not (ChR–, 18.13 ± 4.8%, n = 6 different animals, p = 0.006). Representative images of the ChR2-EYFP signal (D), and the FFN270 signal before (E) and after (F) optogenetic stimulation. Axons that colocalize and destain and highlighted with red arrows. Scale Bar: 10 µm. (Work by Sam Clark and Matt Dunn)

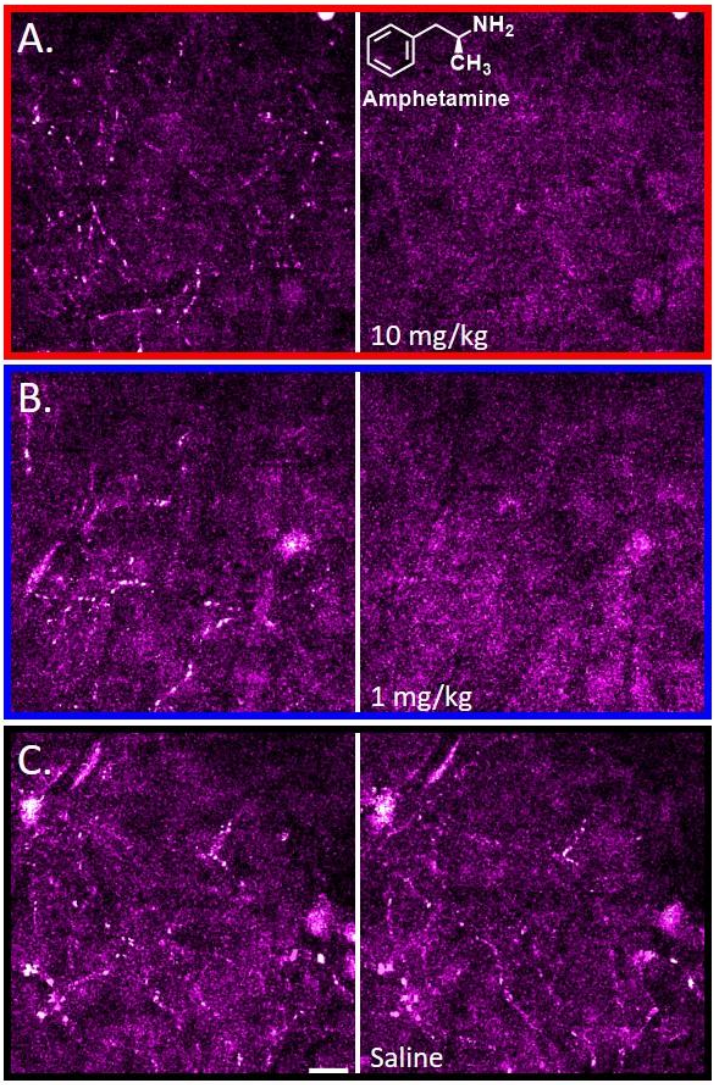
A.
NH2
CH3
Amphetamine
10 mg/kg
B.
1 mg/kg
C.
Saline

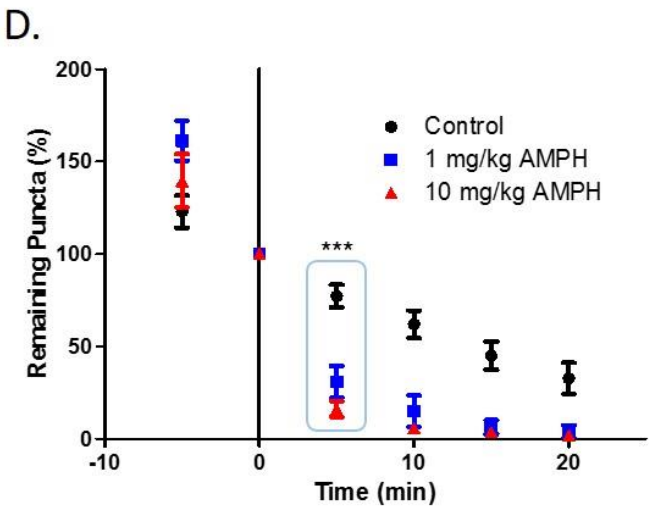
D.
Remaining Puncta (%)
200
150
100
50
0
-10
0
10
20
Time (min)
Control
1 mg/kg AMPH
10 mg/kg AMPH
***

Figure 12. Amphetamine releases FFN270 from cortical NE projections *in vivo*. Representative images of FFN270 in Layer 1 of the barrel cortex in living mice taken before and 5 min after injection of amphetamine (AMPH). The left column includes images acquired before i.p. administration of a high dose (10 mg/kg, A), low dose (1 mg/kg, B) and a vehicle (saline only, C), while the right column is post injection. D) Quantification of the number of puncta before and after each AMPH condition over a 25 min time course. After 5 min there was already a significant decrease in remaining FFN270 puncta in the high (81.4 ± 5.2%) and low (63.2 ± 9.9%) AMPH condition when compared to the control (12.2 ± 7.3%, n = 6-7 different animals per condition, $p < 0.001$ for both AMPH conditions). Scale Bar: 10 µm. (Work by Sam Clark and Matt Dunn).

DISCUSSION

The introduction of FFN270, the first FFN developed to label noradrenergic synapses, has to our knowledge, provided the first tool to image the primary function of synaptic transmission – synaptic vesicle exocytosis – in the CNS *in vivo*. Coupled with electrical and optogenetic stimulation, we were able to examine exocytosis-dependent release from NE axonal branches and individual NE release sites in murine brain tissue and within the intact cortical circuitry of the living brain. The results revealed heterogeneity of neurotransmitter release and identified a population of sites that release only a small portion of vesicular content, even after long trains of photonic pulses delivered locally to the cortical NE axons. This finding is in accordance with our recent study using FFN200, which demonstrated that a portion of dopaminergic puncta in the striatum do not release significant amounts of FFN200 (and thus DA) and are therefore functionally "silent." The present study differs in three major points: 1) we examined ensembles of single NE release sites, which originate from a distinct neurochemical cell type (LC-NE versus DA neurons); 2) the examined NE release sites are in the barrel cortex (versus DA sites in the dorsal striatum); and 3) the NE axon stimulation was achieved by selective targeting of ChR2 and local photostimulation (versus local current injection). The presence of synaptic heterogeneity in two distinct neuronal populations, in two separate brain regions, and under various stimulation methods, suggests that this may be a general phenomenon and raises multiple questions: what mechanism underlies differences in presynaptic activity? can the silent sites be activated in behavior? do the silent sites serve as reserve pools of synaptic vesicles? These and other fundamental questions can now be addressed in specific circuits using the FFN probes and associated imaging methods.

We also used FFN270 *in vivo* to address whether systemic AMPH treatment affects release from individual cortical noradrenergic projections, previously not possible with standard microdialysis or electrochemical techniques. These experiments show that pharmacologically-relevant levels of AMPH (e.g., 1 mg/kg, i.p.), that produce behavioral effects (Daberkow et al. 2013), can drive release from locus coeruleus axons in the cortex *in vivo*. While we are examining a NE-like compound rather than NE itself, this approach indicates that AMPH acts as an NE releaser and not simply as a NET blocker, a question that has been controversial in understanding the therapeutic effects of this drug in ADHD (Heal et al.

2013). As AMPH-induced neurotransmitter redistribution is mostly thought to act via reverse transport across uptake transporters rather than synaptic vesicle exocytosis (Sulzer et al. 2005, Sulzer 2011), and all FFN270 labeled axonal varicosities were uniformly destained in the cortex both *in vivo* and *ex vivo*, our findings indicate that even the low releasing sites contain neurotransmitter accumulation transporters and competent storage vesicles.

FFN270 addresses the shortcomings of, and complements the existing methods used for NE detection in the brain (Nguyen et al. 2010, Muller et al. 2014, Carlsson et al. 1962, Lindvall and Bjorklund 1974, Secor and Glass 2004, Hettie et al. 2013). Further, as a chemically targeted molecular agent, FFN270 should be applicable in primates and other species not amenable to genetic manipulation (Wakayama et al. 2017, Er et al. 2015). However, the probe does not detect the neurotransmitter itself and cannot measure the vesicle content of NE versus DA (NE is synthesized from DA in NE neurons) (Kempadoo et al. 2016) or the changes of NE concentrations at or near the release sites. We envision that the combination of FFNs and cell-based fluorogenic NE sensors (Nguyen et al. 2010, Muller et al. 2014) or protein-based sensors will provide powerful experimental tools for detailed synaptic-level examination of NE release and neurotransmission. In broad terms, multiplexing FFNs with optical techniques that measure receptor activation by neurotransmitters promises means that distinguish modulation of neurotransmission at discrete synapses, a process fundamental to learning and behavior.

Acknowledgments

This paper is dedicated to the memory of James H. Handelman, a visionary and supporter of fundamental science. This work was funded by the G. Harold & Leila Y. Mathers Charitable Foundation (to D. Sames), the National Institute of Mental Health, NIMH (R01MH108186, to D. Sames and D. Sulzer and 1F31MH109293-01A1, to S Clark), the Burroughs Wellcome Fund Postdoctoral Enrichment Program (to K. Kempadoo), and the Howard Hughes Medical Institute (to E. Kandel). We also thank Dr. Wenbiao Gan (NYU) for assistance with exploratory in vivo imaging experiments.

Author Contributions

M.D. and D. Sames initiated the project. D. Sames and D. Sulzer directed the project. D. Sames and A.H. designed the compounds. A.H. synthesized the library of derivative candidates, examined candidates in transfected-cell cultures, and characterized their photophysical properties with assistance from Y.K. and R.J.K. M.D. characterized uptake and release parameters of lead candidates in acute murine brain slice. S.C. performed surgery and FFN loading for *in vivo* experiments. M.D. and S.C. characterized *in vivo* release. Viral delivery and preparation of ChR2-expressing animals was performed by K.A.K in E.R.K's laboratory. Manuscript was prepared by M.D. with contributions from all authors. All authors contributed to the design of the study and discussion of results.

Competing Interests. The authors declare no competing financial interests.

CHAPTER 4: Piezo High Accuracy Surgical Osteal Removal (PHASOR): a technique for improved cranial window surgery in mice

AUTHORS & AFFILIATIONS: Clark SD[1], Mikofsky RM[1]*, Lawson JM[1]*, Sulzer D[1]

[1]Departments of Psychiatry, Neurology, & Pharmacology, Columbia University Medical Campus, and New York State Psychiatric Institute, NY NY 10032

*** These authors contributed equally to this paper**

KEYWORDS: Cranial window, Piezoelectric surgery, multiphoton imaging, in vivo, calcium imaging, dental drill

SHORT ABSTRACT:

Piezoelectric surgery has led to improvements in human maxillofacial and dental surgery. We have developed a protocol to optimize piezoelectric surgery for cranial window surgery in mice.

LONG ABSTRACT:

Multiphoton microscopy has been widely adapted for imaging neurons *in vivo*. Repeated imaging requires implantation of a cranial window or repeated thinning of the skull. Cranial window surgery is typically performed with a high speed rotary drill, and many investigators find it challenging to prevent the drill from damaging the delicate dura and blood vessels. Extensive training and practice is required to remove the bone without damage to underlying tissue and thus cranial window surgery can be difficult, time

consuming, and produce tissue damage. Piezoelectric surgery, which is extensively used for maxillofacial and dental surgery, utilizes ultrasonic vibrations to remove bone without damaging soft tissues. We have developed a method applying piezoelectric surgery to improve cranial window surgery in mice in preparation for multiphoton imaging. Comparisons within our lab find that the method is requires less surgery time and has a lower average rate of complications due to dural bleeding than cranial window surgery with a rotary drill.

INTRODUCTION:

Cranial window surgery to prepare rodents for multiphoton imaging *in vivo* has become an important technique in neuroscience. The removal or thinning of bone is necessary to prepare the mouse for optical imaging with a multiphoton microscope. This surgery is performed either by completely removing an area of bone to expose the underlying dura (Holtmaat et al. 2009), or by thinning a region of bone without full removal from the dura (Yang et al. 2010). The thin skull approach may produce less inflammation and activation of microglia (Dorand et al. 2014) but provides a shallower depth of imaging, a smaller imaging window size (200 µm) and a limited time period during which the window can be imaged due to bone regrowth (Holtmaat et al. 2009). The addition of a polished and reinforced glass window (PoRTS) can increase the imaging size and imaging period but is difficult to perform (Drew et al. 2010).

Both current surgeries use a high speed rotary drill to thin or remove the bone from the skull. The thin skull technique also uses a scalpel after the drill to further thin the bone (Tang et al. 2010). The PoRTS technique requires the extra step of high speed polishing with grit (Drew et al. 2010). In a high speed rotary drill, an air powered turbine or electric motor causes the drill bit to spin at a high velocity. As rotary drills section both bone and soft tissue, there is a risk of damaging the dura and underlying blood vessels. The success of the surgery depends on the skill of the surgeon. In addition to these windows prepared with mechanical surgical methods, a chemical method of optically clearing the skull with different solutions has been developed (Wang et al. 2012, Yang et al. 2016, Vercellotti 2000). However, since piezoelectric surgery is a mechanical method of surgery, our comparisons here will be limited to other mechanical methods.

Piezoelectric surgical devices utilize ultrasonic vibrations to break down mineralized bone without damaging underlying soft tissue, and thus offer an approach to rapidly thin a large area of bone. In a piezoelectric surgical handpiece, the turbine is replaced by a stack of ceramic disks: when current is applied, the disks vibrate at ultrasonic frequencies. The vibrations are transferred through the handpiece to diamond coated tips to cut through bone without damaging soft tissues, an advantage over rotary drills that do not discriminate between tissue types. Piezoelectric surgery was originally developed for use in human by Tomaso Vercellotti and has led to improvements in dental and cranio-maxilofacial surgery (Vercellotti 2000, Vercellotti and Podesta 2007, Stubinger et al. 2015, Basheer et al. 2017).

Piezoelectric surgery has been used to create an osteotomy in Wistar rats and was found by magnetic resonance imaging (MRI) and histology to produce significantly less damage than a traditional dental drill (Pavlikova et al. 2011). The authors concluded that piezoelectric surgery was safe for removing the bone near soft brain tissue. Mice, however, have a thinner dura that is more easily damaged, and that study did not prepare windows for chronic optical imaging. Chronic imaging requires that blood vessels are not damaged and that blood clots do not form under the window. Damage to the dura leads to inflammation that causes the window to cloud, and activates microglia and the proliferation of reactive astrocytes. Here we have optimized piezoelectric surgery for mice to create both thin skull and full bone removal cranial windows suitable for chronic imaging. We compared this surgical technique to cranial window surgeries prepared with a high speed rotary drill.

PROTOCOL:

All procedures involving animals were performed according to the standards set by the Columbia University Medical Center Institutional Animal Care and Use Committee (IACUC). Euthanasia was performed via cervical dislocation under anesthesia with ketamine 100 mg/kg and xylazine 10 mg/kg injected Intraperitonealy. All surgical procedures were performed in a sterile manner (surgeon was wearing head cap, face mask, sterile gloves and clean disposable lab coat), and surgical tools were autoclaved between each use.

1.0 **Presurgical steps**

1.1 Autoclave all surgical instruments to ensure sterility.

1.2 Anesthetize C57bl6 mice with isoflurane (4% for induction and 1.5-2% for surgery). Pinch the hind toe every 10 min to ensure proper depth of anesthesia: increase anesthesia if vocalization or hind limb retraction is seen.

1.3 Place the mouse in the stereotaxic frame on a heating pad or calibrated water recirculating blanket set to 38°C.

1.4 Apply veterinary eye lubricant to the eyes to prevent drying.

1.5 Administer buprenorphine (0.1 mg/kg) subcutaneously to provide presurgical analgesia.

1.6 Remove the hair over the scalp with a 3 minute application of hair removal gel or by shaving with an electric razor.

1.7 Disinfect the scalp with three alternating applications of chlorhexidine or betadine and 70% ethanol using a cotton tipped applicator.

1.8 Inject 100 µl of bupivacaine diluted 50% in saline under the scalp to provide local anesthesia.

2.0 **Piezoelectic cranial window surgery**

2.1 Using autoclaved sterile surgical instruments, remove a 1 cm circle of scalp over the skull by cutting with surgical scissors in a circular pattern. Lift the scalp off of the skull exposing the periosteum tissue over the bone.

2.2 Use the tip of forceps to scrape the exposed bone clear of any remaining periosteum tissue: this is important to ensure that the dental cement will not fall off later.

2.3 Set the piezoelectric surgery unit to vibrate on the lowest setting. Note that higher settings may break blood vessels due to intense vibrations.

2.4 Fix the sterile circular tip to the handpiece. Note: we found the 4 mm circular tip to be well suited for our surgeries: the large tip size contributes to the speed of the surgery as the entire window can be thinned simultaneously.

2.5 Fill a 10 ml syringe with ice cold artificial cerebrospinal fluid and hold it in the other hand not holding the piezoelectric handpiece.

2.6 Irrigate the skull by dripping the ACSF from the syringe onto the skull at a rate of 1 ml/min. alternatively use a peristaltic pump positioned over the skull to free the use of the other hand. Note irrigation with cold ACSF is important to prevent overheating due to the friction from the high frequency vibrations.

2.7 Gently apply the vibrating surgical tip to the skull with a light circular motion (3 circles per 1 sec) and thin the bone to the desired depth to perform a thin skull preparation (5 to 10 min). Note we chose to make 4 mm windows that were thinned to 20 µm. However, the size of the window will vary with the size of the surgical tip, and the thickness of the bone can be adjusted to the desired depth based on the length of time spent applying the tip to the skull.

2.8 gently adjust the angle you hold the handpiece and change the angle of the tip as you apply pressure to the skull to thin the skull uniformly.

2.9 To perform a complete bone removal without leaving any thin bone behind, thin the bone until cracks are visible around the window area. Then remove the remaining flakes of thin bone with forceps without damaging the underlying dura.

2.10 Soak a 1mm piece of hemostatic collagen foam in cold ACSF. Hold the wet foam with forceps and place it on the exposed dura. Allow it to sit on the dura for about 30 sec to stop any micro bleeds from developing.

2.11 Use forceps to place a 4 mm glass coverslip laterally over the window that has been thinned into the bone.

2.12 Use the back of a small plastic or wooden cotton tipped applicator to apply approximately 100 µl of dental acrylic to the skull to hold the window in place.

3.0 **Post surgical care.**

3.1 Remove the mouse from the surgical apparatus and place it in a heated cage for recovery. Monitor it continuously until it has regained full consciousness (assessed by normal mobility, gait, and behavior).

3.2 Assess the animals twice a day for three days for manifestations of post-surgical pain including decreased activity, grooming, or food and water consumption, guarding behavior (e.g. limping or a hunched posture) or increased aggression. Do not return the animal to the company of other animals until it has fully recovered.

3.3 Administer Buprenorphine (0.05-0.1mg/kg) subcutaneously as an analgesic 8-12 hours after the surgery for 3 days. Monitor the area of the window closely following surgery for dehiscence, inflammation, and signs of infection. Note: If the animal does not return to baseline feeding and grooming behaviors, consult a veterinarian regarding possible interventions or euthanasia.

REPRESENTATIVE RESULTS:

Before proceeding with piezoelectric surgery, remove any residual periosteum from the skull. Once the skull is opaque and smooth (Figure 13a), the surgeon may begin piezoelectric surgery. When removing bone with the vibrating piezo tip, it is critical to irrigate the skull with ice cold ACSF. Proper irrigation is achieved when the bottom 1 mm of the tip is submerged in ACSF (Figure 13b). Without proper irrigation, the bone will overheat and damage the brain. After the skull has been thinned to the desired depth chosen by the surgeon, there may be some residual bleeding from blood vessels located in the bone. In order to rapidly cease all bleeding, apply a small 1 mm piece of collagen foam soaked in ACSF to the

area of the window. Let the collagen sit on the skull for approximately 30 seconds (Figure 13c). After the collagen foam is removed, the window will appear translucent, allowing clear visualization of the blood vessels in the dura. The dura will be intact without significant bruising. (Figure 13d). If the dura appears red and inflamed, it is likely due to broken blood vessels from too much pressure applied to the tip during the surgery. To protect the new window and prepare it for chronic imaging, a glass coverslip must be placed over the area. A properly applied glass coverslip will gently sit on top of the window and will not cause any damage to the area. The glass coverslip must cover the entire window. If the glass coverslip is properly applied to the skull, the window will remain translucent under the glass. All of the blood vessels in the dura will still be visible (figure 13e). Dental acrylic must be applied around the glass coverslip to permanently adhere it to the surface of the skull. The edges of the glass coverslip must also be covered in dental acrylic (figure 13f). We found that piezoelectric surgery is typically much faster than a traditional cranial window, taking around 10-12 min per surgery (figure 14A). We also found that there were less complications due to dura bruising and bleeding as observed by eye (figure 14B). A properly prepared window will allow multiphoton imaging of fluorescent indicators in cortical neurons *in vivo*. We chose to image the red calcium indicator JRGECO1a in cell bodies of layer 4 cortical neurons (figure 15A-3B). We were able to observe calcium transients in these cell bodies through the window prepared using PHASOR.

FIGURE AND TABLE LEGENDS:

Figure 13. Pictures of PHASOR. a) The skull after it has been properly prepared for PHASOR. All of the periosteal tissue has been removed, leaving a smooth and clean surface. b) A representative image of PHASOR in progress. The bottom 1 mm of the vibrating surgical tip is submerged in ice cold ACSF. The fluid is applied to the skull at a rate of 1 ml/min. A light circular motion is applied to the skull and the bone is thinned via ultrasonic vibrations. c) After the skull has been thinned, a 1 mm circular piece of collagen foam soaked in cold ACSF is allowed to rest on the window to stop any micro bleeds from the bone. d) A successful window with a translucent dura displays all of the intact blood vessels. There is no visible damage or bruising to the surface of the brain. e) A glass coverslip is placed over the window to protect

the surface of the brain. f) Dental acrylic is applied to the skull to permanently fix the glass coverslip over the window. Scale bar 1 mm in all images.

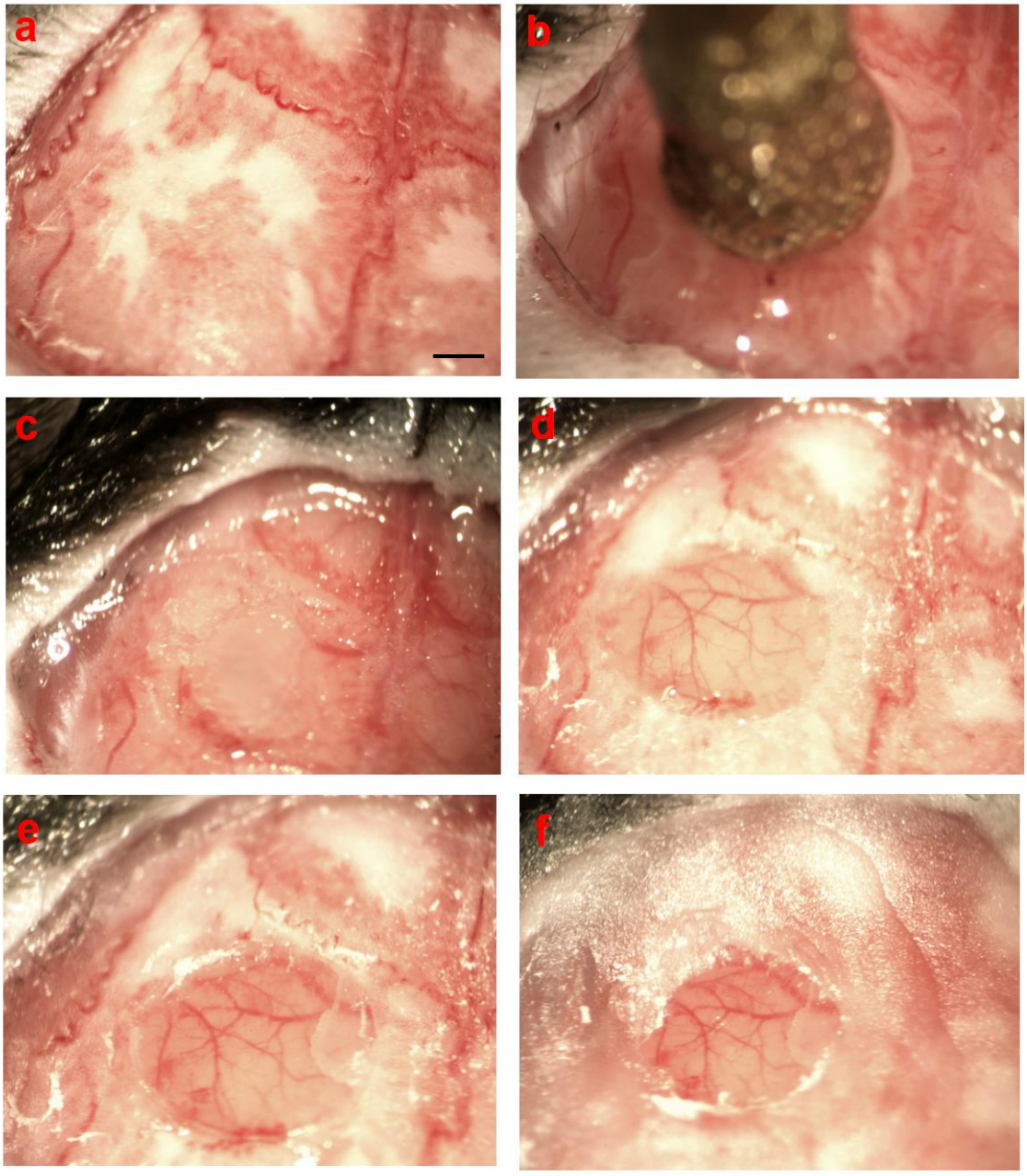

A

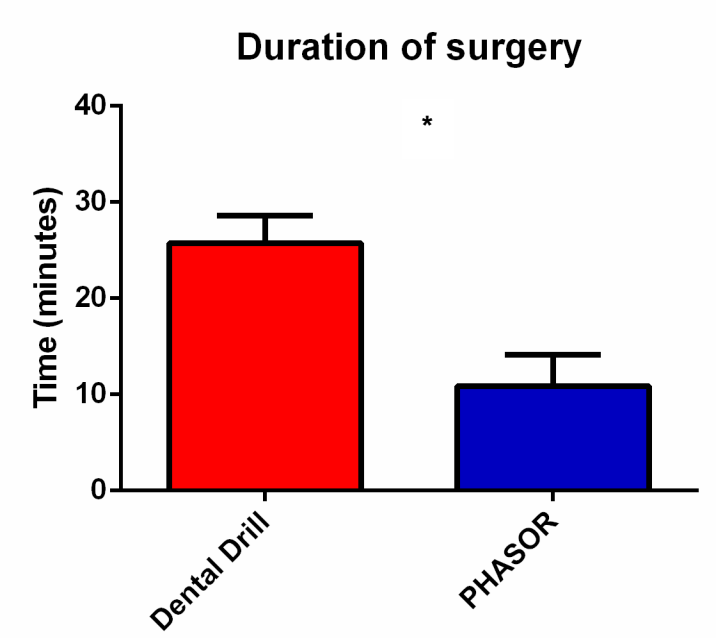

B

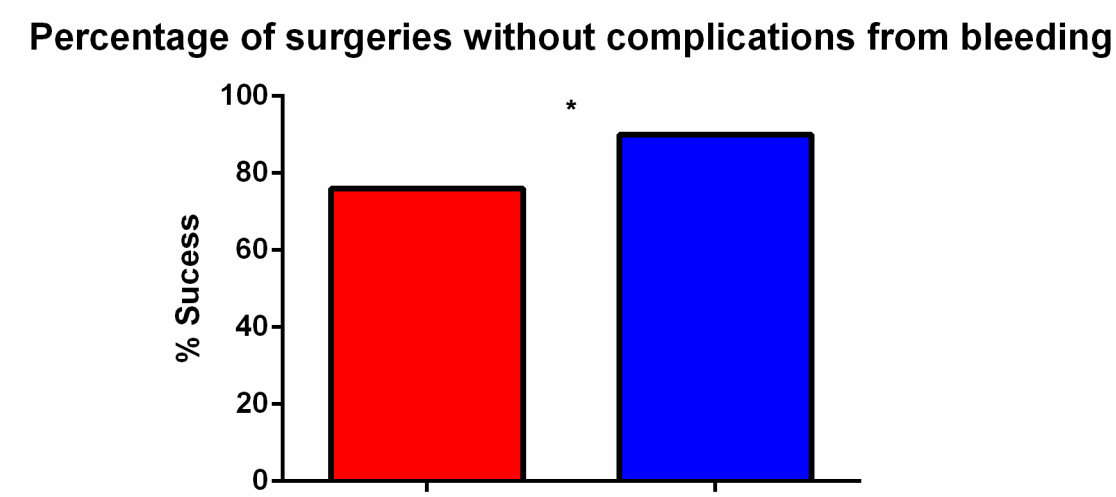

Figure 14. Comparison of success rate in training for PHASOR or dental drill surgery.
A) Average time per surgery was lower for PHASOR than dental drill surgeries ($p<0.05$, two tailed t test) n= 30 surgeries per group and average 10 surgeries per surgeon. B) The percentage of successful surgeries (defined as no bleeding or visible damage to the dura as observed by the surgeon's eye

through the objective set to 350X zoom) was higher for PHASOR than dental drill surgeries (n = 30 surgeries for each group, one tailed z test). Error bars show SD.

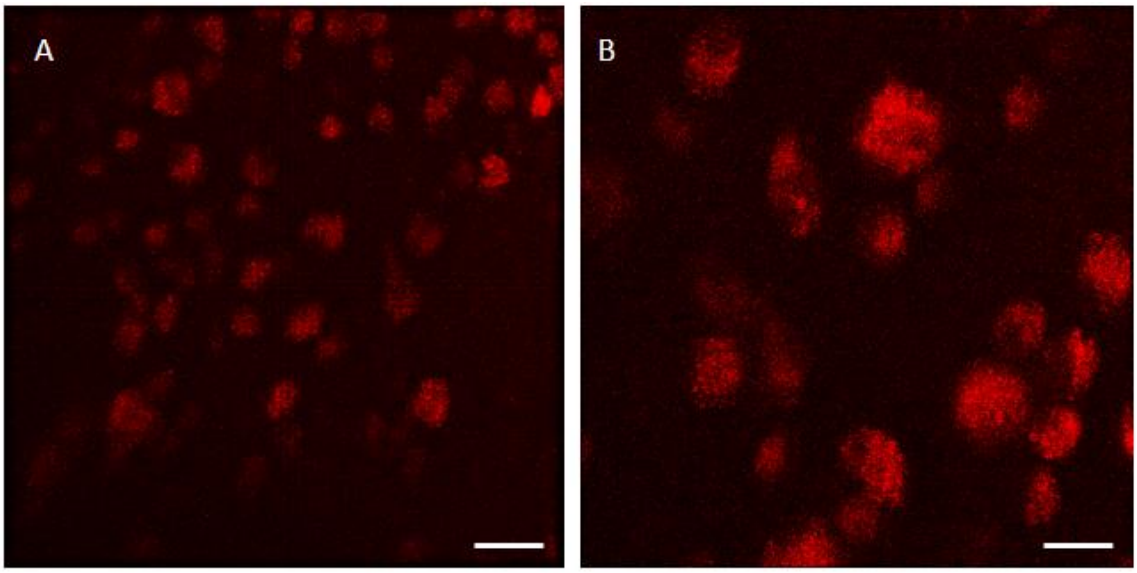

Figure 15. Multiphoton imaging *in vivo* through a cranial window thinned with PHASOR.
A) Calcium transients observed with the red calcium indicator JRGECO1a were imaged in layer 4 pyramidal neurons in murine motor cortex in vivo. Scale bar, 100 µm. B) The same window but different region of layer 4 motor cortex. Scale bar, 30 µm. Headfixed mouse with 3 mm window prepared with PHASOR. Imaged with a Prairie Ultima multiphoton microscope, 40x Olympus objective, 1040 nm excitation wavelength.

Name of Material/ Equipment	Company	Catalog Number	Comments/Description
Piezosurgery Touch	Mectron	5120062	Piezosurgery GP model has the same settings
Circular 4mm flat piezosurgery tip (# OT11)	Mectron	3370019	This tip was ideal for our windows but there are many other tips of different sizes available.
Stereotax frame	Kopf	963	
Mouse adaptor	Stoelting	51625	

Peristaltic pump for irrigation.	Cole-Parmer	WU-77120-42	Makes it easier to irrigate and frees up the other hand to provide stability. Irrigation can be performed by hand with a syringe if necessary.
Avitene Ultrafoam	Bard-Davol	1050020	Important to stop any minor bleeding instantly.
C&B Metabond	Parkell	S380	Much stronger than regular dental acrylic.
Artificial cerebro spinal fluid (ACSF)	Tocris	3525	
Puralube opthalmic ointment	Dechra	17033-211-38	
Mice	JAX	664	

Table 2. Equipment list.

DISCUSSION:

Modifications and troubleshooting

The surgery can be modified by changing the surgical tip. There are many different sizes of tip that can be applied to the handpiece. Changing the size or shape of the tip will result in different sized windows. In addition to the 4mm tip we also tried a 3mm tip and found it also worked well. Even with irrigation with ice cold ACSF, we were not able to get good results with tips that were too narrow (approximately .25 mm) due to the concentrated vibrations causing too much heat and burning the bone leading to damage to the underlying dura. We have not tried the multitude of other tips that are available, and we anticipate that other labs may find new applications for these different tips. While the surgery is relatively straightforward, we found that there are several steps that may require troubleshooting. The first is that the vibrating tip produces a lot of turbulence in the ACSF, which diminishes visibility and produces difficulty in ascertaining bone depth during the bone thinning step of the surgery. We recommend that if it is too difficult to see how thin the bone is, take a break to dry the skull and window by applying a sterile cotton swab to the side of the bone. Do not apply the cotton swab directly to the window, since the rough surface is damaging to thin bone. After checking the depth, reapply ACSF and continue with the surgery. We also

found that if there is damage to the dura, it is usually due to the surgeon putting too much pressure on the tip. Holding the handpiece more gently and applying less force will likely fix this problem. If the surgeon is forcibly scraping the tip on the bone, it will cause a break in the thin bone and damage the skull. Finally, if after thinning the bone, the underlying dura appears bruised , it is likely due to excess heat from the vibrations. Increasing the rate of ACSF flow will fix this issue.

Limitations of the technique. The main limitation of PHASOR is that the handpiece can thin the bone, but cannot remove all of the bone over the dura,: the diamond coated tip has small rough bumps, and the rubbing needed to thin the skull would abrade the dura and cause bleeding if it were used to remove all of the bone. Thus, the use of forceps is required to remove the remaining thin layer. While there is ongoing debate on whether imaging through a thin skull produces less inflammation and less proliferation of microglia and reactive astrocytes, in some cases a window with no bone remaining is preferred, e.g., to provide a greater depth of imaging[3].

Significance with respect to existing methods

We have optimized cranial window preparation for multiphoton imaging in mice. PHASOR is, to our knowledge, the first application of piezoelectric technique to rodent cranial window surgery for optical imaging. We find that the use of piezoelectric surgery in mice shares the advantages of increased speed and decreased adverse events also reported in humans (Vercellotti 2000, Vercellotti et al. 2001, Vercellotti and Podesta 2007, Stubinger et al. 2015). Utilization of the piezoelectric device resulted in faster surgeries (figure 2A) and fewer adverse events of bleeding when compared to a high-speed rotary drill (figure 2B). We also found, within our lab, that PHASOR was easier for new surgeons to learn than traditional approaches to cranial window surgery. Advantages of speed and ease of use are likely to differ among surgeons. Thin skull preparations typically require 30-45 min to thin the bone with a drill and scalpel (Yang et al. 2010), while the PHASOR approach typically requires less than 10 min.

We found that in windows prepared with PHASOR we were able to image calcium transients in layer 4 pyramidal neurons in motor cortex that had been transfected with adeno associated virus encoding the calcium indicator JRGECO1a (AAV9.Syn.NES-jRGECO1a.WPRE.SV40, UPENN Vector Core). We also found that, compared to a thin skull cranial window prepared with a rotary drill and scalpel, the imaging region was larger: while a thin skull prepared with a rotary drill and scalpel has an imaging window of 20 µm diameter (Yang et al. 2010), with PHASOR we were able to quickly thin an area of 3-4 mm. This is similar to the imaging window reported in with PoRTS (Drew et al. 2010). This larger window retains the benefit of rapid imaging reported for thin skull windows prepared with a dental drill and scalpel. Moreover, the window prepared with PHASOR can be immediately imaged, as opposed to traditional bone removal windows that may require weeks to heal before the window can be optimally imaged (Dorand et al. 2014).

Future applications:

We think this technique can be applied to study alterations in blood flow in the vessels under the dura. An important future study is to compare immunoreactivity of PHASOR with other methods of cranial window. This would be important in order to properly determine if PHASOR produces less inflammation in comparison to existing methods.

We hope that the piezoelectric surgical technique documented here will allow more labs to perform cranial windows and successfully use multiphoton imaging *in vivo*.

Critical steps

Make sure your handpiece is set to vibrate on the lowest setting and that the ACSF is being irrigated at a constant rate. The ice cold ACSF must be applied constantly or it will heat up and damage the dura. We found that ACSF must be applied at a rate of at least 1 ml/min. Either use a syringe held in the hand, or use a peristaltic pump, rather than the built in irrigation in the handpiece. The irrigation system in the handpiece ejects ACSF too forcefully and produces too much turbulence, which will significantly impair visibility.

ACKNOWLEDGMENTS:

Supported by the Brain & Behavior, Parkinson's and JPB Foundations, R01 MH108186 and R01

DA07418. F31 fellowship 1F31MH109293-01A1 to S C.

DISCLOSURES:

There are no disclosures.

THESIS PART 2: OPTICAL EXPERIMENTS IN THE STRIATUM

CHAPTER 5: GENERAL INTRODUCTION

OVERVIEW

In this chapter I will provide a review of the striatum, the main input nuclei in the basal ganglia. In subsequent chapters, I will describe the studies I performed on this system. In my first study, I used in vivo optical recording techniques to examine the synchrony in the indirect path between the left and right striatum during tasks of motor behavior. In a preliminary series of experiments included as an appendix, I examined the changes in dorsal striatal direct and indirect path firing rates during tasks of motor learning. Finally, I examined the firing rates of direct and indirect path neurons during motor tasks involving differential anxiety states.

The basal ganglia

The basal ganglia comprise a set of interconnected nuclei in the forebrain of vertebrates that play a critical role in modulating important functions including voluntary movement, motivation, reward, learning, and emotion. Dysfunction in the basal ganglia has been implicated in numerous diseases including Parkinson's disease, Huntington's disease, mood disorders, anxiety spectrum disorders, and drug addiction.

The nuclei that make up the basal ganglia include the striatum, globus pallidus, ventral pallidum, substantia nigra pars compacta (SNc), ventral tegmental area, subthalamic nuclei, and thalamus (Wichmann and DeLong 2016). In humans, the striatum is divided by both spatial location as well as function into dorsal and ventral components. The dorsal striatum is further composed of two nuclei, the caudate and putamen, which are separated by a series of motor neuron axon terminals termed the internal capsule. However, in rodents, the dorsal striatum is mostly homogenous without a clear anatomical distinction between the caudate and putamen. The ventral striatum is comprised of the nucleus accumbens (which can be further subdivided into the shell and core regions) and the olfactory tubercle.

The anatomy of the striatum

The circuitry of the basal ganglia is composed of four distinct cortico-striatal-cortico loops: prefrontal, motor, oculomotor, and limbic (Nambu 2008). Different cortical areas associated with each of the four loops synapse on the striatum, the main input nucleus of the basal ganglia. The work described in this thesis focuses on the motor loop in rodents. The rodent motor loop starts with glutamatergic input from the cortical areas, (primary motor (MI), supplementary motor area (SMA), and premotor cortex (PM)), which synapse on dendrites of the dorsal lateral somatomotor area of the striatum. Information processed in the striatum is passed to the output nuclei of the basal ganglia, the substantia nigra pars reticulata (SNr) and globus pallidus interna (GPi) through inhibitory GABAergic synapses. These nuclei form inhibitory GABAergic synapse on the thalamus which projects excitatory glutamatergic synapses back to cortical motor neurons forming the cortico-striatal-thalamo-cortical loop (Sulzer and Surmeier 2012, Obeso et al. 2008, Smith and Villalba 2008). This motor loop synapses in the thalamic ventral lateral nucleus (VLo and parvicellular part of the ventral anterior nucleus VApc. (Middleton et al. 2000, Hoover and Marshall 1999, Miyachi et al. 2006, Akkal et al. 2007). The thalamus, especially the midline and intralaminar nuclei, also sends glutamatergic excitatory inputs back to the striatum (Kreitzer 2009). In contrast to the dorsal striatum, the ventral striatum receives glutamatergic input from limbic cortical areas and orbitofrontal cortex and projects to the ventral pallidum (Gerfen 1984, Nakano et al. 2000).

The striatum can be further divided into patch and matrix subcompartments by the neurochemical markers expressed throughout the region. Histological stains for mu opioid receptors, substance P, and enkephalin have shown a patchy pattern that composes 10% of the striatum. The remaining 90% of the striatum and exhibits calbindin, somatostatin, and the cholinergic markers, acetylcholinesterase, and choline acetyltransferase, and is termed the matrix (Herkenham and Pert 1981, Graybiel 1986, Graybiel and Ragsdale 1978, Gerfen 1984, Gerfen et al. 1987, Moriwaki et al. 1996). DA is supplied to patches from specific ventral SNc neurons distinct from the SNc neurons that supply the rest of the dorsal striatum (Jimenez-Castellanos and Graybiel 1987, Prensa and Parent 2001).

While both the dorsal and ventral striatum are modulated by DA, the source of the modulation differs for each region. Dopaminergic neurons arising from the ventral tegmental area (VTA) comprise two main pathways. Dopaminergic neurons projecting to the cortex form the mesocortical dopaminergic pathway,

while dopaminergic neurons projecting to the ventral striatum and limbic areas form the mesolimbic pathway. In addition, dopaminergic neurons in the substantia nigra pars compacta project to the dorsal striatum and comprise the nigrostriatal dopaminergic pathway (Sulzer and Surmeier 2012).

The direct and indirect paths of the striatum.

The striatum is composed of approximately 95% GABAergic spiny projection neurons (SPNs) and 5% interneurons. The SPNs can be grouped into two circuits according to anatomic projection targets and receptor expression patterns termed the direct and indirect paths (Kreitzer 2009). The direct pathway comprises SPNs projecting directly to the GABAergic output nuclei of the basal ganglia, the SNr and the Gpi, while the indirect pathway comprises SPNs projecting to the globus pallidus externa (GPe) and subthalamic nucleus. The direct path SPNs (dSPNs) express Gs coupled DA D1 receptors and their activity results in inhibition of the GABAergic output nuclei of the basal ganglia which releases the thalamic motor nuclei from inhibition (**Figure 16**). The indirect path SPNs (iSPNs) express Gi/o coupled DA D2 and adenosine A2A receptors (Obeso et al. 2008, Kravitz and Kreitzer 2012). There is also some overlap of D1 and D2 receptors in the same SPNs (Aizman et al. 2000). The iSPNs form inhibitory synapses on the GPe, releasing the GPi from inhibition and subsequently inhibiting the thalamic motor nuclei. The hyperdirect path comprises a cortico-subthalamo-pallidal path. In this path, cortical motor neurons bypass the striatum and project to the subthalamic nucleus where they form excitatory glutamatergic synapses. The subthalamic nucleus then projects glutamaterigic synapses to both the GPe and the GPi/SNr. The hyperdirect path has been hypothesized to play an important role in motor pattern selection (Nambu 2008). Similar to ventral striatum, SPNs in the patches receive input from limbic and frontal cortex, while the matrix SPNs receives input from sensorimotor cortex and the thalamus (Donoghue and Herkenham 1986, Kincaid and Wilson 1996, Ragsdale and Graybiel 1978).

There are some exceptions to the classic direct and indirect paths. It has been found that in addition to the main projections to the GPi/SNR, a portion of dSPNs project axon collaterals to the GPe. However, the iSPNs project only to the GPe and do not project collaterals to the GPi/SNR (Wu et al. 2000, Fujiyama et al. 2011).

Anatomic and electrophysiological analysis shows that rather than comprising two segregated circuits, the direct and indirect paths SPNs are composed of heterogeneous subgroups. This heterogeneity is present at several levels of the motor loop. At the macrocircuit level, the SPNs can be grouped into subpopulations by cortical and thalamic input. The cortical input areas, MI, SMA, and PM, form synapses on different groups of direct and indirect SPNs with some overlap. Similarly, a portion of SPNs receive reciprocal projections from both the GPe and thalamus (Nambu 2008). The dSPNs receive excitatory glutamatergic input from the cortex via cortico-striatal pathway and the thalamus via thalamostriatal projecting neurons. The iSPNs receive the majority of the corticostriatal axons from sensorimotor cortex (Berretta et al. 1997, Parthasarathy and Graybiel 1997). At the microcircuit level, there is even greater

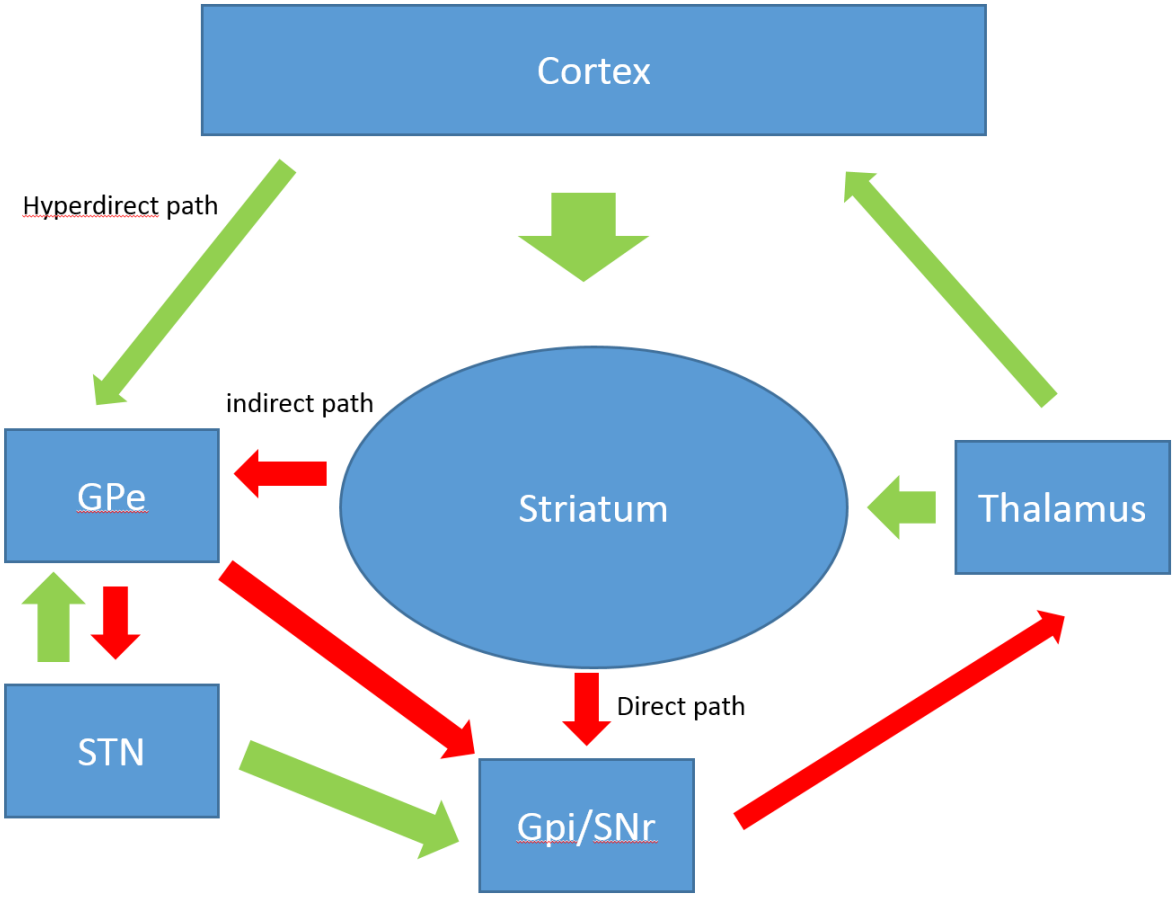

Figure 16. Direct and indirect paths of the striatum. The direct path projects directly from the striatum to the GPi/SNR, while the indirect path projects to the GPE before projecting to the GPi/SNr.

diversity within each path. Both the indirect and direct path SPNs form inhibitory collateral synapses: a

single SPN in either path may receive thousands of axon collaterals from both dSPNs and iSPNs (**Figure 16**) (Taverna et al. 2008). Finally, 5% of the striatum is composed of several types of interneurons that receive cortical input and form synapses on SPNs from both paths (**Figure 17**). Although they comprise a relatively small percentage of the total neurons of the striatum, some interneurons form synapses on hundreds of SPNs, and a single SPN receives input from multiple interneurons, further contributing to the heterogeneity of the complex striatal microciruitry (Kreitzer 2009, Gittis and Kreitzer 2012).

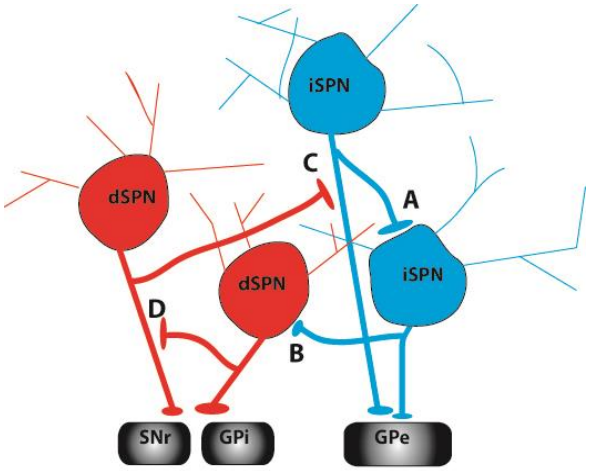

Figure 17. **Four types of SPN axon collaterals in order of most commonly observed to least commonly observed**. *(A) iSPN to iSPN. (B) iSPN to dSPN. (C) dSPN to iSPN. (D) dSPN to dSPN.*

SPNs of the direct and indirect paths have similar electrophysiological properties, which makes them difficult to distinguish in either acute slice or in vivo (Nambu 2008). A defining characteristic of striatal SPN recordings is a transition between up and down states. SPNs usually have a hyperpolarized resting membrane potential between -90mv to -70mv, that is termed the down state. When SPNs fire, they depolarize to -60 to -40mv, termed the up state. Striatal neurons do not display tonic activity and are usually quiet unless stimuli is sufficient to overcome their significant resting hyperpolarization in the down state and invoke a transition to the up state. Because of this firing pattern, SPNs are referred to as phasically active neurons (Nambu 2008). The down state hyperpolarized resting membrane potential

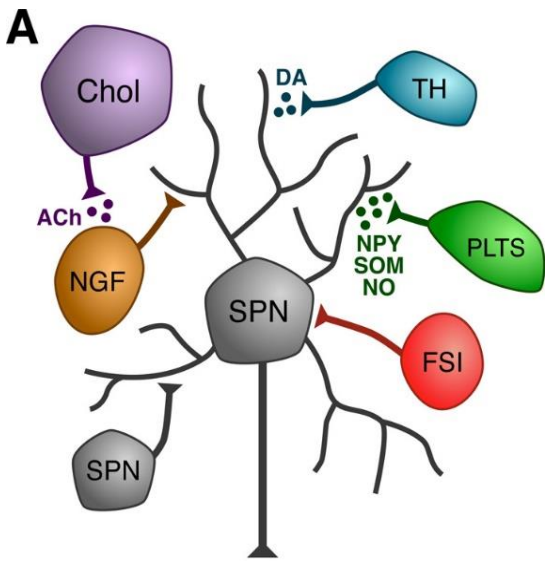

Figure 18. Different types of interneurons and microcircuit interactions in the striatum. [Figure is adapted from Gittis and Kreitzer 2012]

is largely due to polarizing current from inward rectifying potassium channels (Kirs) (Kita 1984, Nisenbaum and Wilson 1995, Mermelstein et al. 1998, Uchimura et al. 1989). Transition between states only occurs when glutamatergic input is strong (Blackwell 2003). Depolarization activates fast-inactivating Kv4.2 and slow-inactivating KV1.2 potassium channels and inhibits the Kirs (Shen et al. 2004, 2005, Surmeier et al. 1989).

Striatal interneurons

Four different types of interneurons make up the other 5% of the striatal neuron population. In contrast to SPNs, interneurons do not possess dendritic spines. Interneurons can be categorized into two groups based on the neurotransmitter they release: GABAergic interneurons, and cholinergic interneurons. The GABAergic interneurons can be further divided into three types: 1. Fast spiking (FS) parvalbumin-positive (PV+), 2. Low threshold spiking (LTS) somatostatin (SOM+), neuropeptide Y and nitric oxide synthase positive, 3 calretinin-positive. Each type of GABAergic interneuron has a characteristic profile.

FS PV+ interneurons are most dense in the dorsolateral striatum and are excited by direct glutamatergic synapses from the cortex and the thalamus. Optogenetic studies have shown that FS interneurons form inhibitory synapses on the soma and proximal dendrites of SPNs and other interneurons (Straub et al. 2016). These interneurons are modulated by DA through excitatory D5 receptors and by acetylcholine through excitatory nicotinic receptors. They exhibit high frequency firing rates and short duration spiking (Kreitzer 2009). While they only constitute a small portion of the striatum, FS interneurons play an important role in regulating striatal output through extensive synapses, In addition to forming multiple synapses per SPN, individual interneurons form inhibitory synapses on hundreds of different SPNs and mediate feed forward inhibition (Tepper et al. 2004, Tepper et al. 2010). Interestingly, FS interneurons form gap junctions with other FS interneurons, enabling high speed transmission of signals and modulation of striatal motor output (Hjorth et al. 2009, Kreitzer 2009).

In a manner similar to FS interneurons, LTS interneurons receive excitatory glutamatergic synapses from both cortico-striatal and thalamo-striatal axons, and form inhibitory synapses on SPNs. Recent use of optogenetic and multiphoton imaging has shown that LTS interneurons mainly synapse on the distal dendritic regions of distant SPNs and other interneurons (Straub et al. 2016). Histological studies of LTS

interneurons show that they express somatostatin, neuropeotide Y and nitric oxide synthase (Chesselet and Graybiel 1986, Kubota and Kawaguchi 1993, Smith and Parent 1986). In contrast to FS interneurons, LTS interneurons receive direct dopaminergic synapses (Hidaka and Totterdell 2001). LTS interneurons have a distinct electrophysiologic profile with plateau potentials and low-threshold spikes (Kreitzer 2009), and display 3Hz to 7Hz membrane oscillations dependent on calcium currents (Song et al. 2016). Like FS interneurons, LTS express excitatory D5 receptors, but express muscarinic M1 and M2 receptors rather than nicotinic receptors (Rivera et al. 2002, Ariano and Kenny 1989, Bernard et al.1992 and 1998)

Calretinin-positive interneurons (CR+ interneurons) are the least studied of the three GABAergic interneurons and account for only .5% of all striatal neurons (Tepper et al. 2010, Rymar et al. 2004). Immunostaining has so far identified three morphologically different types of CR+ interneuron, however the lack of a transgenic CR+ mouse line has limited the study of their electrophysiological profile (Tepper et al. 2010).

Cholinergic interneurons account for about 1% of all striatal neurons (Apicella 2017) and both synapse on, and receive synapses from, SPNs (Tanimura et al. 2017, Izzo and Bolam 1988, Bolam 1986). Cholinergic interneurons also play a direct role in exciting FS interneurons through nicotinic receptors (Koos and Tepper 2002). Recent studies of using Designer Receptors Exclusively Activated by Designer Drugs (DREADD) have shown that cholinergic interneurons modulate striatal output and increase locomotion (Aldrin-Kirk et al. 2018). Cholinergic interneurons may play a role in the processing of salient stimuli and exhibit pauses in tonic activity during cues signaling prediction of reward (Greybiel 1994, Morris 2004).

In contrast to FS and LTS interneurons, excitatory glutamatergic innervation of cholinergic interneurons is mostly through the thalamo-striatal path and partially through the cortico-striatal path (Lapper and Bolam 1992, Thomas et al. 2000). Cholinergic interneurons are tonically active at a rate of 2-10 Hz due to hyperpolarization activated cation channels as well as sodium channels (Wilson and Goldberg 2006, Bennet et al. 2000).

Cholinergic interneurons are modulated by both DA through inhibitory high affinity D2 inhibitory receptors and through excitatory D5 receptors. D2 receptor signaling results in inhibition of voltage gated sodium

channels and hyperpolarization of the cell (Zhang et al. 2017) while D5 activation results in elevated cAMP and depolarization of the cell. They are also modulated by opioid peptides through delta opioid receptors which has been hypothesized to play a role in predictive learning (Heath et al. 2017). Finally, they are modulated by acetylcholine through M2 and M4 muscarinic receptors. The M2 receptor is present as an autoreceptor on presynaptic terminals and reduces release of acetylcholine (Hersch et al. 1994, Yan and Surmeier 1996).

Cholinergic interneurons also play a role in DA modulation and increase DA release by increasing intracellular calcium via ionotropic nicotinic receptors on presynaptic DA terminals (Exley and Cragg 2008, Cachope et al. 2012) and may play a role in levodopa induced dyskinesia (Aldrin-Kirk et al. 2018, Cortes et al. 2017). Cholinergic interneurons can also decrease DA release by binding muscarinic M5 metabotropic receptors on DA terminals (Foster et al. 2014).

DA and cannabinoid neuromodulation of the striatum

DA modulates activity over the entire striatum. DA release sites are usually en passant on the axons, and near the dendritic shafts of cortico-striatal glutamatergic synapses (Freund et al. 1984). Tonic levels of DA are widely suspected to preferentially bind high affinity D2 receptors. In contrast, DA neuron bursting, as occurs in response to salient stimuli, is theorized to activate lower affinity D1 receptors (Nambu 2008).

DA plays a critical role in SPN up and down state transitions. In the up state, L-type currents are enhanced by excitatory D1 receptors (Carter and Sabatini 2004, Surmeier et al. 1995).

D2 receptors are mainly expressed on iSPNs and have a higher affinity for DA than D1 receptors. In the up state, in contrast to D1 receptors, D2 receptors inhibit L-type calcium currents. This results in decreased SPN firing (Kreitzer 2009).

In addition to its role in modulating SPN excitability and state changes, DA also modulates glutamate release from both the corticostriatal and thalamostriatal excitatory synapses onto medium spiny neurons. The D2 receptor can reduce glutamate release from cortical inputs to SPNs terminals of low activity during high frequency stimulation, mostly due to retrograde cannabinoid release (Bamford et al. 2009, Yin and Lovinger 2005). This presynaptic change in corticostrital plasticity is termed chronic presynaptic

depression CPD. (Bamford 2008, Storey et al. 2016). These changes selectively inhibit the less active corticostriatal terminals, and in this way, DA acts as a high pass filter.

Through signaling through cannabinoid receptors, endocannabinoids play an important role in modulating striatal DA release and striatal plasticity. In the striatum, endocannabinoids are retrograde transmitters that mainly act on presynaptic CB1 receptor where they modulate short-term and long-term depression of synaptic transmission (Heinbockel et al. 2005). Endocannabinoids are fatty acid neurotransmitters. CB1 receptors in the dorsal striatum are located on presynaptic corticostriatal and thalamostriatal synapses as well as on GABAergic interneurons and SPN collaterals (Lafourcade et al. 2007, Fitzgerald et al. 2012). By acting at postsynaptic D2 receptors on SPNs with simultaneous mGluR1 activation, DA drives SPNs to release endocanabinoids that bind the cannabinoid receptor CB1 on presynaptic corticostriatal and thalamostriatal synapses and induces long term depression LTD (Wong et al. 2015). This form of corticostriatal LTD has been implicated in motor learning and action initiation (Jin et al. 2014, Hilario and Costa 2008). The cannabinoid system is also activated by Δ^9Tetrahydrocannabinol (THC), a psychoactive compound in Cannabis sativa (marijuana) plants.

There has been recent interest in cannabinoid modulating compounds as antiepileptics (Friedman and Devinski 2015). Use of Cannabis sativa for seizures is not an entirely new concept, as references to cannabis in the treatment of epilepsy goes as far back as ancient Sumeria in 1800 B.C. (Schultes 1973) Recent studies have shown that the active antiepileptic compound is cannabidiol ,which is not psychoactive, while THC is not thought to play a critical role in seizure suppression (Rosenberg et al. 2015, Filloux et al. 2015). Additionally, animal models demonstrate cannabidiol efficacy in models of focal epilepsy, and it is possible that it may soon join the other broad spectrum antiepileptics as standard of care (Devinsky et al. 2017).

The role of the striatum in motor behavior.

Several models have been proposed to explain how the direct and indirect paths function to influence motor behavior. The classical “go nogo” model, first proposed by Albin and DeLong, postulates that the two paths act in opposition to each other (Albin et al. 1989). Activation of the direct path causes movement while activation of the indirect path inhibits movement. This hypothesis was originally based on

the predicted downstream effects on thalamic motor nuclei of inhibiting the GABAergic output nuclei of the direct and indirect paths. This theory arose from studies showing motor deficits resulting from surgical lesions of basal ganglia output nuclei in primates. Later support came from observations that a specific immunotoxin mediated lesion of the entire indirect path resulted in increases in locomotion (Sano et al. 2003). In a recent study supporting the classic go nogo interpretation of the paths, optogenetic activation of the direct path neurons via channelrhodopsin resulted in increased locomotion while optogenetic activation of the indirect path neurons resulted in freezing, bradykinesia, and decreased locomotion (Kravitz et al. 2010). However, this study modeled all of the neurons in either the direct or indirect paths as a homogenous group, and using optogenetic techniques to put all of the dSPNs or iSPNs in the up state overrides the complex signal filtration process that occurs with natural movement.

In concordance with DeLong's original studies on behaving primates, a more recent model hypothesizes that the direct and indirect SPNs require coordinated and concurrent activity to modulate motor behavior (Nambu 2008, Cui et al. 2013, Mink 2003, Chan 2005). In this theory, both the direct and indirect paths are active at the same time. The direct pathway supports selection of the intended motor pattern while the indirect path simultaneously suppresses competing motor patterns. This theory of the striatum as a complex processor, rather than simply two opposing circuits, is supported by anatomic and electrophysiological analysis showing that rather than comprising two opposing segregated circuits, the direct and indirect paths SPNs form synapses on each other. This model was strongly supported when in vivo optical recordings from fiber optic implants in mice expressing the genetically encoded calcium indicator GCaMP3 in dSPNs or iSPNs showed that the levels of activity in the direct and indirect path SPNs are highest before movement initiation and during movement (Cui et al. 2013). Additionally, activity in both paths are lowest during stasis. While this study was able to show general activity, single photon counting does not have the optical resolution to record from subpopulations within the direct and indirect paths. These findings were confirmed by optogenetic aided electrophysiological recordings, which found that both paths were activity during execution of motor patterns, and that individual neurons would fire during specific parts of the action sequence (Jin et al. 2014). In a more recent study, Klaus et al. 2017, used a GRIN lens implanted in the dorsolateral striatum to record from the dSPNs and iSPNs with high spatial and temporal resolution. This technique allowed recording from populations of several hundred

neurons that expressed the improved calcium indicator GCaMP6f (Chen et al. 2013). They were able to determine that ensembles of SPNs in close spatial proximity are active during specific actions. They also found that similar actions recruited overlapping ensembles that were more closely located (Klaus et al. 2017).

In addition to glutamatergic input, SPNs also receive GABAergic corticostriatal input from interneurons in primary (M1) and secondary (M2) motor cortices (Rock et al. 2016). Optogenetic activation of PV+ in M1 and SOM+ projecting interneurons in M2 result in inhibition of locomotion while optogenetic activation of SOM+ interneurons in M1 results in increased locomotion (Melzer et al. 2017).

Striatal dysfunction in motor disease.

Dysfunction in the striatum plays an important role in several motor diseases, the most prevalent of which is Parkinson's disease. Parkinson's is the second most common neurodegenerative disease after Alzheimer's. and affects over ten million people worldwide, with a combined health burden In the United States of over 25 billion dollars. The disease is characterized by the degeneration of the dopaminergic projection neurons in the substantia nigra pars compacta (SNc), resulting in a striatal DA deficiency (Sulzer and Surmeier 2012, Obeso et al. 2008, Smith and Villalba 2008, Kreitzer and Berke 2011). This DA deficiency causes widespread changes in the complex motor circuitry of the striatum leading to characteristic motor symptoms, including bradykinesia (slow and reduced movement and reflexes), akinesia (loss of voluntary movement), muscle rigidity and resting tremor (Albin et al. 1989, Hammond et al. 2007, Hernandez et al. 2013).

All striatal neurons express DA receptors, and dopaminergic projection neurons from the SNc play a critical modulatory role that is essential to the normal function of all neurons in the motor loop of the striatum (Sulzer and Surmeier 2012). In the normal state, the SNc projection neurons have low frequency tonic activity and maintain a tonic level of DA that appears to bind high affinity D2 receptors, resulting in inhibition of indirect path SPNs. In response to stimuli, the SNc fires higher frequency bursts, resulting in a higher level of striatal DA available to bind lower affinity D1 receptors and increase excitability of the direct path SPNs (Kreitzer 2009). In Parkinson's, loss of DA is thought to result in a pathological over-excitation of the indirect path and corresponding decrease in excitability of the direct path (Delong and

Wichmorann 2009, Hammond et al. 2007, Sulzer and Surmeier 2012, Jaidar et al. 2010). Chronic DA depletion also causes pathological changes to the interneurons which further disrupts the microcircuitry and normal function of the SPNs (Taverna et al. 2008). The FS interneuron innervation of medium spiny neurons doubles leading to abnormal iSPN synchrony (Gittis and Kreitzer 2012). Due to a loss of inhibitory DA tone, cholinergic interneurons increase firing and begin to fire in synchronous patterns (Ding 2008, Raj 2001). Additionally, loss of DA leads to deterioration of the collaterals between SPNs (Taverna 2008). While the global changes to the striatum in the parkinsonian state have been quantified, it is unknown how DA depletion affects the subpopulations of dSPNs and iSPNs (Bevan et al. 2002).

In contrast to Parkinson's, Huntington's disease is characterized by loss of SPNs, with iSPN death more prevalent in the early stages (Reiner et al. 1988). This loss of the indirect path leads to hyperkinetic movements that characterize the disorder and supports the theory that the indirect path works to suppress competing motor programs.

CHAPTER 6: *IN VIVO* RECORDING FROM THE DIRECT AND INDIRECT PATHS REVEALS INCREASED FIRING IN A MOUSE MODEL OF ANXIETY

ABSTRACT

Anxiety disorders are the most common class of mental illness worldwide, costing more than 40 billion dollars in the US. Human magnetic resonance imaging studies implicate dysfunction in the striatum and increased striatal volume in the pathology of anxiety. The dorsal striatum is largely comprised of spiny projection neurons (SPNs) that project through the basal ganglia circuitry in two major pathways, termed the direct and indirect paths. Direct pathway SPNs express DA D1 receptors while indirect pathway SPNs (iSPNs) express DA D2 receptors. The activity of the dSPNs and iPSNs during tasks of anxiety have never been examined *in vivo*. We hypothesized that these neurons may show differential activation depending on the anxiety state of the mouse.

We used time correlated single photon counting (TCSPC) to record neuronal activity in the dSPNs and iSPNs during the elevated plus maze task of anxiety. TCSPC is an in vivo optical recording technique that was first applied to neuroscience by Cui et al. 2013. In this technique, a single mode optical fiber is implanted in the brain of a mouse. Neurons are then transfected with a viral vector expressing a calcium indicator such as GCaMP. A blue laser is pulsed into the brain through the fiber to excite the GCaMP to emit green light. This green light travels through the fiber where it is measured by a photo detector. The photons measured with this technique can be precisely measured by time. The intensity of the fluorescence from GCaMP can be used to determine the degree of neuronal activation and is a proxy for neuronal firing rate (Cui et al. 2013). Using transistor transistor logic (TTL) pulses, the recording time stamps generated by the TCSPC machine can be matched to video recorded with a high speed camera. This allows matching specific mouse behaviors to activation of specific groups of neurons.

The elevated plus maze, consists of two open and two closed arms. Time spent in the closed arms is thought to be associated with a lower anxiety state than the open arms. D1-Cre (direct path) and A2A-Cre (indirect path) mice were injected with AAV9.Flex.GCaMP6f virus. Imaging fibers were implanted in the dorsal lateral striatum. Mice were recorded with a high speed video camera framelocked to the TCSPC

sampling rate. This enabled us to correlate anxiety related behaviors with GCaMP6f changes in fluorescence. Both the dSPNs and iSPNs also showed a significantly higher rate of firing the closed arms of the maze (P<.05). Utilizing high speed video analysis, we concluded that the increased calcium transients in the dSPNs correlated with behaviors that are associated with a lower anxiety state.

INTRODUCTION

Fear is an acute response of increased arousal and somatic symptoms in the presence of negative stimuli, while anxiety occurs in the absence of a proximal threat (Calhoon and Tye 2015). In the proper context, both anxiety and fear have potentially useful evolutionary benefits. Increased vigilance, and stimulation of the sympathetic nervous system can aid avoidance or escape from danger and lead to increased survival of an individual. Excessive, and pathological levels of inappropriate anxiety, however, can lead to sever impairment of daily living. Anxiety disorders, including obsessive compulsive disorder (OCD) and generalized anxiety disorder (GAD) are the most common class of mental illness worldwide, costing more than 40$ billion in the US and causing significant functional impairment (Andlin-sobocki and Wittchen 2005, Hoffman et al. 2008). The DSM-5 symptoms of (GAD) are characterized by excessive and difficult to control anxiety or worry about topics events or activities that interfere with daily living. The disorder is also associated with several other symptoms such as restlessness, fatigue, difficulty sleeping, difficulty concentrating, irritability, somatic symptoms.

The circuit most studied in anxiety involves two loops. First, threatening stimuli is detected by the sensory systems and flows in a forward circular loop between the amygdala, bed nucleus of the stria terminalis (BNST), ventral hippocampus (vHPC) and medial prefrontal cortex (mPFC). Then information flows through this loop in the reverse direction via reciprocal projections. Importance is assigned to the stimuli in the forward loop, and this importance is revaluated in the backwards loop (Allsop et al. 2014, Calhoon and Tye 2015).

In addition to the structures that comprise the anxiety loops, the striatum has also been implicated as playing a potential role in anxiety disorders. Dysfunction in the striatum and increased striatal volume on human magnetic resonance imaging (MRI) studies has been implicated in the pathology of anxiety. In

anxiety disorders, the increased sensitivity to a perceived possibility of future threat to the individual is conceptualized as intolerance of uncertainty (IU). Individuals with GAD show increased volume in the dorsal striatum (caudate and putamen), as assessed by structural MRI, compared to healthy controls. The levels of IU also positively correlate with the increase in volume (Hilbert et al. 2015). A recent meta-analysis of volex-based morphometry studies found that individuals with OCD and other anxiety disorders showed increased bilateral gray matter in the dorsal striatum (caudate) compared to healthy controls. However a reduction in matter was seen with individuals with posttraumatic stress disorder and panic disorder (Radua et al. 2010). These changes in striatal volume seem to occur on a gradient, and are seen even in individuals who have increased anxiety that does not reach pathological levels. Additionally, striatal volume assessed with MRI recently showed that in healthy individuals, the volume of the dorsal striatum, especially putamen was positivity correlated with increased IU (Kim et al. 2017). In patients with OCD refractory to treatment, deep brain stimulation (DBS) of the nucleus accumbens can provide an effective but invasive treatment that provides relief from the symptoms (Denys et al. 2010, Gabriels et al. 2003, Greenberg et al. 2010). Finally, in rat models of anxiety, DBS in both the ventral and dorsal striatum was found to reduce anxiety (Dijk et al. 2013).

The dorsal striatum is largely composed of GABAergic spiny projection neurons. Striatal SPNs comprise two major circuits. The SPNs expressing D1 receptors (dSPNs) maintain a direct projection to the substantia nigra pars reticulata (SNr) and globus pallidus externa (GPe), termed the direct pathway. SPNs expressing D2 receptors (iSPNs) trigger a multisynaptic circuit, synapsing in the globus pallidus interna (GPi), which then projects to the SNr /GPe, termed the indirect pathway. Both direct and indirect pathway SPN activity are modulated by dopaminergic projections from the SNc. These paths can be further divided into the associative and sensorimotor paths depending on their cortical input. The SPNs in the dorsal medial striatum (DMS) receive input from the mPFC and cortical association areas and comprises the associative path, while the SPNS in the DLS receive cortical input from sensory and motor areas and comprise the sensorimotor path.

Anxiety states can be measured in the mouse through different behavioral paradigms. One of the most widely used is the elevated plus maze. In this task, a maze is constructed in the shape of a plus symbol

with four rectangular arms of equal length. Two of the arms are surrounded by walls and the other two arms are left open. The maze is elevated above the ground. The mouse is placed in the center of the maze and is allowed to explore freely for a period of time (usually 5 to 10 minutes). The purpose of this task is to evaluate anxiety-like behaviors in mice by observing their motivation to explore the open areas of the maze. Since the mouse will naturally avoid the open arms of the maze, the time in the open arms can be used as a proxy of the anxiety state of the animal (Walf and Frye 2007). This behavioral paradigm has been both genetically and pharmacologically validated. Anxiolytic drugs, used to treat individuals with GAD, increase the time spent in the open arms of the maze, while anxiogenic drugs reduce the time in the open arms (Pellow et al. 1985, Lister 1987, Shepherd et al. 1994). In addition to the time spent in the open and closed arms of the maze, other behaviors like head dipping, grooming, and rearing are associated with a lower anxiety state and provide further information regarding the animal's anxiety state (Shepherd et al. 1994, Braun et al. 2011, Heredia et al. 2013).

In mouse models of anxiety, the striatum has been implicated in behaviors associated with in the elevated plus maze. Targeted ablation of PV interneurons in the dorsal striatum, which has been shown to disrupt the direct and indirect paths, reduces the time spent in the open arms of the elevated plus maze (Xu et al. 2016). Ablation of dopaminergic projections to the dorsal striatum with the neurotoxin MPP+ increases anxiety-like behaviors and decreases the time spent in the open arms of in the elevated plus maze (Cunha et al. 2017). Despite recordings from hippocampus, prefrontal cortex, and amygdala during the elevated plus maze, little is known about the firing patterns of the dorsal striatal direct and indirect path neurons during the elevated plus maze (Carvalho et al. 2005). We used time correlated single photon counting (TCSPC) to distinguish dSPNs and iSPNs activity *in vivo* using the genetically encoded calcium indicator GCaMP to measure calcium transients, which serves as a proxy of somatodendritic action potentials (Chen et al. 2013). Time correlated single photon counting (TCSPC) of fluorescence changes in GCaMP has recently been applied to image dSPNs and iSPNs activity in awake behaving healthy mice (Cui et al. 2013, Kupferschmidt et al. 2017), but has not yet been applied to study changes that occur in behavioral models of anxiety. We hypothesized that the direct and indirect paths of the dorsal striatum may show differential firing depending on the anxiety state of the mouse.

Because the SPNs of the associative path receive input from cortical association areas involved in the main anxiety processing loops such as the mPFC. We chose to record from the dSPNs and iSPNs in the DMS. We transfected mice expressing cre recombinase in A2A-receptor-expressing neurons and D1-receptor expressing neurons with AAV9 Flex GCaMP6f virus into DMS, and implanted imaging fibers in the same site using TCSP. Mice were recorded with a high speed video camera framelocked to the sampling rate of the time correlated single photon counting machine enabling behaviors to be correlated with calcium transient changes with millisecond precision.

METHODS

Mice

Adult 8 week old male D1-Cre (GENSAT FK-150) and A2A-Cre (MMRRC 036158) mice were housed in a reverse light cycle room. All behavioral experiments were performed in the dark cycle of the mouse. All procedures were conducted in accordance with Institutional Animal Care and Use Committee (IACUC) of the New York State Psychiatric Institute.

Viral injection and fiber implant surgery

Mice were injected with buprenorphine (0.05- 0.1 mg/kg) prior to anesthesia and anesthetized with isoflurane (1-4%). Marcaine diluted 50% in saline was injected under the scalp to provide local anesthetic. The body temperature of the mouse was maintained for the duration of imaging with a heating pad. The depth of anesthesia was monitored by both the animal's response to toe-pinch every 5 min and observation of respiratory rate. Once the proper depth of anesthesia was reached, the animal was placed in a small animal stereotactic apparatus on top of a heating pad and Puralube vet ointment was applied to the eyes to prevent vision loss. All surgical procedures were performed in a sterile manner. Marcaine (0.5%) with saline 1:2 (0.25%) (2 mg/kg), was injected subcutaneously along the midline of the scalp as a local anesthetic. Before the incision, the hair over the scalp area was removed with NAIR and sterilized with a gentle scrub with Betadine on a sterile cotton swab, followed by 70% ethanol, repeated 3 times. The scalp was then removed with surgical scissors, membranes over the skull were removed by scraping, and the exposed bone was dried with compressed air. A 1 mm hole was then made over the dorsal

striatum with a high speed dental drill (Midwest Stylus 360). Any bleeding from the bone or dura was stopped with an application of collagen foam (Avitene Ultrafoam, Bard Davol). A glass pipette attached to a Nanoject II (Drummond Scientific) was filled with AAV9 Flex GCaMP6f virus (UPENN Viral Core) (300 nl of 10^{13} viral units/ml), and attached to the stereotax. A volume of 300ul of virus was injected into the dorsal striatum (1 mm AP, 1.0 mm ML, over several depths (DV: 3.0mm, 2.5 mm, 2,2mm) with 3 minutes of delay per depth. The glass pipette was then withdrawn from the brain and an imaging fiber was then implanted into the dorsal striatum at the location of the injection (1 mm AP, 1.0 mm ML, 2.5mm DV). The fiber was then secured to the skull with dental acrylic (Parkel Metabond). The mouse was then transferred to a heated cage to recover.

Time correlated single photon counting

To measure neural firing patterns in the two striatal pathways, mice were tethered the TCSPC machine (custom built from Becker Hickl parts). GCaMP6f was excited with a 473 nm picosecond pulsed laser (Becker Hickl). Mice were tested while freely moving and awake on the selected behavior task while GCaMP fluorescence was measured by the TCSPC in a population of neurons within 300 μm of the implant. Photon counts were recorded by TCSPC Image software from Becker Hickl.

Video and photon analysis.

High speed videos were analyzed and behaviors were scored by hand and annotated onto the recordings from the TCSPC machine. The following behaviors in the elevated plus maze were observed to be correlated to calcium transient peaks: initiation of forwards movement, initiation of backwards movement, initiating rearing, initiating sitting, nose poking, right turns, left turns, walking backwards, grooming, moving between the middle zone to the open or closed arms.

Photon analysis

Calcium transients were analyzed using custom functions written in MATLAB (**Figure 19**) by my collaborator Tim Cheung, as follows:

Calculation of dF/F. Raw photon counts were low-pass filtered using a Kaiser window (pass band 40 Hz, stop band 44 Hz) and then smoothed by binning the filtered data into 25 msec bins and calculating the median of each bin. The background fluorescence at time *t* in a session of the smoothed photon count, B(*t*), is then calculated by centering a sliding window (width 30 s) and determining the median of the photon count within that window. The dF/F at time *t* is calculated as [photon count at time *t* – B(t)] / B(*t*) (Howe & Dombeck 2016). For time points at the beginning and the end of the session where a centered sliding window is unavailable, the B(*t*) of the nearest time with a centered window is used to estimate the background fluorescence (e.g., for the beginning of the session *t* = 0-15 s, the B(*t*) of *t* = 15 s was used).

Identification dF/F transient blocks. Time bins during which dF/F are significantly elevated above baseline levels (i.e., transient blocks) are identified as follows.

The onset of a transient block. The onset of a transient block is identified by time-bins at which the 1st derivative of the dF/F (i.e., the slope) is higher than random chance, which is indicative of the rise of calcium transients (Gunaydin et al. 2014, Ramdya et al. 2006). The 1st derivative of the dF/F is calculated and then smoothed using a triangular window with half width of 4 bins (100 msec). The sample of 1st derivative is assumed to be normally distributed with potential outliers. The mean of this underlying normal distribution is estimated using the sample median of the 1st derivative dF/F (robust against outliers). The standard deviation (S.D.) is of this underlying normal distribution is estimated using the median absolute deviation (also robust against outliers; Gunaydin et al. 2014, Calipari et al. 2016). These estimates (mean, S.D.) are then used to calculate the p value of each data point of the 1st derivative dF/F (i.e., z-test). The Benjamini-Hochberg procedure is then used to correct for multiple comparisons (of multiple time-bins), with a False Discovery Rate set to 5% (0.05): this allows false positives to be controlled for regardless of session length (number of time bins). Finally, a time bin is only deemed significant if the next 3 time bins are also significant (after FDR correction), in order to reduce unreliable/false positive time bins.

The offset of a transient block. The criterion for the offset of a transient block is as follows. After the dF/F (not its 1st derivative) in a transient block has reached at least one peak (defined below), the first subsequent time-bin with a dF/F that either falls below the mean + 0.5×S.D. of the baseline dF/F

population up to that time bin (i.e., the population of time bins that are not classified as “transient”) (Lovett-Barron et al. 2014, *Science* 343:857-63), or falls below the dF/F level at the start of the “transient” block, is defined as the offset of a transient block.

Identification dF/F peaks. Visual inspection of dF/F traces suggests that within each transient block (i.e., a continuous block of time bins during which the dF/F is elevated above baseline levels), there can be multiple dF/F peaks. Gross measures of dF/F, such as the average dF/F during transients, obscure both the timing of these peaks and their amplitudes. dF/F peaks can be identified by time bins at which both the following occur: 1) the 1st derivative of dF/F crosses from positive to negative, 2) the 2nd derivative of dF/F is more negative than chance, which indicates that the downturn in dF/F is steeper than chance. This second criterion allows inflexion points of dF/F to be excluded. A custom algorithm was used to identify dF/F peaks within each transient block, described as follows. For each transient block, the highest dF/F within the block is automatically classified as a dF/F peak. Additional putative peaks within each transient block are identified by 1) first locating the time-bins at which the 1st derivative of dF/F crosses from positive to negative; 2) then examining the dF/F in a time-window of 100 msec before and 100 msec after, and locating the time-bin with the maximum dF/F within this time-window; 3) then looking up that time-bin’s corresponding 2nd derivative of dF/F, and accept the time-bin as a peak if the 2nd derivative of dF/F is significantly negative (calculated as described below). One consequence of this algorithm is that the minimal time between two consecutive peaks that can be identified is 125 msec. The 2nd derivative of dF/F is calculated from the 1st derivative of dF/F (see “Identification dF/F transient blocks section” above) and then smoothed using a rectangular window with a half width of 2 bins (50 msec). The sample of 2nd derivative is assumed to be normally distributed with potential outliers, analogous to the sample of 1st derivative, and its mean and S.D. were estimated using the sample median and the median absolute deviation, respectively (see “Identification dF/F transient blocks section” above). Time bins at which the 2nd derivative of dF/F is significantly negative is identified by calculating the p-value of each time bin, and then using the Benjamini-Hochberg procedure to set the False Discovery Rate to 5% (0.05). A time bin is only deemed significant if the next 3 time-bins are also significant (after FDR correction), in order to reduce unreliable/false positive time-bins.

Elevated plus maze

The maze was constructed of plastic plates glued together to form 4 arms (two open and two with walls). The maze was 30 cm long and 5 cm wide. The open arms of the maze did not have any railing. The maze was elevated 30 cm above the floor with plastic legs. In order to avoid detector overload due to overexposure of the detector to photons, the behaviors were performed under red light. A 30 fps camera (Med Associates) was positioned above the maze and a second camera 240 fps camera was positioned perpendicular to the maze. Both cameras were synchronized to start recording at the same time as the TCSPC machine. Mice were acclimated to the room for 1 hour prior to recording. Each mouse was taken out of its cage and tethered to the TCSPC machine before being placed in the maze facing the same open arm. Mice were allowed to explore the maze freely for 10 minutes before being returned to their cage.

RESULTS

We observed that mice spent significantly more time in the closed arms than in the open or middle areas of the maze (**Figure 20 top**). These results are in accordance with previous studies using the elevated maze (Walf and Frye 2013). We found that both direct path (GENSAT FK-150 Cre) and indirect path (A2A-Cre MMRRC 036158) mice showed a similar preference for the closed arms, demonstrating the effect was consistent across the different genotypes (**Figure 20 bottom**). Analysis of the rate of calcium transients showed that the SPNs of the dorsal striatum exhibited higher activity when the mouse was in the closed arms of the mouse than the middle and open arms (**Figure 21 top**). We then sought to determine if the rate of firing in the direct and indirect paths differed with the anxiety state of the mouse. We found that both dSPNs and iSPNs demonstrated significantly higher rates of firing in the closed than in the open arms (Two way ANOVA $P < .001$) (**Figure 21 bottom**).

We then examined if the increased firing rate was linked to increased motor behavior in the closed arms of the maze. The firing rates of dorsal striatal dSPNs and iSPNs, measured with calcium transients, has previously been correlated with motor patterns (Cui et al. 2013). Additionally, behaviors in the maze are associated with the anxiety state of the animal (Shepherd et al. 1994, Braun et al. 2011, Heredia et al. 2013). In light of these prior studies, we sought to determine if the behaviors were associated with

calcium transients. By examining the synchronized TCSPC peaks we found that the calcium peaks were associated with specific behavior patterns (**Figure 22**). We found that calcium peaks were correlated with one of the following behaviors: initiation of forwards movement, initiation of backwards movement, initiating rearing, initiating sitting, nose poking, right turns, left turns, walking backwards, grooming, moving between the middle zone to the open or closed arms. With the exception of grooming, we did not observe any of these behaviors to occur without creating calcium transients. Interestingly, grooming, which is classically considered to be associated with striatal circuitry (Lovinger 2017), was only rarely associated with calcium transients.

Finally, we sought to determine if these calcium transient associated behaviors were differentially expressed in the different zones of the maze. By examining behaviors that have been shown to be related to anxiety state, we found that both total behaviors (**Figure 23 top**), and behaviors adjusted for time spent in each arm (**Figure 23 bottom**), were significantly increased in the closed arms of the maze compared to the open and middle areas.

FIGURES

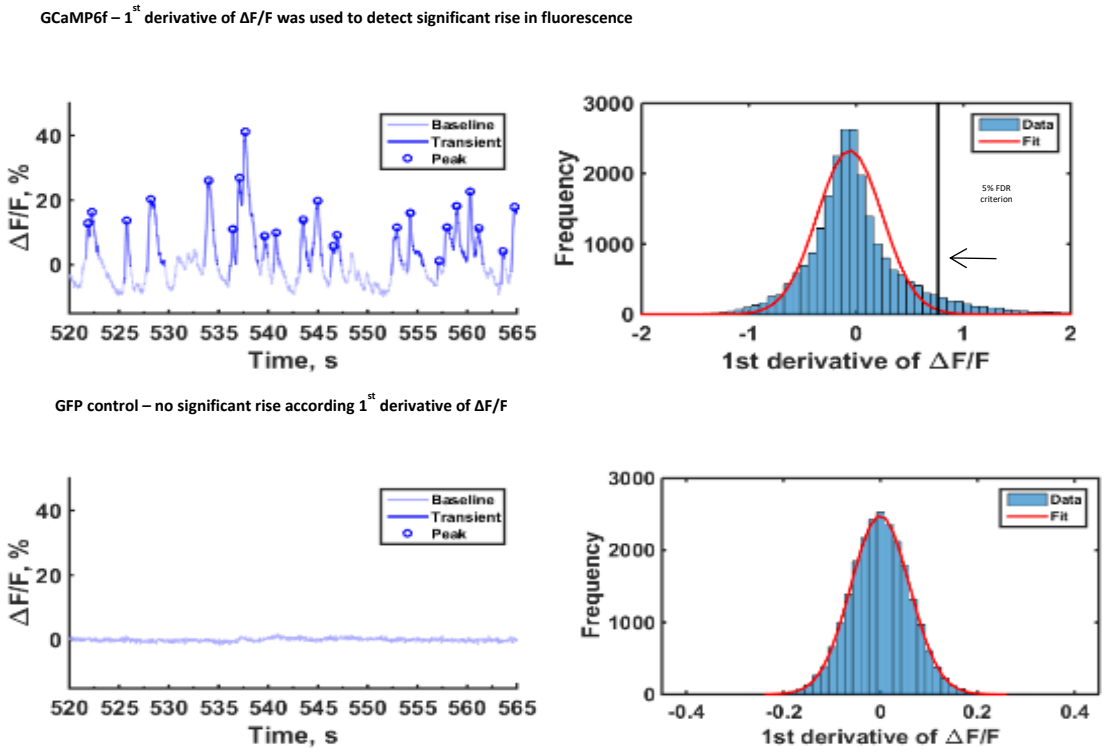

Figure 19. Tim's algorithm to detect Ca^{2+} peaks: Significantly high 1st derivative of ΔF/F detects rise of Ca^{2+} transient [4-5]. Multiple comparison corrected using False Discovery Rate (FDR) at 5%. Return to baseline defined as ΔF/F decaying to baseline's mean + 0.5 S.D [6]. Peak identified as bins at which 1st derivative of ΔF/F crosses zero and 2nd derivative of ΔF/F is significantly negative.

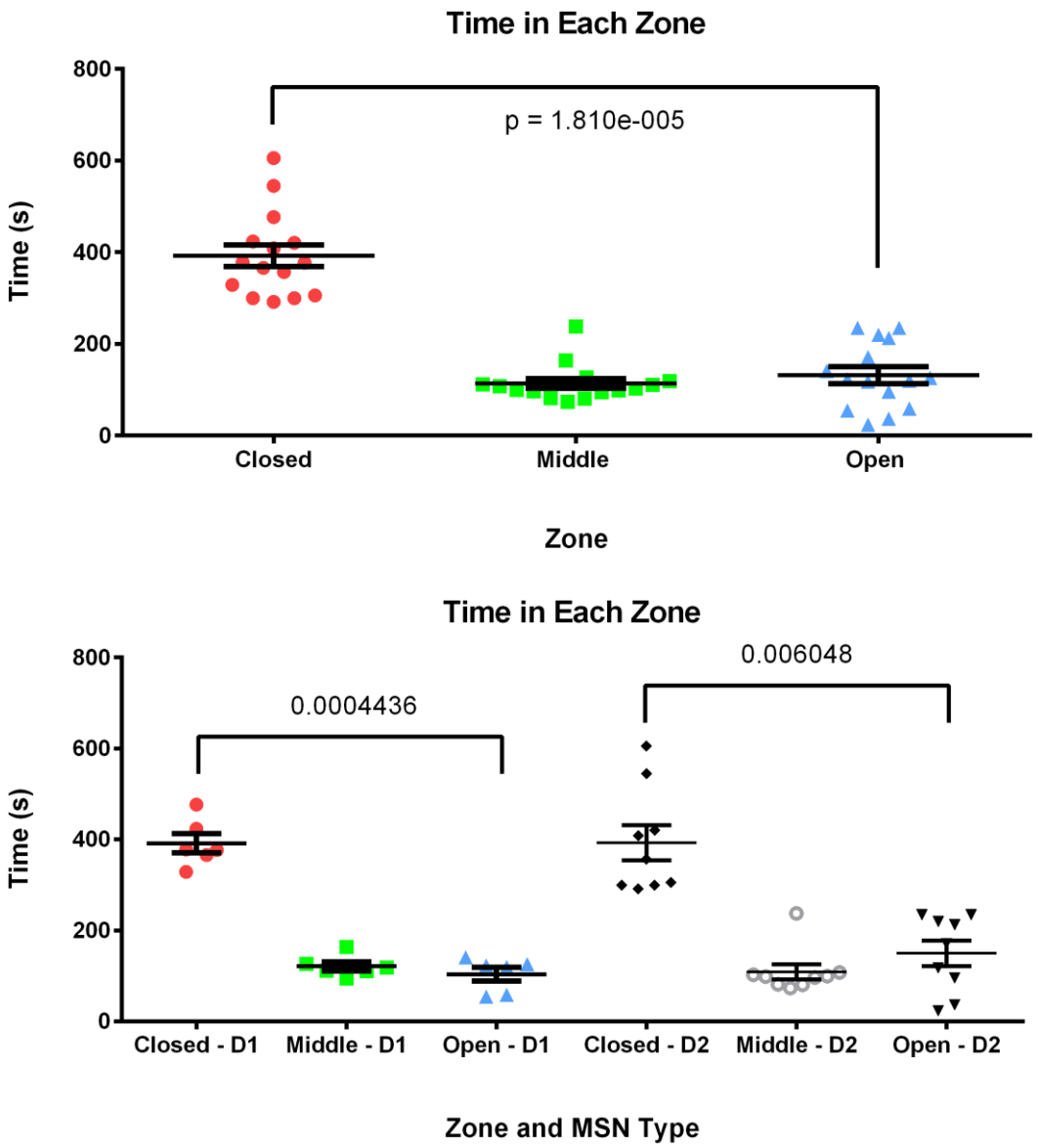

Figure 20. Time spent in each zone of the elevated plus maze. Top: the time spent in the closed arms of the maze for all groups combined was significantly greater than time spent in the middle zone and open arms of the maze. Bottom: considering the groups separately both Dd1 (direct path) and D2 (indirect path) mice spent significantly more time in the closed arms of the maze.

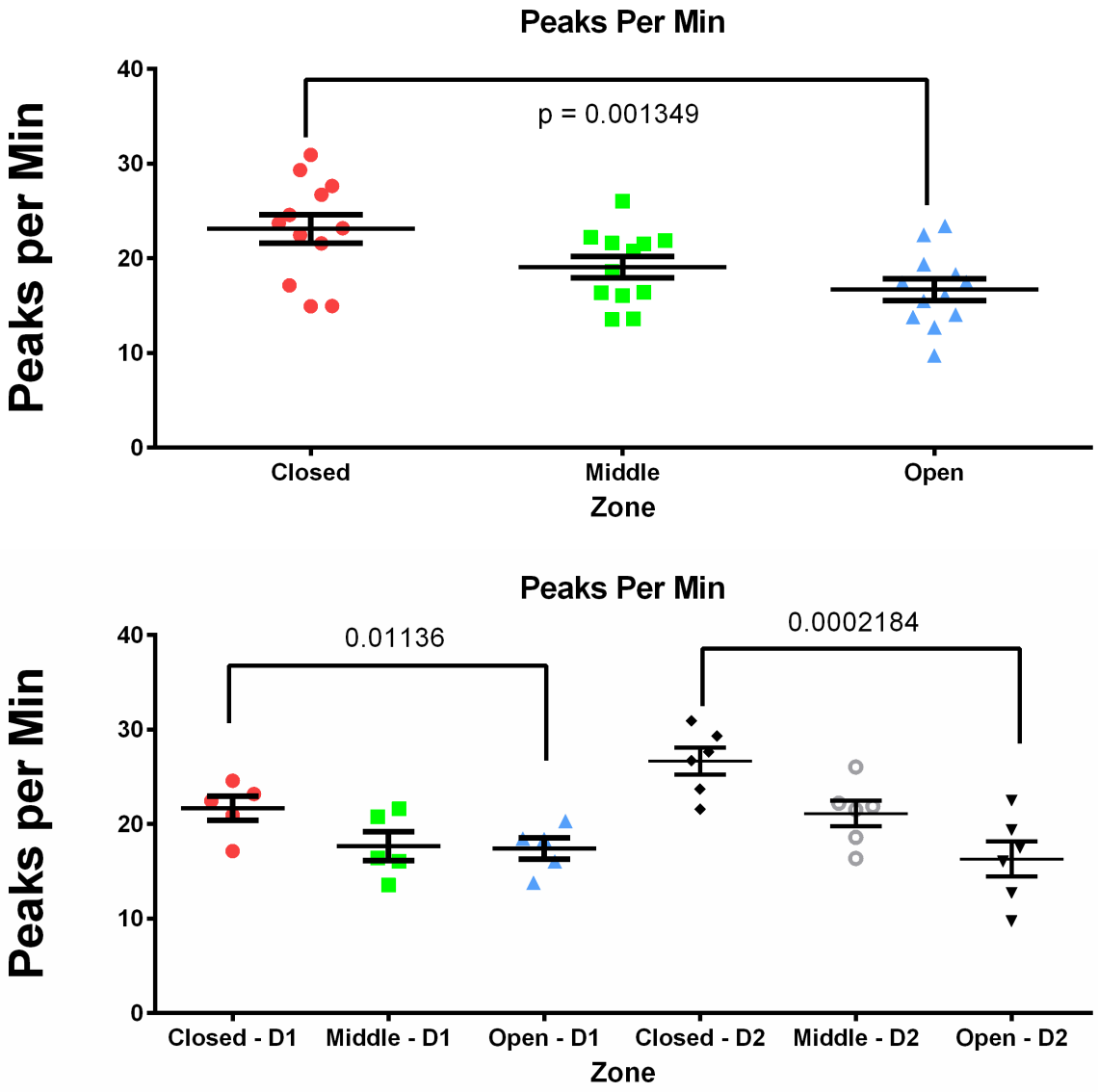

Figure 21. Rate of calcium peaks per minute in the different zones of the elevated plus maze. Top: calcium peaks per minute for both paths combined was significantly greater in the closed arms of the maze than the open and middle arms. Bottom: The rate of calcium peaks per minute were significantly greater in the closed arms of the maze than in the middle or open arms.

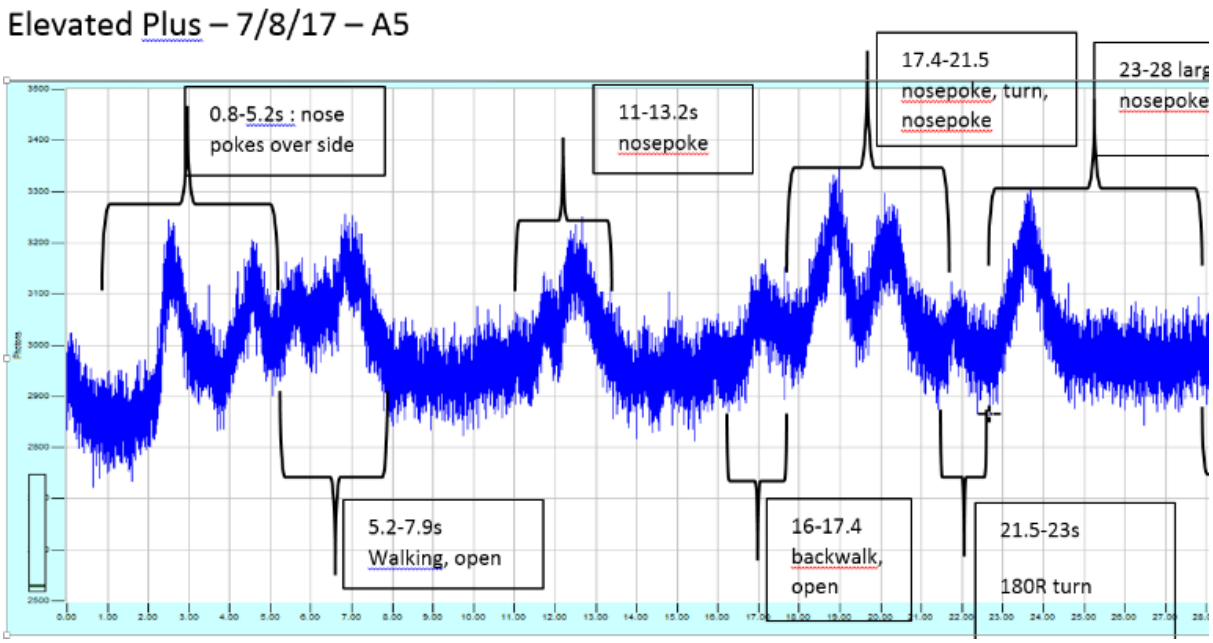

Figure 22. Annotation of different calcium peaks. This illustrates the method of evaluating each calcium peak and matching it with a corresponding behavior.

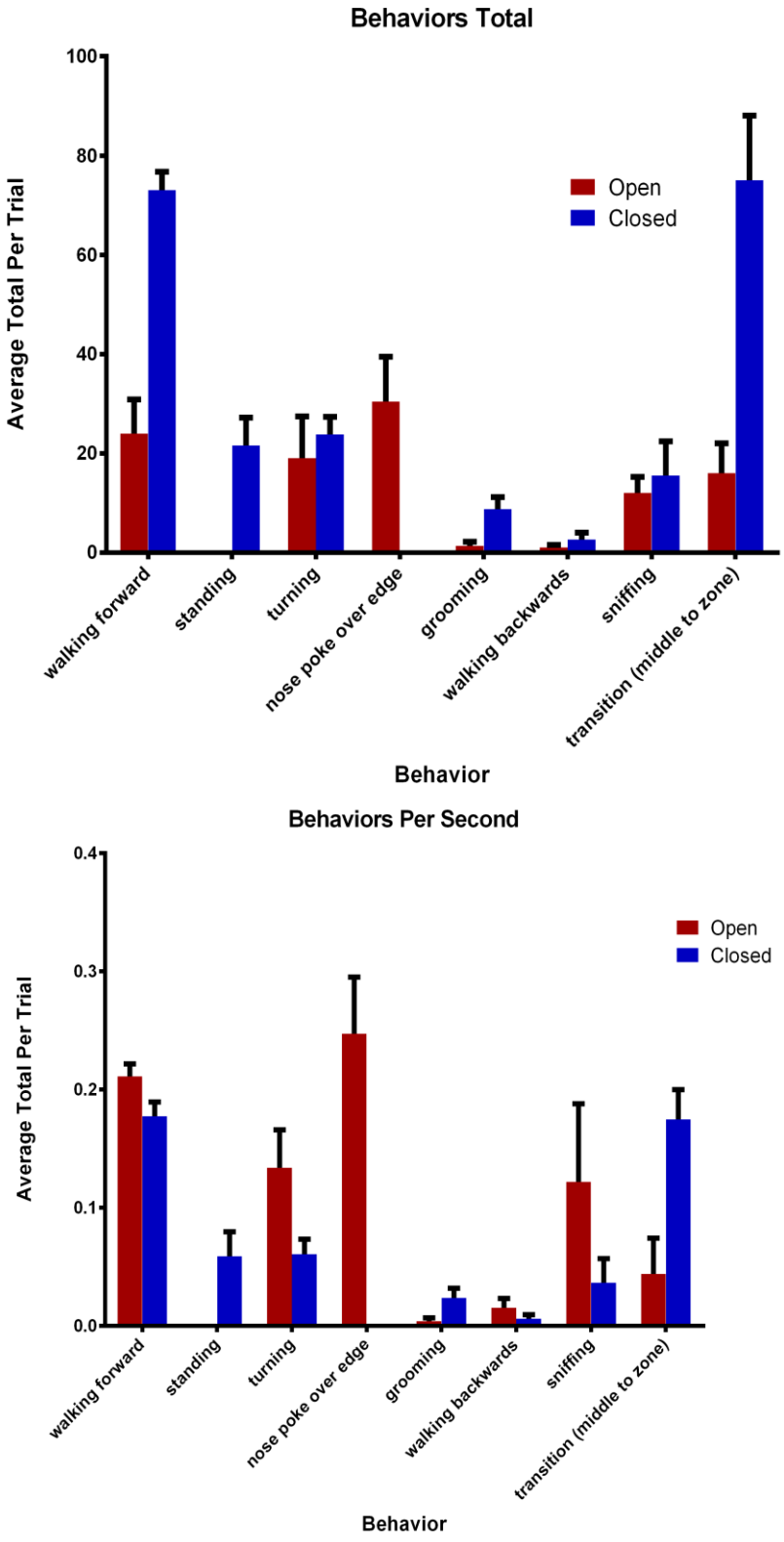

Figure 23. Behaviors displayed by mice in the elevated plus maze. Top the total average numbers of eight different behaviors displayed in the open arms compared to the closed arms averaged across all mice. Bottom: The same behaviors per second, adjusted for time spent in each zone.

DISCUSSION

This study is to our knowledge the first in vivo recording from the direct and indirect paths in the dorsal striatum in the mouse during a behavioral task of anxiety. Similar to previous publications (Walf and Frye 2013), we find that the mice prefer to spend time in the closed arms of the maze and that they exhibit more behaviors in those arms (**Figure 23**). We also find that both the direct and indirect paths exhibit increased activity while the mouse is in the closed arms (**Figure 21**). This increased firing is correlated with the higher levels of behaviors in the closed arms of the maze (**Figure 22**).

A possible conclusion is that the direct and indirect paths exhibit higher activity when the mouse is experiencing a lower anxiety state. As motor behaviors have been correlated with the anxiety state of the animal (Shepherd et al. 1994, Braun et al. 2011, Heredia et al. 2013), we surmise that the larger level motor behaviors in the closed arms correlates with the lower anxiety state. We believe this is the first in vivo confirmation for a potential role of the direct and indirect paths of differential modulation of motor patterns in different anxiety states. We are not able to determine from these results whether the DLS plays a role in the perception of anxiety in addition to the motor behavior associated with the anxious state.

An important limitation of the elevated plus maze is that open arm exploration can have several confounding variables. Increased entries into the open arms could, in addition to reduced anxiety, be due to increased novelty seeking or reduced impulse control. Therefore, additional tests of anxiety, such as active avoidance or novelty suppressed feeding, to further analyze the association with DLS activity and the anxious state (Njung'e 1991, Nicolas et al. 2006, Treit et al. 1981, Dulawa et al. 2004).

Future directions

We plan to repeat these experiments with a new cohort of mice that have been pretreated with benzodiazepines. Since benzodiazepines have been shown to be anxiolytic and increase the time spent in the open arms, we hypothesize that they will increase the exhibition of motor patterns in the open arms and that we will record a corresponding increase in the direct and indirect path firing rates. We are also in the process of determining whether the waveform of the calcium transient differs depending on the behavioral pattern. We further intend to examine the role of cannabinoid and DA modulation. Some studies have implicated DA signaling through the D3 receptor and cannabinoid signaling on CB1 receptors in the mesolimbic circuit to the ventral striatum and mPFC in the pathogenesis of anxiety (Leggio 2014, Wei 2017). Finally, in these mice we studied dSPNs and iSPNs in the DMS that comprise the associative path and we intend to follow up these results with recordings from the sensorimotor path via fibers implanted in the DLS and examine if the results are similar in the sensorimotor path.

We plan on analyzing the videos to determine if there is an association between the size and frequency of calcium transients and the type of behavior that the mouse is demonstrating. To do this, we will analyze the videos by hand and match different behaviors to different peaks. We will use logistical regression analysis to analyze whether there are specific types of peaks that are associated with specific behaviors.

CHAPTER 7: GENERAL DISCUSSION AND FUTURE DIRECTIONS

This chapter offers a general discussion on the research in the previous chapters and considers the future experimental directions.

In my first set of experiments, we utilized in-vivo multiphoton imaging of a NE specific fluorescent false neurotransmitter (FFN) AGH270 in mice surgically implanted with a cranial window to visualize noradrenergic release from each individual synapse. We either infused or microinjected FFN270 into barrel cortex of wt B6 mice, an area critical for processing sensory perception. We chose the barrel cortex as a model as the sensory cortex has been shown to be abnormal in children with ADHD (Francx et al., 2016), and because cortical noradrenergic synapses comprise an important therapeutic target of the ADHD treatments AMPH, methylphenidate, and atomoxetine. AMPH's action in the cortex in vivo had previously only been indirectly observed via SPECT or PET imaging and microdialysis.

We hypothesized that AMPH would cause vesicular release of NE and that the magnitude of its effect may differ between synapses. We found that in the absence of sensory stimuli, only a small subset of noradrenergic synapses actively released FFN, consistent with the phasic activity of the locus coeruleus. However, at 1mg/kg d-AMPH (i.p.), a mouse dosage equivalent to that used for treatment of ADHD, the FFN was emptied from all synapses within 10 minutes. This provides the first in vivo confirmation that AMPH can cause release of vesicular NE at treatment relevant doses. The effect was more rapid with 10 mg/kg, dosages associated with AMPH abuse. Surprisingly, AMPH's ability to cause complete release from all synapses was uniform and occurred in the absence of sensory stimulus to the cortex. This data supports the network reset theory of noradrenergic cortical function and is consistent with an action by which NE filters cortical neurons to tune out less salient stimuli.

We believe that our optical data provides convincing proof that AMPH causes complete NE release at the pharmacologically relevant dosage of 1mg/kg, as we are able to optically observe exocytosis,. We can also quantify the amount of release, in contrast to previous papers that were unable to determine the extent compared to reuptake at the lower dose range because they use slower bulk methods of measurement such as microdialysis. We believe this is both the first time that neurotransmission from individual presynaptic sites as well as its modulation by AMPH has been observed in mammalian brain in

vivo. This technique far exceeds the spatial and temporal resolution of either SPECT or PET imaging, and by providing a means to study of individual synapses, elucidates the synaptic mechanisms of noradrenergic drugs

Another interesting finding resulting from the experiments with FFN270 is the evidence for heterogenous release of neurotransmitters. We found that a small portion of release sites would not fully release the FFN, even after optogenetic stimulation. These findings seem to support a recent study that found evidence of silent synapses by using FFN200 in the striatum (Pereira et al. 2016). The FFN200 study used electrical stimulation of dopaminergic axons and found that most axons that display GCaMP3 transient would not release the FFN. However, little is known about the mechanism of plasma membrane accumulation or selectivity of FFN200. Follow-up experiments with other FFNs in different brain regions are necessary to confirm these findings and to determine whether they are indicative of the underlying biological mechanism of synaptic release, or an artifact of the FFN.

Limitations of FFNs

There are several limitations of FFNs. First, they cannot be used to distinguish between release of neurotransmitter that occurs during vesicular fusion, and release that occurs during other methods of neurotransmission such as the kiss-and-run form of neurotransmitter release. In this case, release from a vesicle occurs through brief opening of a fusion pore rather than full fusion (Ceccarelli et al. 1973, Henkel and Betz, 1995). One potential interpretation of a bouton does not rapidly destain is that it has switched its mode to of release from vesicular fusion to kiss-and-run. This switch in mode of transmission has been proposed occur during mGluR-dependent LTD (Stanislav et al., 2002).

Another limitation is in the interpretation of puncta that do not destain with stimulation. FFN imaging alone cannot be used to determine whether these puncta may have been damaged by the surgery and are thus not functioning normally. Using FFN270 in neurons that co-express GCaMP6f would help to resolve this issue, as the presence of a calcium transient can help determine if the neuron is undergoing calcium influx. If there is no calcium transient, then the puncta is likely not depolarizing and puncta that do not destain may be damaged or may not have been stimulated. Additionally, FFN270 may be accumulated into reserve pools of puncta that may not release with initial levels of stimulation. While we did not find

this to be the case with AMPH induced release, this may be an issue with other methods, such as channelrhodopsin or electrically simulated release.

Future directions

An interesting future direction would be to study AMPH release in different mouse models of disease. This would provide important translational information about the effects of the genes linked to the mouse disease models and could provide a link between gene function and alterations in cortical NE. Furthermore, the ability to simultaneously image FFN270 and GCaMP6f will provide information on the basis of such deficits in different mose models with different genetic defects. The FFNs will provide determination of any changes in the kinetics of release. An increase in the t1/2 of the release signal may implicate a defect in vesicular release of NE. If fewer synapses are observed with FFN270, there may be a problem with vesicular loading, perhaps involving NET. Fewer puncta overall may suggest that the NE projections are sparser in the disease model than in wild type mice. If there is a lower rate of calcium transients observed via GCaMP6f, one may conclude that there is a lower rate of firing. Another possibility is that there will not be any differences in either anatomy or firing rate of NE neurons, or kinetics of NE release. One may then conclude that any mechanisms involved in a NE deficit may include other factors, such as rapid breakdown of NE by catechol-o-methyl transferase (COMT).

A second future direction for FFN270 includes determining whether the probability or degree of release changes when mice undergo a task of learning. In this case, the speed and degree of destaining of puncta filled with FFN270 could be studied over several days. After a pre-training baseline has been established, the mice could be trained on a task involving learning. Changes in puncta destaining could be compared to the baseline.

Additional experiments may seek to explore deficits in working memory (WM). WM depends on optimal catecholamine levels in the mPFC (Seemans et al. 1998). Mouse models of psychiatric disease exhibit deficits in WM, deficits in cortico-subcortical circuits (Ellegood et al. 2014), and cortical catecholamine deficits (Murotani et al. 2007). Simultaneous multiphoton imaging of FFN release from cortical projections and the firing rate of those projections via GCaMP6f in the medial prefrontal cortex (mPFC) of mouse models of disease as they perform a delayed nonmatch to sample (DNMS) task of WM (Liu et al. 2014)

could provide important information on catecholamine deficits that occur during active cognitive processing in these models.

Imaging the natural transmission of NE in the absence of a NE releasing drug such as AMPH would have translational relevance and may unmask deficits that are not apparent with drug interventions. This would allow the determination of the kinetics of NE release in wild type and psychiatric disease model mice during a physiologically relevant task. If the mice have impaired performance on a task of WM and exhibit aberrant cortical catecholamine transmission during this task, this paradigm should provide some insight into the nature of such catecholamine deficiencies.

I expect that with this paradigm the researcher will be able to compare differences in catecholamine kinetics, number of active terminals, and the firing rate of the catecholamine projections between wild type and disease model mice during the DNMS task of WM. It is possible that both the mechanism and degree of catecholamine deficit may differ between the different mouse models of psychiatric disease.

It has been shown that during the learning of a new classical conditioning task, increased activity in VTA mesocortical neurons and catecholamine release in the mPFC initially correlates with the time of the reward (unconditioned stimulus) to the time of the cue (conditioned stimulus). It is possible that in wild type mice, FFN release will initially correlate with delivery of the reward, and as the mice learn the task, FFN release will shift to presentation of the second cue. In mouse models of psychiatric disease, however, this shift may not occur within the same time frame of the wild type mice. A second possibility is that these neurons will show deficits in NE release, the nature of which will be able to be determined with FFNs and GCaMP6f. An increased t1/2 of detaining may indicate deficits in vesicular release and lower rates of GCaMP6f transients may indicate lower firing rates of catecholaminergic neurons.

Another possibility is that the degree of impairment on the task of WM correlates with the degree of catecholamine deficit. The use of FFNs will allow the determination of a correlation between a catecholamine deficit and a WM deficit. Note, however, that WM depends on neuromodulators other than DA and NE levels in the mPFC, such as acetylcholine via muscarinic receptors in the mPFC. If the degree of deficit in WM does not correlate with deficits in catecholamine transmission, one may conclude that the

impairment on the task was due to other factors, such as the involvement of additional neuromodulatory systems or other circuit deficits that will not be tested in these experiments.

PHASOR

In my second set of experiments, I introduced a new method of cranial window surgery: PHASOR. This is an improvement in cranial window surgery that I initially developed to improve the use of FFNs *in vivo*. Cranial window surgery to prepare rodents for multiphoton imaging *in vivo* has become widespread in neuroscience. This surgery can be categorized into two main groups: surgeries in which a circle of bone is completely removed, and surgeries in which a circle of bone is thinned but not removed from the skull, i.e., “thin skull technique.” The removal or thinning of bone is necessary to prepare the mouse for optical imaging with a multiphoton microscope. Both of these surgeries make use of a high speed rotary drill to either thin or remove the bone from the skull. Because rotary drills will cut through both bone and soft tissue there is a high risk of damaging the dura and underlying blood vessels. The success of the surgery depends on the skill and hand eye coordination of the surgeon. Piezosugery was originally developed by Tomaso Vercellotti (Vercellotti et al. 2000) and has led to improvements in dental and cranio-maxilofacial, facial plastic surgery, ocular plastic surgery, and pediatric surgery in humans. We believe our data is the first application of piezosurgery to prepare mice for multiphoton imaging. Piezosurgery can be used to create both thin skull and complete bone removal windows. The use of a piezoelectric cutting device resulted in faster surgeries that were easier for new surgeons to perform, and had fewer complications that that from a high speed rotary drill. The advantages of speed and ease of use may be dependent on the surgeon because it is possible that given highly trained surgeons they will be able to create cranial windows with a dental drill with equal speed: however not everyone has the required excellent hand eye coordination and the results for new surgeons is apparent. We hope that the application of piezosurgery to mice will result in safer surgeries for mice and better surgical outcomes. In future experiments we hope to determine the effects of piezosurgery on neuronal inflammation. We will follow up with immunostains for neuronal markers of inflammation and microglia activation and compare these to traditional cranial

windows. We hypothesize that piezosurgery will result in lower levels of inflammatory markers, however this is an important control to perform.

TCSPC

In a separate set of experiments, we sought to analyze the firing rates of the dSPNs and iSPNs, of the direct and indirect paths respectively, during the elevated plus maze, a rodent task of anxiety. We found that the direct and indirect path SPNs exhibit higher rates of firing when the mouse was in a lower anxiety state. We also noted that in the closed arms of the maze, the mice exhibited higher levels of behaviors that are associated with a lower anxiety state. These behaviors were correlated with specific calcium transients. These results are important because the striatum is not typically a structure analyzed in the much studied anxiety loop, which includes the hippocampus, prefrontal cortex, and amygdala. There is nevertheless evidence from human MRI studies that the dorsal striatum plays a role in the processing of anxiety. Those studies found that increased intolerance of uncertainty correlate with increased striatal volume, and that patients with OCD possess increased striatal gray matter while patients with PTSD and panic disorder showed reduced in gray matter. Importantly, striatal volume correlated with markers of anxiety even in individuals who did not meet the criteria for an anxiety disorder suggesting that the striatum may play a role in the processing of anxiety (Hilbert 2015, Radua 2010, Kim 2017). Also relevant is evidence that deep brain stimulation of the striatum is an effective treatment for treatment refractory OCD (Denys et al. 2010, Gabriels et al. 2003, Greenberg et al. 2010). Our results, implicating a potential role of the striatum in anxiety are congruent with these studies. However, until pharmacological manipulation and more extensive anxiety tests are conducted, we are unable to determine the precise role of the striatum in anxiety. In follow-p experiments, we plan to repeat our recordings from the dSPN and iSPNs during other tasks of anxiety including the open field, the zero maze, and novelty suppressed feeding (Njung'e et al. 1991, Nicolas et al. 2006, Treit et al. 1981, Dulawa et al. 2004).

Another potential interpretation of these results are is that the striatum plays a role only in the motor output of anxiety, and not the perception or emotional state related to anxiety. In order to better understand its precise role, we also hope to test if drugs that are prescribed to humans to reduce anxiety, such as benzodiazepines and SSRIs, will have an effect on either the dSPN and iSPN firing rates, or the

behaviors the mouse exhibits in the maze. We recorded from the DMS because it receives input from the mPFC, which is implicated in the classic anxiety loop. Future experiments could include optogenetic silencing or stimulation of brain regions more typically implicated in anxiety, such as the amygdala, with simultaneous TCSPC recording from the striatum. It would be important to know if stimulation or inhibition of different parts of the classic anxiety loop would change the firing rate of the dSPNs and iSPNs in the dorsal striatum. If such changes could be observed, it would suggest that the classic loop features inputs into the striatum relevant to anxiety processing. Finally, it would be important to record from the DL, which receives input from motor and somatorsenory cortex, to determine if there are changes in this area as well.

Finally, in a preliminary set of experiments included as an appendix, we used viral vectors to express GCaMP6f in the dSPNs and iSPNs of the direct and indirect paths. By implanting optical fibers in the DMS and DLS, we were able to use TCSPC to record from the associative path and sensorimotor paths respectively. A portion of the mice had bilateral fibers implanted in both the left and right DLS. First, we examined the synchrony of peaks in the left and right striatum during goal directed tasks and found correlation of synchronous and asynchronous peaks during specific behaviors. We believe this is the first time that synchronous peaks between the left and right striatum have been observed. These results are intriguing and bring up unanswered questions. First, does the synchrony between peaks in the left and right striatum involve bridging collateral communication between hemispheres? Alternatively, are these seemingly synchronous but temporally phase shifted peaks produced independently? We would expect that a 6-hydroxydopamine hemi-lesion model of Parkinson's disease change the synchrony on one side, although this may also have effects on the nonlesioned side.

As this approach can record realtime changes in the dSPNs or iSPNs on both hemispheres, it would provide an optimal system to study levodopa induced dyskinesia. With this system, the effects of potential treatments such as cholinergic modulation on the firing rates of the direct and indirect paths could be visualized in real time.

In the next chapter of our motor skill learning experiments, we sought to measure the firing rate of the dSPNs and iSPNs changed during motor skill learning and determine if there was a difference in the

change of rate in the SPNs located in the DMS compared to the DLS. Unfortunately, multiple technical problems plagued this set of experiments and severely limited our present conclusions. We did, however, find that in the treadmill task of motor skill learning, dSPNs and iSPNs in the DLS show a significant decrease in firing. During the rotarod, parallel bars, and high bar, iSPNs indicate trends toward decreased firing, dSPNs in the DMS displayed a significant increase in firing between days 1 and 2 of motor skill learning. We also were able to verify that both the DMS and DLS are active during the days of motor learning.

While not yet complete, we think that these are important studies as the role of the DMS associative path and the DLS sensorimotor path during motor learning has been the subject of much controversy. The most recent and technically advanced study, Kupferschmidt et al. (2017), found that corticostriatal projections to the DMS shows low activation on the first day of learning that rapidly increases by the second day and then reduces again by the third day. In contrast, the corticostriatal projections to the DLS exhibited highest levels of activity on day one, and these levels decreased during each subsequent day of training. Our results are relevant, as by recording from the dSPNS and iSPNs of the direct and indirect pathways, we are measuring the next step in the cortico-striato-thalamo-cortico loop. Our results suggest that the changes in firing during motor learning are similar to those observed by Kupferschmidt et al. 2017, and the reduction in firing could be due to refinement of neuronal firing as would be expected by the results of Jin et al. 2014, and Klaus et al. 2017. Overall, this reduction would be in support of the neuronal ensemble hypothesis, that neuronal circuits become increasingly refined as learning occurs (Fingelkurts et al. 2004). Our results need to be followed with larger numbers of mice in order to reach significance. Follow-up experiments should also record from the mice for the entire 5 day period of motor learning. If our results are indeed significant, and the changes we observed are consistent over the full time period, the next step would be to determine if these changes in firing are due to changes in plasticity occurring on the synaptic level. Since a combination of DA, endocannabinoids, metabotropic glutamate, and cholinergic interneurons have been implicated in modulating corticostriatal plasticity (Wong et al. 2015, Bamford et al. 2009), we would seek to determine their role on the changes in dSPN and iSPN firing rates during motor skill learning. It is our hypothesis that cannabinoid receptor 1 antagonists such as AM-251, which interfere with the changes in corticostriatal plasticity, would also inhibit the mouse's ability

to learn the motor task. To further examine the role of DA on these tasks, they could be repeated with D1 and D2 antagonists.

REFERENCES

Adam, Y., Edwards, R. H., & Schuldiner, S. (2008). Expression and function of the rat vesicular monoamine transporter 2. *American Journal of Physiology-Cell Physiology, 294*(4), C1004-C1011.

Aizman, O., Brismar, H., Uhlén, P., Zettergren, E., Levey, A. I., Forssberg, H., . . . Aperia, A. (2000). Anatomical and physiological evidence for D 1 and D 2 dopamine receptor colocalization in neostriatal neurons. *Nature neuroscience, 3*(3).

Akkal, D., Dum, R. P., & Strick, P. L. (2007). Supplementary motor area and presupplementary motor area: targets of basal ganglia and cerebellar output. *Journal of Neuroscience, 27*(40), 10659-10673.

Albin, R. L., Young, A. B., & Penney, J. B. (1989). The functional anatomy of basal ganglia disorders. *Trends in Neurosciences, 12*(10), 366-375.

Aldrin-Kirk, P., Heuer, A., Rylander Ottosson, D., Davidsson, M., Mattsson, B., & Bjorklund, T. (2018). Chemogenetic modulation of cholinergic interneurons reveals their regulating role on the direct and indirect output pathways from the striatum. *Neurobiol Dis, 109*(Pt A), 148-162. doi:10.1016/j.nbd.2017.10.010

Allsop, S. A., Vander Weele, C. M., Wichmann, R., & Tye, K. M. (2014). Optogenetic insights on the relationship between anxiety-related behaviors and social deficits. *Frontiers in behavioral neuroscience, 8*.

Amara, S. G., & Sonders, M. S. (1998). Neurotransmitter transporters as molecular targets for addictive drugs. *Drug & Alcohol Dependence, 51*(1), 87-96.

Andlin-Sobocki, P., & Wittchen, H. U. (2005). Cost of anxiety disorders in Europe. *European Journal of Neurology, 12*(s1), 39-44.

Aosaki, T., Tsubokawa, H., Ishida, A., Watanabe, K., Graybiel, A. M., & Kimura, M. (1994). Responses of tonically active neurons in the primate's striatum undergo systematic changes during behavioral sensorimotor conditioning. *Journal of Neuroscience, 14*(6), 3969-3984.

Apicella, P. (2017). The role of the intrinsic cholinergic system of the striatum: What have we learned from TAN recordings in behaving animals? *Neuroscience, 360*, 81-94. doi:10.1016/j.neuroscience.2017.07.060

Ariano, M. A., & Kenny, S. L. (1989). Striatal muscarinic receptors are associated with substance P and somatostatin containing neurons. *Brain research, 497*(1), 51-58.

Aston-Jones, G., & Bloom, F. (1981). Activity of norepinephrine-containing locus coeruleus neurons in behaving rats anticipates fluctuations in the sleep-waking cycle. *Journal of Neuroscience, 1*(8), 876-886.

Aston-Jones, G., & Cohen, J. D. (2005). An integrative theory of locus coeruleus-norepinephrine function: adaptive gain and optimal performance. *Annu. Rev. Neurosci., 28*, 403-450.

Bamford, N. S., Zhang, H., Schmitz, Y., Wu, N.-P., Cepeda, C., Levine, M. S., . . . Sulzer, D. (2004). Heterosynaptic dopamine neurotransmission selects sets of corticostriatal terminals. *Neuron, 42*(4), 653-663.

Basheer, S., Govind, R., Daniel, A., Sam, G., Adarsh, V., & Rao, A. (2017). Comparative Study of

Piezoelectric and Rotary Osteotomy Technique for Third Molar Impaction. *The journal of contemporary dental practice, 18*(1), 60-64.

Bekar, L. K., Wei, H. S., & Nedergaard, M. (2012). The locus coeruleus-norepinephrine network optimizes coupling of cerebral blood volume with oxygen demand. *Journal of Cerebral Blood Flow & Metabolism, 32*(12), 2135-2145.

Bennett, B. D., Callaway, J. C., & Wilson, C. J. (2000). Intrinsic membrane properties underlying spontaneous tonic firing in neostriatal cholinergic interneurons. *Journal of Neuroscience, 20*(22), 8493-8503.

Bernard, V., Laribi, O., Levey, A. I., & Bloch, B. (1998). Subcellular redistribution of m2 muscarinic acetylcholine receptors in striatal interneurons in vivo after acute cholinergic stimulation. *Journal of Neuroscience, 18*(23), 10207-10218.

Bernard, V., Normand, E., & Bloch, B. (1992). Phenotypical characterization of the rat striatal neurons expressing muscarinic receptor genes. *Journal of Neuroscience, 12*(9), 3591-3600.

Berretta, S., Parthasarathy, H. B., & Graybiel, A. M. (1997). Local release of GABAergic inhibition in the motor cortex induces immediate-early gene expression in indirect pathway neurons of the striatum. *Journal of Neuroscience, 17*(12), 4752-4763.

Berridge, C. W., & Devilbiss, D. M. (2011). Psychostimulants as cognitive enhancers: the prefrontal cortex, catecholamines, and attention-deficit/hyperactivity disorder. *Biological psychiatry, 69*(12), e101-e111.

Berridge, C. W., & Stalnaker, T. A. (2002). Relationship between low-dose amphetamine-induced arousal and extracellular norepinephrine and dopamine levels within prefrontal cortex. *Synapse, 46*(3), 140-149.

Berridge, C. W., & Waterhouse, B. D. (2003). The locus coeruleus–noradrenergic system: modulation of behavioral state and state-dependent cognitive processes. *Brain Research Reviews, 42*(1), 33-84.

Bevan, M. D., Magill, P. J., Terman, D., Bolam, J. P., & Wilson, C. J. (2002). Move to the rhythm: oscillations in the subthalamic nucleus–external globus pallidus network. *Trends in Neurosciences, 25*(10), 525-531.

Bian, C., Zeng, Q., Xiong, H., Zhang, X., & Wang, S. (2010). Electrochemistry of norepinephrine on carbon-coated nickel magnetic nanoparticles modified electrode and analytical applications. *Bioelectrochemistry, 79*(1), 1-5.

Blackwell, K. T., Czubayko, U., & Plenz, D. (2003). Quantitative estimate of synaptic inputs to striatal neurons during up and down states in vitro. *Journal of Neuroscience, 23*(27), 9123-9132.

Blanc, G., Trovero, F., Vezina, P., Herve, D., Godeheu, A. M., Glowinski, J., & Tassin, J. P. (1994). Blockade of Prefronto-cortical α1-Adrenergic Receptors Prevents Locomotor Hyperactivity Induced by Subcortical D-Amphetamine Injection. *European Journal of Neuroscience, 6*(3), 293-298.

Bönisch, H., Runkel, F., Roubert, C., Giros, B., & Brüss, M. (1999). The human desipramine-sensitive noradrenaline transporter and the importance of defined amino acids for its function. *Autonomic and Autacoid Pharmacology, 19*(6), 327-333.

Braak, H., & Del Tredici, K. (2011). The pathological process underlying Alzheimer's disease in individuals under thirty. *Acta neuropathologica, 121*(2), 171-181.

Braun, A. A., Skelton, M. R., Vorhees, C. V., & Williams, M. T. (2011). Comparison of the elevated plus and elevated zero mazes in treated and untreated male Sprague–Dawley rats: effects of anxiolytic and anxiogenic agents. *Pharmacology Biochemistry and Behavior, 97*(3), 406-415.

Cachope, R., Mateo, Y., Mathur, B. N., Irving, J., Wang, H.-L., Morales, M., . . . Cheer, J. F. (2012). Selective activation of cholinergic interneurons enhances accumbal phasic dopamine release: setting the tone for reward processing. *Cell reports, 2*(1), 33-41.

Calhoon, G. G., & Tye, K. M. (2015). Resolving the neural circuits of anxiety. *Nature neuroscience, 18*(10), 1394.

Carlsson, A., Falck, B., Hillarp, N. Å., & Torp, A. (1962). Histochemical localization at the cellular level of hypothalamic noradrenaline. *Acta Physiologica, 54*(3-4), 385-386.

Carter, A. G., & Sabatini, B. L. (2004). State-dependent calcium signaling in dendritic spines of striatal medium spiny neurons. *Neuron, 44*(3), 483-493.

Chan, C. S., Surmeier, D. J., & Yung, W.-H. (2005). Striatal information signaling and integration in globus pallidus: timing matters. *Neurosignals, 14*(6), 281-289.

Chen, T.-W., Wardill, T. J., Sun, Y., Pulver, S. R., Renninger, S. L., Baohan, A., . . . Jayaraman, V. (2013). Ultrasensitive fluorescent proteins for imaging neuronal activity. *Nature, 499*(7458), 295.

Chesselet, M., & Graybiel, A. (1986). Striatal neurons expressing somatostatin-like immunoreactivity: evidence for a peptidergic interneuronal system in the cat. *Neuroscience, 17*(3), 547-571.

Clark, A. M., Leroy, F., Martyniuk, K. M., Feng, W., McManus, E., Bailey, M. R., . . . Kellendonk, C. (2017). Dopamine D2 Receptors in the Paraventricular Thalamus Attenuate Cocaine Locomotor Sensitization. *eNeuro, 4*(5), ENEURO. 0227-0217.2017.

Clayton, E. C., Rajkowski, J., Cohen, J. D., & Aston-Jones, G. (2004). Phasic activation of monkey locus ceruleus neurons by simple decisions in a forced-choice task. *Journal of Neuroscience, 24*(44), 9914-9920.

Constantinople, C. M., & Bruno, R. M. (2011). Effects and mechanisms of wakefulness on local cortical networks. *Neuron, 69*(6), 1061-1068.

Corbit, V. L., Ahmari, S. E., & Gittis, A. H. (2017). A Corticostriatal Balancing Act Supports Skill Learning. *Neuron, 96*(2), 253-255. doi:10.1016/j.neuron.2017.09.046

Cortes, M., Malave, L., Castello, J., Flajolet, M., Cenci, M. A., Friedman, E., & Rebholz, H. (2017). CK2 oppositely modulates L-DOPA induced dyskinesia via striatal projection neurons expressing D1- or D2-receptors. *J Neurosci*. doi:10.1523/jneurosci.0443-17.2017

Covey, D., Mateo, Y., Sulzer, D., Cheer, J. F., & Lovinger, D. M. (2017). Endocannabinoid modulation of dopamine neurotransmission. *Neuropharmacology*.

Cui, G., Jun, S. B., Jin, X., Pham, M. D., Vogel, S. S., Lovinger, D. M., & Costa, R. M. (2013). Concurrent activation of striatal direct and indirect pathways during action initiation. *Nature, 494*(7436), 238-242.

Cunha, M. P., Pazini, F. L., Lieberknecht, V., Budni, J., Oliveira, A., Rosa, J. M., . . . Rodrigues, A. L. S. (2017). MPP(+)-Lesioned Mice: an Experimental Model of Motor, Emotional, Memory/Learning, and Striatal Neurochemical Dysfunctions. *Mol Neurobiol, 54*(8), 6356-6377. doi:10.1007/s12035-016-0147-1

Daberkow, D., Brown, H., Bunner, K., Kraniotis, S., Doellman, M., Ragozzino, M., . . . Roitman, M. (2013). Amphetamine paradoxically augments exocytotic dopamine release and phasic dopamine signals. *Journal of Neuroscience, 33*(2), 452-463.

Danielson, M. L., Visser, S. N., Chronis-Tuscano, A., & DuPaul, G. J. (2017). A National Description of Treatment among United States Children and Adolescents with Attention-Deficit/Hyperactivity Disorder. *J Pediatr*. doi:10.1016/j.jpeds.2017.08.040

Deacon, R. M. (2013). Measuring motor coordination in mice. *Journal of visualized experiments: JoVE*(75).

Degenhardt, L., & Hall, W. (2012). Extent of illicit drug use and dependence, and their contribution to the global burden of disease. *The Lancet, 379*(9810), 55-70.

del Campo, N., Chamberlain, S. R., Sahakian, B. J., & Robbins, T. W. (2011). The roles of dopamine and noradrenaline in the pathophysiology and treatment of attention-deficit/hyperactivity disorder. *Biological psychiatry, 69*(12), e145-e157.

DeLong, M., & Wichmann, T. (2009). Update on models of basal ganglia function and dysfunction. *Parkinsonism & related disorders, 15*, S237-S240.

Dempsey, C., & Sawtell, N. B. (2016). The Timing Is Right for Cerebellar Learning. *Neuron, 92*(5), 931-933.

Denys, D., Mantione, M., Figee, M., van den Munckhof, P., Koerselman, F., Westenberg, H., . . . Schuurman, R. (2010). Deep brain stimulation of the nucleus accumbens for treatment-refractory obsessive-compulsive disorder. *Archives of general psychiatry, 67*(10), 1061-1068.

Devilbiss, D. M., & Waterhouse, B. D. (2004). The effects of tonic locus ceruleus output on sensory-evoked responses of ventral posterior medial thalamic and barrel field cortical neurons in the awake rat. *Journal of Neuroscience, 24*(48), 10773-10785.

Devinsky, O., Cross, J. H., Laux, L., Marsh, E., Miller, I., Nabbout, R., . . . Wright, S. (2017). Trial of cannabidiol for drug-resistant seizures in the Dravet syndrome. *New England Journal of Medicine, 376*(21), 2011-2020.

Dickson, D. W., Braak, H., Duda, J. E., Duyckaerts, C., Gasser, T., Halliday, G. M., . . . Wszolek, Z. K. (2009). Neuropathological assessment of Parkinson's disease: refining the diagnostic criteria. *The Lancet Neurology, 8*(12), 1150-1157.

Donoghue, J. P., & Herkenham, M. (1986). Neostriatal projections from individual cortical fields conform to histochemically distinct striatal compartments in the rat. *Brain research, 365*(2), 397-403.

Dorand, R. D., Barkauskas, D. S., Evans, T. A., Petrosiute, A., & Huang, A. Y. (2014). Comparison of intravital thinned skull and cranial window approaches to study CNS immunobiology in the mouse cortex. *Intravital, 3*(2), e29728.

Drew, P. J., Shih, A. Y., Driscoll, J. D., Knutsen, P. M., Blinder, P., Davalos, D., . . . Kleinfeld, D. (2010). Chronic optical access through a polished and reinforced thinned skull. *Nature methods, 7*(12), 981-984.

Dulawa, S. C., Holick, K. A., Gundersen, B., & Hen, R. (2004). Effects of chronic fluoxetine in animal models of anxiety and depression. *Neuropsychopharmacology, 29*(7), 1321-1330. doi:10.1038/sj.npp.1300433

Durieux, P. F., Bearzatto, B., Guiducci, S., Buch, T., Waisman, A., Zoli, M., . . . de Kerchove d'Exaerde, A. (2009). D2R striatopallidal neurons inhibit both locomotor and drug reward processes. *Nature neuroscience, 12*(4), 393-395.

Ellegood, J., Markx, S., Lerch, J., Steadman, P., Genç, C., Provenzano, F., . . . Gogos, J. (2014). Neuroanatomical phenotypes in a mouse model of the 22q11. 2 microdeletion. *Mol Psychiatry, 19*(1), 99.

Er, J. C., Leong, C., Teoh, C. L., Yuan, Q., Merchant, P., Dunn, M., . . . Kim, D. (2015). NeuO: a fluorescent chemical probe for live neuron labeling. *Angewandte Chemie International Edition, 54*(8), 2442-2446.

Exley, R., & Cragg, S. (2008). Presynaptic nicotinic receptors: a dynamic and diverse cholinergic filter of striatal dopamine neurotransmission. *British journal of pharmacology, 153*(S1).

Filloux, F. M. (2015). Cannabinoids for pediatric epilepsy? Up in smoke or real science? *Translational pediatrics, 4*(4), 271.

Fingelkurts, A. A., & Fingelkurts, A. A. (2004). Making complexity simpler: multivariability and metastability in the brain. *International Journal of Neuroscience, 114*(7), 843-862.

Fiorillo, C. D., Tobler, P. N., & Schultz, W. (2003). Discrete coding of reward probability and uncertainty by dopamine neurons. *Science, 299*(5614), 1898-1902.

Fitzgerald, M. L., Shobin, E., & Pickel, V. M. (2012). Cannabinoid modulation of the dopaminergic circuitry: implications for limbic and striatal output. *Progress in Neuro-Psychopharmacology and Biological Psychiatry, 38*(1), 21-29.

Florin, S. M., Kuczenski, R., & Segal, D. S. (1994). Regional extracellular norepinephrine responses to amphetamine and cocaine and effects of clonidine pretreatment. *Brain research, 654*(1), 53-62.

Foote, S. L., Bloom, F. E., & Aston-Jones, G. (1983). Nucleus locus ceruleus: new evidence of anatomical and physiological specificity. *Physiological reviews, 63*(3), 844-914.

Foster, D. J., Gentry, P. R., Lizardi-Ortiz, J. E., Bridges, T. M., Wood, M. R., Niswender, C. M., . . . Conn, P. J. (2014). M5 receptor activation produces opposing physiological outcomes in dopamine neurons depending on the receptor's location. *Journal of Neuroscience, 34*(9), 3253-3262.

Francx, W., Llera, A., Mennes, M., Zwiers, M. P., Faraone, S. V., Oosterlaan, J., . . . Beckmann, C. F. (2016). Integrated analysis of gray and white matter alterations in attention-deficit/hyperactivity disorder. *Neuroimage Clin, 11*, 357-367. doi:10.1016/j.nicl.2016.03.005

Freeze, B. S., Kravitz, A. V., Hammack, N., Berke, J. D., & Kreitzer, A. C. (2013). Control of basal ganglia output by direct and indirect pathway projection neurons. *Journal of Neuroscience, 33*(47), 18531-18539.

Freund, T., Powell, J., & Smith, A. (1984). Tyrosine hydroxylase-immunoreactive boutons in synaptic contact with identified striatonigral neurons, with particular reference to dendritic spines. *Neuroscience, 13*(4), 1189-1215.

Friedman, D., & Devinsky, O. (2015). Cannabinoids in the treatment of epilepsy. *New England Journal of Medicine, 373*(11), 1048-1058.

Fujiyama, F., Sohn, J., Nakano, T., Furuta, T., Nakamura, K. C., Matsuda, W., & Kaneko, T. (2011). Exclusive and common targets of neostriatofugal projections of rat striosome neurons: a single neuron-tracing study using a viral vector. *European Journal of Neuroscience, 33*(4), 668-677.

Gabriëls, L., Cosyns, P., Nuttin, B., Demeulemeester, H., & Gybels, J. (2003). Deep brain stimulation for treatment-refractory obsessive-compulsive disorder: psychopathological and neuropsychological outcome in three cases. *Acta Psychiatrica Scandinavica, 107*(4), 275-282.

Gerfen, C. R. (1984). The neostriatal mosaic: compartmentalization of corticostriatal input and striatonigral output systems. *Nature, 311*(5985), 461.

Gerfen, C. R., Engber, T. M., Mahan, L. C., Susel, Z., Chase, T. N., Monsma Jr, F. J., & Sibley, D. R. (1990). D1 and D2 dopamine receptor-regulated gene expression of striatonigral and striatopallidal neurons. *Science, 250*(4986), 1429-1432.

Gerfen, C. R., Herkenham, M., & Thibault, J. (1987). The neostriatal mosaic: II. Patch-and matrix-directed mesostriatal dopaminergic and non-dopaminergic systems. *Journal of Neuroscience, 7*(12), 3915-3934.

Gerfen, C. R., & Surmeier, D. J. (2011). Modulation of striatal projection systems by dopamine. *Annual review of neuroscience, 34*, 441-466.

Gerfen, C. R., & Young, W. S. (1988). Distribution of striatonigral and striatopallidal peptidergic neurons in both patch and matrix compartments: an in situ hybridization histochemistry and fluorescent retrograde tracing study. *Brain research, 460*(1), 161-167.

Gittis, A. H., & Kreitzer, A. C. (2012). Striatal microcircuitry and movement disorders. *Trends in Neurosciences, 35*(9), 557-564.

Gonzalez, M. Z., Puglia, M. H., Morris, J. P., & Connelly, J. J. (2017). Oxytocin Receptor Genotype and Low Economic Privilege Reverses Ventral Striatum-Social Anxiety Association. *Social Neuroscience*(just-accepted).

Graybiel, A., Ragsdale, C., Yoneoka, E., & Elde, R. (1981). An immunohistochemical study of enkephalins and other neuropeptides in the striatum of the cat with evidence that the opiate peptides are arranged to form mosaic patterns in register with the striosomal compartments visible by acetylcholinesterase staining. *Neuroscience, 6*(3), 377-397.

Graybiel, A. M., & Ragsdale, C. W. (1978). Histochemically distinct compartments in the striatum of human, monkeys, and cat demonstrated by acetylthiocholinesterase staining. *Proceedings of the National Academy of Sciences, 75*(11), 5723-5726.

Greenberg, B., Gabriels, L., Malone Jr, D., Rezai, A., Friehs, G., Okun, M., . . . Kubu, C. (2010). Deep brain stimulation of the ventral internal capsule/ventral striatum for obsessive-compulsive disorder: worldwide experience. *Mol Psychiatry, 15*(1), 64.

Gubernator, N. G., Zhang, H., Staal, R. G., Mosharov, E. V., Pereira, D. B., Yue, M., . . . Edwards, R. H. (2009). Fluorescent false neurotransmitters visualize dopamine release from individual presynaptic terminals. *Science, 324*(5933), 1441-1444.

Gunaydin, L. A., Grosenick, L., Finkelstein, J. C., Kauvar, I. V., Fenno, L. E., Adhikari, A., . . . Zalocusky, K. A. (2014). Natural neural projection dynamics underlying social behavior. *Cell, 157*(7), 1535-1551.

Gurevich, E. V., & Joyce, J. N. (2000). Dopamine D3 receptor is selectively and transiently expressed in the developing whisker barrel cortex of the rat. *Journal of Comparative Neurology, 420*(1), 35-51.

Halliday, G., Hely, M., Reid, W., & Morris, J. (2008). The progression of pathology in longitudinally followed patients with Parkinson's disease. *Acta neuropathologica, 115*(4), 409-415.

Hammond, C., Bergman, H., & Brown, P. (2007). Pathological synchronization in Parkinson's disease: networks, models and treatments. *Trends in Neurosciences, 30*(7), 357-364.

Hare, T. A., Schultz, W., Camerer, C. F., O'Doherty, J. P., & Rangel, A. (2011). Transformation of stimulus value signals into motor commands during simple choice. *Proceedings of the National Academy of Sciences, 108*(44), 18120-18125.

Heal, D. J., Smith, S. L., Gosden, J., & Nutt, D. J. (2013). Amphetamine, past and present–a pharmacological and clinical perspective. *Journal of Psychopharmacology, 27*(6), 479-496.

Heath, E., Chieng, B., Christie, M. J., & Balleine, B. W. (2017). Substance P and dopamine interact to modulate the distribution of delta-opioid receptors on cholinergic interneurons in the striatum. *Eur J Neurosci*. doi:10.1111/ejn.13750

Heinbockel, T., Brager, D. H., Reich, C. G., Zhao, J., Muralidharan, S., Alger, B. E., & Kao, J. P. (2005). Endocannabinoid signaling dynamics probed with optical tools. *Journal of Neuroscience, 25*(41), 9449-9459.

Herkenham, M., & Pert, C. B. (1981). Mosaic distribution of opiate receptors, parafascicular projections and acetylcholinesterase in rat striatum. *Nature, 291*(5814), 415-418.

Hernandez, L. F., Kubota, Y., Hu, D., Howe, M. W., Lemaire, N., & Graybiel, A. M. (2013). Selective effects of dopamine depletion and L-DOPA therapy on learning-related firing dynamics of striatal neurons. *Journal of Neuroscience, 33*(11), 4782-4795.

Herr, N. R., Park, J., McElligott, Z. A., Belle, A. M., Carelli, R. M., & Wightman, R. M. (2012). In vivo voltammetry monitoring of electrically evoked extracellular norepinephrine in subregions of the bed nucleus of the stria terminalis. *Journal of neurophysiology, 107*(6), 1731-1737.

Hersch, S. M., Gutekunst, C.-A., Rees, H., Heilman, C. J., & Levey, A. I. (1994). Distribution of m1-m4 muscarinic receptor proteins in the rat striatum: light and electron microscopic immunocytochemistry using subtype-specific antibodies. *Journal of Neuroscience, 14*(5), 3351-3363.

Hettie, K. S., Liu, X., Gillis, K. D., & Glass, T. E. (2013). Selective catecholamine recognition with NeuroSensor 521: a fluorescent sensor for the visualization of norepinephrine in fixed and live cells. *ACS chemical neuroscience, 4*(6), 918-923.

Hidaka, S., & Totterdell, S. (2001). Ultrastructural features of the nitric oxide synthase-containing interneurons in the nucleus accumbens and their relationship with tyrosine hydroxylase-containing terminals. *Journal of Comparative Neurology, 431*(2), 139-154.

Higuchi, H., Uchida, S., Murata, M., & Yoshida, H. (1985). Discrepancy between α1-adrenoceptor-mediated contraction and the occupation theory in rat vas deferens—Possible existence of a ‘silent’receptor. *European journal of pharmacology, 113*(1), 37-42.

Hilário, M. R., & Costa, R. M. (2008). High on habits. *Frontiers in neuroscience, 2*, 30.

Hilbert, K., Pine, D. S., Muehlhan, M., Lueken, U., Steudte-Schmiedgen, S., & Beesdo-Baum, K. (2015). Gray and white matter volume abnormalities in generalized anxiety disorder by categorical and dimensional characterization. *Psychiatry Research: Neuroimaging, 234*(3), 314-320.

Hires, S. A., Zhu, Y., & Tsien, R. Y. (2008). Optical measurement of synaptic glutamate spillover and reuptake by linker optimized glutamate-sensitive fluorescent reporters. *Proceedings of the National Academy of Sciences, 105*(11), 4411-4416.

Hjorth, J., Blackwell, K. T., & Kotaleski, J. H. (2009). Gap junctions between striatal fast-spiking interneurons regulate spiking activity and synchronization as a function of cortical activity. *J Neurosci, 29*(16), 5276-5286. doi:10.1523/jneurosci.6031-08.2009

Hoehn, M. M., & Yahr, M. D. (1998). Parkinsonism: onset, progression, and mortality. *Neurology, 50*(2), 318-318.

Hoffman, D. L., Dukes, E. M., & Wittchen, H. U. (2008). Human and economic burden of generalized anxiety disorder. *Depression and anxiety, 25*(1), 72-90.

Holtmaat, A., Bonhoeffer, T., Chow, D. K., Chuckowree, J., De Paola, V., Hofer, S. B., . . . Lee, W.-C. A. (2009). Long-term, high-resolution imaging in the mouse neocortex through a chronic cranial window. *Nature protocols, 4*(8), 1128-1144.

Hoover, B. R., & Marshall, J. F. (1999). Population characteristics of preproenkephalin mRNA-containing neurons in the globus pallidus of the rat. *Neuroscience letters, 265*(3), 199-202.

Howe, M., & Dombeck, D. (2016). Rapid signalling in distinct dopaminergic axons during locomotion and reward. *Nature, 535*(7613), 505.

Hu, G., Henke, A., Karpowicz Jr, R. J., Sonders, M. S., Farrimond, F., Edwards, R., . . . Sames, D. (2013). New fluorescent substrate enables quantitative and high-throughput examination of vesicular monoamine transporter 2 (VMAT2). *ACS chemical biology, 8*(9), 1947-1954.

Humphries, M. D., Wood, R., & Gurney, K. (2009). Dopamine-modulated dynamic cell assemblies generated by the GABAergic striatal microcircuit. *Neural Networks, 22*(8), 1174-1188.

Hutchison, W. D., Dostrovsky, J. O., Walters, J. R., Courtemanche, R., Boraud, T., Goldberg, J., & Brown, P. (2004). Neuronal oscillations in the basal ganglia and movement disorders: evidence from whole animal and human recordings. *Journal of Neuroscience, 24*(42), 9240-9243.

Iba, M., McBride, J. D., Guo, J. L., Zhang, B., Trojanowski, J. Q., & Lee, V. M.-Y. (2015). Tau pathology spread in PS19 tau transgenic mice following locus coeruleus (LC) injections of synthetic tau fibrils is determined by the LC's afferent and efferent connections. *Acta neuropathologica, 130*(3), 349-362.

Ilango, A., Kesner, A. J., Keller, K. L., Stuber, G. D., Bonci, A., & Ikemoto, S. (2014). Similar roles of substantia nigra and ventral tegmental dopamine neurons in reward and aversion. *Journal of Neuroscience, 34*(3), 817-822.

Izzo, P., & Bolam, J. P. (1988). Cholinergic synaptic input to different parts of spiny striatonigral neurons in the rat. *Journal of Comparative Neurology, 269*(2), 219-234.

Jáidar, O., Carrillo-Reid, L., Hernández, A., Drucker-Colín, R., Bargas, J., & Hernández-Cruz, A. (2010). Dynamics of the Parkinsonian striatal microcircuit: entrainment into a dominant network state. *Journal of Neuroscience, 30*(34), 11326-11336.

Jepma, M., Deinum, J., Asplund, C. L., Rombouts, S. A., Tamsma, J. T., Tjeerdema, N., . . . Nieuwenhuis, S. (2011). Neurocognitive function in dopamine-beta-hydroxylase deficiency. *Neuropsychopharmacology, 36*(8), 1608-1619. doi:10.1038/npp.2011.42

Jimenez-Castellanos, J., & Graybiel, A. (1987). Subdivisions of the dopamine-containing A8-A9-A10 complex identified by their differential mesostriatal innervation of striosomes and extrastriosomal matrix. *Neuroscience, 23*(1), 223-242.

Jin, X., & Costa, R. M. (2015). Shaping action sequences in basal ganglia circuits. *Curr Opin Neurobiol, 33*, 188-196. doi:10.1016/j.conb.2015.06.011

Jin, X., Tecuapetla, F., & Costa, R. M. (2014). Basal Ganglia Subcircuits Distinctively Encode the Parsing and Concatenation of Action Sequences. *Nature neuroscience, 17*(3), 423-430. doi:10.1038/nn.3632

Kempadoo, K. A., Mosharov, E. V., Choi, S. J., Sulzer, D., & Kandel, E. R. (2016). Dopamine release from the locus coeruleus to the dorsal hippocampus promotes spatial learning and memory. *Proceedings of the National Academy of Sciences, 113*(51), 14835-14840.

Kim, M. J., Shin, J., Taylor, J. M., Mattek, A. M., Chavez, S. J., & Whalen, P. J. (2017). Intolerance of uncertainty predicts increased striatal volume. *Emotion, 17*(6), 895.

Kincaid, A. E., & Wilson, C. J. (1996). Corticostriatal innervation of the patch and matrix in the rat neostriatum. *The Journal of comparative neurology, 374*(4), 578-592.

Kita, H., & Kitai, S. (1987). Efferent projections of the subthalamic nucleus in the rat: light and electron microscopic analysis with the PHA-L method. *Journal of Comparative Neurology, 260*(3), 435-452.

Klaus, A., Martins, G. J., Paixao, V. B., Zhou, P., Paninski, L., & Costa, R. M. (2017). The spatiotemporal organization of the striatum encodes action space. *Neuron, 95*(5), 1171-1180. e1177.

Koós, T., & Tepper, J. M. (2002). Dual cholinergic control of fast-spiking interneurons in the neostriatum. *Journal of Neuroscience, 22*(2), 529-535.

Kravitz, A. V., Freeze, B. S., Parker, P. R., Kay, K., Thwin, M. T., Deisseroth, K., & Kreitzer, A. C. (2010). Regulation of parkinsonian motor behaviours by optogenetic control of basal ganglia circuitry. *Nature, 466*(7306), 622-626.

Kravitz, A. V., & Kreitzer, A. C. (2011). Optogenetic manipulation of neural circuitry in vivo. *Current opinion in neurobiology, 21*(3), 433-439.

Kravitz, A. V., & Kreitzer, A. C. (2012). Striatal mechanisms underlying movement, reinforcement, and punishment. *Physiology, 27*(3), 167-177.

Kravitz, A. V., Owen, S. F., & Kreitzer, A. C. (2013). Optogenetic identification of striatal projection neuron subtypes during in vivo recordings. *Brain research, 1511*, 21-32.

Kravitz, A. V., Tye, L. D., & Kreitzer, A. C. (2012). Distinct roles for direct and indirect pathway striatal neurons in reinforcement. *Nature neuroscience, 15*(6), 816-818.

Kreitzer, A. C. (2009). Physiology and pharmacology of striatal neurons. *Annual review of neuroscience, 32*, 127-147.

Kreitzer, A. C., & Berke, J. D. (2011). Investigating striatal function through cell-type-specific manipulations. *Neuroscience, 198*, 19-26.

Kubota, Y., & Kawaguchi, Y. (1993). Spatial distributions of chemically identified intrinsic neurons in relation to patch and matrix compartments of rat neostriatum. *Journal of Comparative Neurology, 332*(4), 499-513.

Lach, G., Schellekens, H., Dinan, T. G., & Cryan, J. F. (2017). Anxiety, Depression, and the Microbiome: A Role for Gut Peptides. *Neurotherapeutics*, 1-24.

Lafourcade, M., Elezgarai, I., Mato, S., Bakiri, Y., Grandes, P., & Manzoni, O. J. (2007). Molecular components and functions of the endocannabinoid system in mouse prefrontal cortex. *PloS one, 2*(8), e709.

Lapper, S., & Bolam, J. (1992). Input from the frontal cortex and the parafascicular nucleus to cholinergic interneurons in the dorsal striatum of the rat. *Neuroscience, 51*(3), 533-545.

Lapper, S., Smith, Y., Sadikot, A., Parent, A., & Bolam, J. (1992). Cortical input to parvalbumin-immunoreactive neurones in the putamen of the squirrel monkey. *Brain research, 580*(1), 215-224.

Lee, M., Gubernator, N. G., Sulzer, D., & Sames, D. (2010). Development of pH-responsive fluorescent false neurotransmitters. *Journal of the American Chemical Society, 132*(26), 8828-8830.

Leggio, G. M., Torrisi, S. A., Castorina, A., Platania, C. B. M., Impellizzeri, A. A. R., Fidilio, A., . . . Salomone, S. (2015). Dopamine D3 receptor-dependent changes in alpha6 GABAA subunit expression in striatum modulate anxiety-like behaviour: Responsiveness and tolerance to diazepam. *European Neuropsychopharmacology, 25*(9), 1427-1436.

Lerner, T. N., & Kreitzer, A. C. (2011). Neuromodulatory control of striatal plasticity and behavior. *Current opinion in neurobiology, 21*(2), 322-327.

Leverenz, J. B., Quinn, J. F., Zabetian, C., Zhang, J., Montine, K. S., & Montine, T. J. (2009). Cognitive impairment and dementia in patients with Parkinson disease. *Current topics in medicinal chemistry, 9*(10), 903-912.

Lindvall, O., & Björklund, A. (1974). The glyoxylic acid fluorescence histochemical method: a detailed account of the methodology for the visualization of central catecholamine neurons. *Histochemistry, 39*(2), 97-127.

Lister, R. G. (1987). The use of a plus-maze to measure anxiety in the mouse. *Psychopharmacology, 92*(2), 180-185.

Liu, D., Gu, X., Zhu, J., Zhang, X., Han, Z., Yan, W., . . . Hou, R. (2014). Medial prefrontal activity during delay period contributes to learning of a working memory task. *Science, 346*(6208), 458-463.

Lovinger, D. M. (2017). An indirect route to repetitive actions. *J Clin Invest, 127*(5), 1618-1621. doi:10.1172/jci93918

Lu, L.-P., Wang, S.-Q., & Lin, X.-Q. (2004). Fabrication of layer-by-layer deposited multilayer films containing DNA and gold nanoparticle for norepinephrine biosensor. *Analytica chimica acta, 519*(2), 161-166.

Mallet, N., Le Moine, C., Charpier, S., & Gonon, F. (2005). Feedforward inhibition of projection neurons by fast-spiking GABA interneurons in the rat striatum in vivo. *Journal of Neuroscience, 25*(15), 3857-3869.

Marvin, J. S., Borghuis, B. G., Tian, L., Cichon, J., Harnett, M. T., Akerboom, J., . . . Bargmann, C. I. (2013). An optimized fluorescent probe for visualizing glutamate neurotransmission. *Nature methods, 10*(2), 162-170.

Matheus, F. C., Rial, D., Real, J. I., Lemos, C., Takahashi, R. N., Bertoglio, L. J., . . . Prediger, R. D. (2016). Temporal dissociation of striatum and prefrontal cortex uncouples anhedonia and defense behaviors relevant to depression in 6-OHDA-lesioned rats. *Molecular neurobiology, 53*(6), 3891-3899.

Matsushita, N., Okada, H., Yasoshima, Y., Takahashi, K., Kiuchi, K., & Kobayashi, K. (2002). Dynamics of tyrosine hydroxylase promoter activity during midbrain dopaminergic neuron development. *Journal of neurochemistry, 82*(2), 295-304.

Mehta, M. A., Sahakian, B. J., & Robbins, T. W. (2001). Comparative psychopharmacology of methylphenidate and related drugs in human volunteers, patients with ADHD, and experimental animals.

Melzer, S., Gil, M., Koser, D. E., Michael, M., Huang, K. W., & Monyer, H. (2017). Distinct corticostriatal GABAergic neurons modulate striatal output neurons and motor activity. *Cell reports, 19*(5), 1045-1055.

Mermelstein, P. G., Song, W.-J., Tkatch, T., Yan, Z., & Surmeier, D. J. (1998). Inwardly rectifying potassium (IRK) currents are correlated with IRK subunit expression in rat nucleus accumbens medium spiny neurons. *Journal of Neuroscience, 18*(17), 6650-6661.

Middleton, F. A., & Strick, P. L. (2000). Basal ganglia output and cognition: evidence from anatomical, behavioral, and clinical studies. *Brain and cognition, 42*(2), 183-200.

Mink, J. W. (2003). The basal ganglia and involuntary movements: impaired inhibition of competing motor patterns. *Archives of neurology, 60*(10), 1365-1368.

Miyachi, S., Lu, X., Imanishi, M., Sawada, K., Nambu, A., & Takada, M. (2006). Somatotopically arranged inputs from putamen and subthalamic nucleus to primary motor cortex. *Neurosci Res, 56*(3), 300-308.

Moret, C., & Briley, M. (2011). The importance of norepinephrine in depression. *Neuropsychiatric disease and treatment, 7*(Suppl 1), 9.

Moriwaki, A., Wang, J.-B., Svingos, A., van Bockstaele, E., Cheng, P., Pickel, V., & Uhl, G. R. (1996). μ Opiate receptor immunoreactivity in rat central nervous system. *Neurochemical research, 21*(11), 1315-1331.

Morón, J. A., Brockington, A., Wise, R. A., Rocha, B. A., & Hope, B. T. (2002). Dopamine uptake through the norepinephrine transporter in brain regions with low levels of the dopamine transporter: evidence from knock-out mouse lines. *Journal of Neuroscience, 22*(2), 389-395.

Motaghi, S., Sheibani, V., Farazifard, R., & Joneidi, H. (2006). Electrical stimulation of locus coeruleus strengthens the surround inhibition in layer V barrel cortex in rat. *Neuroscience letters, 401*(3), 280-284.

Muller, A., Joseph, V., Slesinger, P. A., & Kleinfeld, D. (2014). Cell-based reporters reveal in vivo dynamics of dopamine and norepinephrine release in murine cortex. *Nature methods, 11*(12), 1245-1252.

Murotani, T., Ishizuka, T., Hattori, S., Hashimoto, R., Matsuzaki, S., & Yamatodani, A. (2007). High dopamine turnover in the brains of Sandy mice. *Neuroscience letters, 421*(1), 47-51.

Nabavi, S., Fox, R., Proulx, C. D., Lin, J. Y., Tsien, R. Y., & Malinow, R. (2014). Engineering a memory with LTD and LTP. *Nature, 511*(7509), 348-352.

Nakano, K., Kayahara, T., Tsutsumi, T., & Ushiro, H. (2000). Neural circuits and functional organization of the striatum. *Journal of neurology, 247*, V1-V15.

Nambu, A. (2008). Seven problems on the basal ganglia. *Current opinion in neurobiology, 18*(6), 595-604.

Nambu, A., Tokuno, H., & Takada, M. (2002). Functional significance of the cortico-subthalamo-pallidal 'hyperdirect' pathway. *Neurosci Res, 43*(2), 111-117.

Namiki, S., Sakamoto, H., Iinuma, S., Iino, M., & Hirose, K. (2007). Optical glutamate sensor for spatiotemporal analysis of synaptic transmission. *European Journal of Neuroscience, 25*(8), 2249-2259.

Nguyen, Q.-T., Schroeder, L. F., Mank, M., Muller, A., Taylor, P., Griesbeck, O., & Kleinfeld, D. (2010). An in vivo biosensor for neurotransmitter release and in situ receptor activity. *Nature neuroscience, 13*(1), 127-132.

Nguyen, V., Tiemann, D., Park, E., & Salehi, A. (2017). Alpha-2 Agonists. *Anesthesiol Clin, 35*(2), 233-245. doi:10.1016/j.anclin.2017.01.009

Nicolas, L. B., & Prinssen, E. P. (2006). Social approach-avoidance behavior of a high-anxiety strain of rats: effects of benzodiazepine receptor ligands. *Psychopharmacology (Berl), 184*(1), 65-74. doi:10.1007/s00213-005-0233-y

Nisenbaum, E. S., Mermelstein, P. G., Wilson, C. J., & Surmeier, D. J. (1998). Selective blockade of a slowly inactivating potassium current in striatal neurons by (±) 6-chloro-APB hydrobromide (SKF82958). *Synapse, 29*(3), 213-224.

Nisenbaum, E. S., & Wilson, C. J. (1995). Potassium currents responsible for inward and outward rectification in rat neostriatal spiny projection neurons. *Journal of Neuroscience, 15*(6), 4449-4463.

Njung'e, K., & Handley, S. L. (1991). Evaluation of marble-burying behavior as a model of anxiety. *Pharmacol Biochem Behav, 38*(1), 63-67.

Obeso, J. A., Marin, C., Rodriguez-Oroz, C., Blesa, J., Benitez-Temiño, B., Mena-Segovia, J., . . . Olanow, C. W. (2008). The basal ganglia in Parkinson's disease: current concepts and unexplained observations. *Annals of neurology, 64*(S2).

Okubo, Y., Sekiya, H., Namiki, S., Sakamoto, H., Iinuma, S., Yamasaki, M., . . . Iino, M. (2010). Imaging extrasynaptic glutamate dynamics in the brain. *Proceedings of the National Academy of Sciences, 107*(14), 6526-6531.

Park, J., Takmakov, P., & Wightman, R. M. (2011). In vivo comparison of norepinephrine and dopamine release in rat brain by simultaneous measurements with fast-scan cyclic voltammetry. *Journal of neurochemistry, 119*(5), 932-944.

Parslow, A., Cardona, A., & Bryson-Richardson, R. J. (2014). Sample drift correction following 4D confocal time-lapse imaging. *Journal of visualized experiments: JoVE*(86).

Parthasarathy, H., & Graybiel, A. (1997). Cortically driven immediate-early gene expression reflects modular influence of sensorimotor cortex on identified striatal neurons in the squirrel monkey. *Journal of Neuroscience, 17*(7), 2477-2491.

Pavlíková, G., Foltán, R., Burian, M., Horká, E., Adámek, S., Hejčl, A., . . . Šedý, J. (2011). Piezosurgery prevents brain tissue damage: an experimental study on a new rat model. *International journal of oral and maxillofacial surgery, 40*(8), 840-844.

Pellow, S., Chopin, P., File, S. E., & Briley, M. (1985). Validation of open: closed arm entries in an elevated plus-maze as a measure of anxiety in the rat. *Journal of neuroscience methods, 14*(3), 149-167.

Pereira, D. B., Schmitz, Y., Mészáros, J., Merchant, P., Hu, G., Li, S., . . . Morgenstern, T. J. (2016). Fluorescent false neurotransmitter reveals functionally silent dopamine vesicle clusters in the striatum. *Nature neuroscience, 19*(4), 578-586.

Portmann, T., Yang, M., Mao, R., Panagiotakos, G., Ellegood, J., Dolen, G., . . . Dolmetsch, R. E. (2014). Behavioral abnormalities and circuit defects in the basal ganglia of a mouse model of 16p11.2 deletion syndrome. *Cell Rep, 7*(4), 1077-1092. doi:10.1016/j.celrep.2014.03.036

Prensa, L. a., & Parent, A. (2001). The nigrostriatal pathway in the rat: a single-axon study of the relationship between dorsal and ventral tier nigral neurons and the striosome/matrix striatal compartments. *Journal of Neuroscience, 21*(18), 7247-7260.

Radua, J., Van Den Heuvel, O. A., Surguladze, S., & Mataix-Cols, D. (2010). Meta-analytical comparison of voxel-based morphometry studies in obsessive-compulsive disorder vs other anxiety disorders. *Archives of general psychiatry, 67*(7), 701-711.

Raiteri, M., Bertollini, A., Angelini, F., & Levi, G. (1975). d-Amphetamine as a releaser or reuptake inhibitor of biogenic amines in synaptosomes. *European journal of pharmacology, 34*(1), 189-195.

Ramdya, P., Reiter, B., & Engert, F. (2006). Reverse correlation of rapid calcium signals in the zebrafish optic tectum in vivo. *Journal of neuroscience methods, 157*(2), 230-237.

Ramos, B. P., & Arnsten, A. F. (2007). Adrenergic pharmacology and cognition: focus on the prefrontal cortex. *Pharmacology & therapeutics, 113*(3), 523-536.

Ravenelle, R., Neugebauer, N. M., Niedzielak, T., & Donaldson, S. T. (2014). Sex differences in diazepam effects and parvalbumin-positive GABA neurons in trait anxiety Long Evans rats. *Behavioural brain research, 270*, 68-74.

Redgrave, P., Rodriguez, M., Smith, Y., Rodriguez-Oroz, M. C., Lehericy, S., Bergman, H., . . . Obeso, J. A. (2010). Goal-directed and habitual control in the basal ganglia: implications for Parkinson's disease. *Nat Rev Neurosci, 11*(11), 760-772. doi:10.1038/nrn2915

Reiner, A., Albin, R. L., Anderson, K. D., D'Amato, C. J., Penney, J. B., & Young, A. B. (1988). Differential loss of striatal projection neurons in Huntington disease. *Proceedings of the National Academy of Sciences, 85*(15), 5733-5737.

Rivera, A., Alberti, I., Martín, A. B., Narváez, J. A., De La Calle, A., & Moratalla, R. (2002). Molecular phenotype of rat striatal neurons expressing the dopamine D5 receptor subtype. *European Journal of Neuroscience, 16*(11), 2049-2058.

Robertson, S. D., Plummer, N. W., De Marchena, J., & Jensen, P. (2013). Developmental origins of central norepinephrine neuron diversity. *Nature neuroscience, 16*(8), 1016-1023.

Rock, C., Zurita, H., Wilson, C., & Apicella, A. J. (2016). An inhibitory corticostriatal pathway. *Elife, 5*, e15890.

Rodriguez, P. C., Pereira, D. B., Borgkvist, A., Wong, M. Y., Barnard, C., Sonders, M. S., . . . Sulzer, D. (2013). Fluorescent dopamine tracer resolves individual dopaminergic synapses and their activity in the brain. *Proceedings of the National Academy of Sciences, 110*(3), 870-875.

Rosenberg, E. C., Tsien, R. W., Whalley, B. J., & Devinsky, O. (2015). Cannabinoids and epilepsy. *Neurotherapeutics, 12*(4), 747-768.

Rothman, R. B., & Baumann, M. H. (2003). Monoamine transporters and psychostimulant drugs. *European journal of pharmacology, 479*(1), 23-40.

Rothman, R. B., Baumann, M. H., Dersch, C. M., Romero, D. V., Rice, K. C., Carroll, F. I., & Partilla, J. S. (2001). Amphetamine-type central nervous system stimulants release norepinephrine more potently than they release dopamine and serotonin. *Synapse, 39*(1), 32-41.

Rymar, V. V., Sasseville, R., Luk, K. C., & Sadikot, A. F. (2004). Neurogenesis and stereological morphometry of calretinin-immunoreactive GABAergic interneurons of the neostriatum. *Journal of Comparative Neurology, 469*(3), 325-339.

Salahpour, A., Ramsey, A. J., Medvedev, I. O., Kile, B., Sotnikova, T. D., Holmstrand, E., . . . Murphy, K. (2008). Increased amphetamine-induced hyperactivity and reward in mice overexpressing the dopamine transporter. *Proceedings of the National Academy of Sciences, 105*(11), 4405-4410.

Sames, D., Dunn, M., Karpowicz Jr, R. J., & Sulzer, D. (2013). Visualizing neurotransmitter secretion at individual synapses. In: ACS Publications.

Sanders, J., Happe, H., Bylund, D., & Murrin, L. (2005). Development of the norepinephrine transporter in the rat CNS. *Neuroscience, 130*(1), 107-117.

Sara, S. J. (2009). The locus coeruleus and noradrenergic modulation of cognition. *Nature Reviews Neuroscience, 10*(3), 211-223.

Sara, S. J. (2009). The locus coeruleus and noradrenergic modulation of cognition. *Nature Reviews Neuroscience, 10*(3), 211.

Sara, S. J., & Bouret, S. (2012). Orienting and reorienting: the locus coeruleus mediates cognition through arousal. *Neuron, 76*(1), 130-141.

Sawamoto, K., Nakao, N., Kobayashi, K., Matsushita, N., Takahashi, H., Kakishita, K., . . . Murakami, F. (2001). Visualization, direct isolation, and transplantation of midbrain dopaminergic neurons. *Proceedings of the National Academy of Sciences, 98*(11), 6423-6428.

Scheggia, D., Zamberletti, E., Realini, N., Mereu, M., Contarini, G., Ferretti, V., . . . Papaleo, F. (2017). Remote memories are enhanced by COMT activity through dysregulation of the endocannabinoid system in the prefrontal cortex. *Mol Psychiatry*. doi:10.1038/mp.2017.126

Schroeter, S., Apparsundaram, S., Wiley, R. G., Miner, L. H., Sesack, S. R., & Blakely, R. D. (2000). Immunolocalization of the cocaine-and antidepressant-sensitive l-norepinephrine transporter. *Journal of Comparative Neurology, 420*(2), 211-232.

Schultes, R. E. (1973). Man and marihuana. *Natural History, 82*(7), 59-&.

Seamans, J. K., Floresco, S. B., & Phillips, A. G. (1998). D1 receptor modulation of hippocampal–prefrontal cortical circuits integrating spatial memory with executive functions in the rat. *Journal of Neuroscience, 18*(4), 1613-1621.

Secor, K. E., & Glass, T. E. (2004). Selective amine recognition: development of a chemosensor for dopamine and norepinephrine. *Organic letters, 6*(21), 3727-3730.

Segal, D. S., & Kuczenski, R. (1992). In vivo microdialysis reveals a diminished amphetamine-induced DA response corresponding to behavioral sensitization produced by repeated amphetamine pretreatment. *Brain research, 571*(2), 330-337.

Shen, W., Hamilton, S. E., Nathanson, N. M., & Surmeier, D. J. (2005). Cholinergic suppression of KCNQ channel currents enhances excitability of striatal medium spiny neurons. *Journal of Neuroscience, 25*(32), 7449-7458.

Shen, W., Hernandez-Lopez, S., Tkatch, T., Held, J. E., & Surmeier, D. J. (2004). Kv1. 2-containing K+ channels regulate subthreshold excitability of striatal medium spiny neurons. *Journal of neurophysiology, 91*(3), 1337-1349.

Shepherd, J. K., Grewal, S. S., Fletcher, A., Bill, D. J., & Dourish, C. T. (1994). Behavioural and pharmacological characterisation of the elevated “zero-maze” as an animal model of anxiety. *Psychopharmacology, 116*(1), 56-64.

Smith, Y., & Villalba, R. (2008). Striatal and extrastriatal dopamine in the basal ganglia: an overview of its anatomical organization in normal and Parkinsonian brains. *Movement Disorders, 23*(S3).

Song, S. C., Beatty, J. A., & Wilson, C. J. (2016). The ionic mechanism of membrane potential oscillations and membrane resonance in striatal LTS interneurons. *J Neurophysiol, 116*(4), 1752-1764. doi:10.1152/jn.00511.2016

Spencer, R. C., Devilbiss, D. M., & Berridge, C. W. (2015). The cognition-enhancing effects of psychostimulants involve direct action in the prefrontal cortex. *Biological psychiatry, 77*(11), 940-950.

Stocchi, F., Vacca, L., Ruggieri, S., & Olanow, C. (2005). Infusion of levodopa methyl ester in patients with advanced PD: a clinical and pharmacokinetic study. *Arch Neurol, 62*, 905-910.

Straub, C., Saulnier, J. L., Bègue, A., Feng, D. D., Huang, K. W., & Sabatini, B. L. (2016). Principles of synaptic organization of GABAergic interneurons in the striatum. *Neuron, 92*(1), 84-92.

Stübinger, S., Stricker, A., & Berg, B.-I. (2015). Piezosurgery in implant dentistry. *Clinical, cosmetic and investigational dentistry, 7*, 115.

Sulzer, D. (2011). How addictive drugs disrupt presynaptic dopamine neurotransmission. *Neuron, 69*(4), 628-649.

Sulzer, D., Sonders, M. S., Poulsen, N. W., & Galli, A. (2005). Mechanisms of neurotransmitter release by amphetamines: a review. *Progress in neurobiology, 75*(6), 406-433.

Sulzer, D., & Surmeier, D. J. (2013). Neuronal vulnerability, pathogenesis, and Parkinson's disease. *Movement Disorders, 28*(6), 715-724.

Surmeier, D. J., Bargas, J., Hemmings, H. C., Nairn, A. C., & Greengard, P. (1995). Modulation of calcium currents by a D 1 dopaminergic protein kinase/phosphatase cascade in rat neostriatal neurons. *Neuron, 14*(2), 385-397.

Surmeier, D. J., Bargas, J., & Kitai, S. (1989). Two types of A-current differing in voltage-dependence are expressed by neurons of the rat neostriatum. *Neuroscience letters, 103*(3), 331-337.

Surmeier, D. J., Ding, J., Day, M., Wang, Z., & Shen, W. (2007). D1 and D2 dopamine-receptor modulation of striatal glutamatergic signaling in striatal medium spiny neurons. *Trends in Neurosciences, 30*(5), 228-235.

Tanimura, A., Pancani, T., Lim, S. A. O., Tubert, C., Melendez, A. E., Shen, W., & Surmeier, D. J. (2017). Striatal cholinergic interneurons and Parkinson's disease. *Eur J Neurosci*. doi:10.1111/ejn.13638

Taverna, S., Ilijic, E., & Surmeier, D. J. (2008). Recurrent collateral connections of striatal medium spiny neurons are disrupted in models of Parkinson's disease. *Journal of Neuroscience, 28*(21), 5504-5512.

Tepper, J. M., & Bolam, J. P. (2004). Functional diversity and specificity of neostriatal interneurons. *Current opinion in neurobiology, 14*(6), 685-692.

Tepper, J. M., Tecuapetla, F., Koos, T., & Ibanez-Sandoval, O. (2010). Heterogeneity and diversity of striatal GABAergic interneurons. *Front Neuroanat, 4*, 150. doi:10.3389/fnana.2010.00150

Thomas, T. M., Smith, Y., Levey, A. I., & Hersch, S. M. (2000). Cortical inputs to m2-immunoreactive striatal interneurons in rat and monkey. *Synapse, 37*(4), 252-261.

Torres, G. E., Gainetdinov, R. R., & Caron, M. G. (2003). Plasma membrane monoamine transporters: structure, regulation and function. *Nature Reviews Neuroscience, 4*(1), 13-25.

Treit, D., Pinel, J. P., & Fibiger, H. C. (1981). Conditioned defensive burying: a new paradigm for the study of anxiolytic agents. *Pharmacol Biochem Behav, 15*(4), 619-626.

Troncoso, E., Muller, D., Korodi, K., Steimer, T., Welker, E., & Kiss, J. Z. (2004). Recovery of evoked potentials, metabolic activity and behavior in a mouse model of somatosensory cortex lesion: role of the neural cell adhesion molecule (NCAM). *Cerebral Cortex, 14*(3), 332-341.

Uchimura, N., Cherubini, E., & North, R. (1989). Inward rectification in rat nucleus accumbens neurons. *Journal of neurophysiology, 62*(6), 1280-1286.

Uchimura, N., Higashi, H., & Nishi, S. (1989). Membrane properties and synaptic responses of the guinea pig nucleus accumbens neurons in vitro. *Journal of neurophysiology, 61*(4), 769-779.

Uddin, M. S., Al Mamun, A., Kabir, M. T., Nasrullah, M., Wahid, F., Begum, M. M., . . . Amran, M. S. (2017). Neurochemistry of Neurochemicals: Messengers of Brain Functions. *Journal of Intellectual Disability-Diagnosis and Treatment, 5*, 000-000.

Ungerstedt, U. (1971). Stereotaxic mapping of the monoamine pathways in the rat brain. *Acta Physiologica, 82*(S367), 1-48.

van Dijk, A., Klanker, M., van Oorschot, N., Post, R., Hamelink, R., Feenstra, M. G., & Denys, D. (2013). Deep brain stimulation affects conditioned and unconditioned anxiety in different brain areas. *Translational psychiatry, 3*(7), e289.

Vazey, E. M., & Aston-Jones, G. (2012). The emerging role of norepinephrine in cognitive dysfunctions of Parkinson's disease. *Frontiers in behavioral neuroscience, 6*.

Vazey, E. M., & Aston-Jones, G. (2013). New tricks for old dogmas: optogenetic and designer receptor insights for Parkinson's disease. *Brain research, 1511*, 153-163.

Ventura, R., Cabib, S., Alcaro, A., Orsini, C., & Puglisi-Allegra, S. (2003). Norepinephrine in the prefrontal cortex is critical for amphetamine-induced reward and mesoaccumbens dopamine release. *Journal of Neuroscience, 23*(5), 1879-1885.

Vercellotti, T. (2000). Piezoelectric surgery in implantology: a case report--a new piezoelectric ridge expansion technique. *International Journal of Periodontics & Restorative Dentistry, 20*(4).

Vercellotti, T., De Paoli, S., & Nevins, M. (2001). The piezoelectric bony window osteotomy and sinus membrane elevation: introduction of a new technique for simplification of the sinus augmentation procedure. *International Journal of Periodontics & Restorative Dentistry, 21*(6).

Vercellotti, T., & Podesta, A. (2007). Orthodontic microsurgery: a new surgically guided technique for dental movement. *International Journal of Periodontics & Restorative Dentistry, 27*(4).

Visser, S. N., Danielson, M. L., Bitsko, R. H., Holbrook, J. R., Kogan, M. D., Ghandour, R. M., . . . Blumberg, S. J. (2014). Trends in the parent-report of health care provider-diagnosed and medicated attention-deficit/hyperactivity disorder: United States, 2003–2011. *Journal of the American Academy of Child & Adolescent Psychiatry, 53*(1), 34-46. e32.

Wakayama, S., Kiyonaka, S., Arai, I., Kakegawa, W., Matsuda, S., Ibata, K., . . . Hamachi, I. (2017). Chemical labelling for visualizing native AMPA receptors in live neurons. *Nature Communications, 8*.

Walf, A. A., & Frye, C. A. (2007). The use of the elevated plus maze as an assay of anxiety-related behavior in rodents. *Nature protocols, 2*(2), 322-328. doi:10.1038/nprot.2007.44

Wang, J., Zhang, Y., Xu, T., Luo, Q., & Zhu, D. (2012). An innovative transparent cranial window based on skull optical clearing. *Laser Physics Letters, 9*(6), 469.

Wang, Z., Kai, L., Day, M., Ronesi, J., Yin, H. H., Ding, J., . . . Surmeier, D. J. (2006). Dopaminergic control of corticostriatal long-term synaptic depression in medium spiny neurons is mediated by cholinergic interneurons. *Neuron, 50*(3), 443-452.

Wei, D., Allsop, S., Tye, K., & Piomelli, D. (2017). Endocannabinoid Signaling in the Control of Social Behavior. *Trends in Neurosciences, 40*(7), 385-396. doi:https://doi.org/10.1016/j.tins.2017.04.005

Wichmann, T., Bergman, H., & DeLong, M. R. (2017). Basal ganglia, movement disorders and deep brain stimulation: advances made through non-human primate research. *Journal of Neural Transmission*, 1-12.

Wilson, C. J., & Goldberg, J. A. (2006). Origin of the slow afterhyperpolarization and slow rhythmic bursting in striatal cholinergic interneurons. *Journal of neurophysiology, 95*(1), 196-204.

Wilson, C. J., & Kawaguchi, Y. (1996). The origins of two-state spontaneous membrane potential fluctuations of neostriatal spiny neurons. *Journal of Neuroscience, 16*(7), 2397-2410.

Wong, M. Y., Borgkvist, A., Choi, S. J., Mosharov, E. V., Bamford, N. S., & Sulzer, D. (2015). Dopamine-dependent corticostriatal synaptic filtering regulates sensorimotor behavior. *Neuroscience, 290*, 594-607. doi:10.1016/j.neuroscience.2015.01.022

Wong, M. Y., Sulzer, D., & Bamford, N. S. (2011). Imaging presynaptic exocytosis in corticostriatal slices. *Neurodegeneration: Methods and Protocols*, 363-376.

Wu, Y., Pearl, S., Zigmond, M., & Michael, A. (2000). Inhibitory glutamatergic regulation of evoked dopamine release in striatum. *Neuroscience, 96*(1), 65-72.

Xu, M., Li, L., & Pittenger, C. (2016). Ablation of fast-spiking interneurons in the dorsal striatum, recapitulating abnormalities seen post-mortem in Tourette syndrome, produces anxiety and elevated grooming. *Neuroscience, 324*, 321-329.

Yan, Z., & Surmeier, D. J. (1996). Muscarinic (m2/m4) receptors reduce N-and P-type Ca2+ currents in rat neostriatal cholinergic interneurons through a fast, membrane-delimited, G-protein pathway. *Journal of Neuroscience, 16*(8), 2592-2604.

Yang, G., Pan, F., Parkhurst, C. N., Grutzendler, J., & Gan, W.-B. (2010). Thinned-skull cranial window technique for long-term imaging of the cortex in live mice. *Nature protocols, 5*(2), 201-208.

Yang, X., Zhang, Y., Zhao, K., Zhao, Y., Liu, Y., Gong, H., . . . Zhu, D. (2016). Skull optical clearing solution for enhancing ultrasonic and photoacoustic imaging. *IEEE transactions on medical imaging, 35*(8), 1903-1906.

Zakharenko, S. S., Zablow, L., & Siegelbaum, S. A. (2002). Altered presynaptic vesicle release and cycling during mGluR-dependent LTD. *Neuron, 35*(6), 1099-1110.

Zarow, C., Lyness, S. A., Mortimer, J. A., & Chui, H. C. (2003). Neuronal loss is greater in the locus coeruleus than nucleus basalis and substantia nigra in Alzheimer and Parkinson diseases. *Archives of neurology, 60*(3), 337-341.

Zhang, Y. F., & Cragg, S. J. (2017). Pauses in Striatal Cholinergic Interneurons: What is Revealed by Their Common Themes and Variations? *Front Syst Neurosci, 11*, 80. doi:10.3389/fnsys.2017.00080

Zhao, B., Zhu, J., Dai, D., Xing, J., He, J., Fu, Z., . . . Wang, W. (2016). Differential dopaminergic regulation of inwardly rectifying potassium channel mediated subthreshold dynamics in striatal medium spiny neurons. *Neuropharmacology, 107*, 396-410. doi:10.1016/j.neuropharm.2016.03.037

Zhou, J. (2004). Norepinephrine transporter inhibitors and their therapeutic potential. *Drugs of the Future, 29*(12), 1235.

APPENDIX

THE STRIATUM IN MOTOR SKILL LEARNING

Presented here are the early results of some preliminary studies examining the changes that occur in the direct and indirect paths during behavioral tasks involving motor learning.

ABSTRACT:

The ability to learn new and more complex motor skills increases the ability to find food, escape from predators, and the chance of survival. Motor skill learning comprises an acquisition period, where a motor skill is goal directed, and a mastery period where a motor skill has become automatic (Corbit 2017). Striatal spiny projection neurons (SPNs) regulate movement through two major circuits. The direct pathway SPNs project to the substantia nigra pars reticulata (SNr) and globus pallidus interna (GPi). The indirect pathway SPNs expressing D2 receptors (iSPNs) trigger a multisynaptic circuit, synapsing to the globus pallidus externa (GPe), which then projects to the SNr. These paths can be further subdivided by anatomical location and cortical input. The dorsomedial striatum (DMS) comprises the associative path, and the dorsolateral striatum (DLS) comprises the sensorimotor path. Both the DMS and DLS have been implicated in motor skill learning. To our knowledge, there are no studies examining the extent of synchronous activity between left and right striatum in either the direct or indirect paths in the DMS or DLS during locomotion or motor skill learning.

We used time correlated single photon counting (TCSPC) to record neuronal activity in the direct and indirect paths in both the left and right DMS and DLS. D1-Cre (direct path) and A2A-Cre (indirect path) mice were injected with AAV9 Flex GCaMP6f virus. Imaging fibers were implanted in both the right and left dorsal lateral striatum. We adapted a camera to record mouse movement. Mice were recorded with the high speed video camera framelocked to the sampling rate of the TCSPC machine. This enabled us to perform simultaneous recording from both the left and right DMS and DLS with millisecond precision, allowing us to correlate locomotor behavior with GCaMP6f changes in fluorescence.

We found evidence of synchronous and asynchronous activity as determined by both amplitude and frequency of firing in DLS during goal oriented behaviors in mice. We also found a significant decrease in

calcium transients in the direct and indirect path neurons during motor learning. This is to our knowledge the first *in vivo* optical recording data suggesting that there is a reduction in direct and indirect path neuronal activation during motor learning and supports a “neuronal ensemble” hypothesis (Klaus et al. 2017).

Introduction.

The ability to learn new and more complex motor skills increases the ability to find food, and escape from predators and increases the chance of survival. In addition to its role in executing already learned motor skills through motor pattern support and suppression, the striatum is thought to play an important role in the learning of new motor skills. In disorders of the striatum such as Parkinson’s and Huntington’s disease, the ability to learn new motor skills is compromised (Nambu 2008). While many brain regions, notably including the cerebellum, are implicated in motor learning (Dempsey and Sawtell 2016), this study focuses on the potential role the direct and indirect paths of the striatum in motor skill learning.

Motor skill learning has been described in two periods, as an acquisition period, where a motor skill is goal directed, and the mastery period, where a motor skill no longer requires conscious control and the actions becomes automatic (Corbit et al. 2017). The motor acquisition period can be conceptualized as learning to ride a bicycle. During this period, which may take many days, the subject must be cognizant of feedback from failed attempts and readjust their technique accordingly. However, once mastery is achieved, riding the bicycle becomes automatic. This skill is also long lasting, persisting even in the absence of further practice.

Striatal spiny projection neurons (SPNs) regulate movement through two major circuits. The direct pathway SPNs project to the substantia nigra pars reticulata (SNr) and globus pallidus interna (GPi). The indirect pathway SPNs expressing D2 receptors (iSPNs) trigger a multisynaptic circuit, synapsing to the globus pallidus externa (GPe), which then projects to the SNr. Activation of the direct and indirect paths correlates with enhanced locomotion in mice. These two paths can be further subdivided depending on cortical input and spatial location. The associative path comprises cortical input from the medial prefrontal cortex (mPFC) to the dorsal medial striatum. The sensorimotor path comprises cortical input from primary motor and somatosensory cortex to the dorsolateral striatum. In an older model, the

associative path was theorized to play an important role in motor skill acquisition, while the sensorimotor path controls execution of already mastered motor skills (Graybiel et al. 2008, Corbit et al. 2017). Prior research disrupting each path has found that disruptions in the associative path result in loss of the ability to acquire new motor skills, but do not impair already learned motor skills while disrupting the sensorimotor path results in disruptions of previously learned motor skills. In this case, previously mastered skills return to conscious control. (Yin et al. 2009, Redgrave et al. 2010). A refinement on this model suggested that the DLS and DMS compete for control during motor learning (Thorn et al. 2010).

This model was theorized without the techniques to record from only the corticostriatal neurons involved in each path, but such techniques have now been developed. In a recent study, Kupferschmidt et al. (2017) used time correlated single photon counting to record presynaptic calcium transients from either the associative path or the sensorimotor path in mice during training on the rotarod, a rodent task of motor skill learning. In support of the revised model, they found that both paths were simultaneously active during skill acquisition and execution of mastered skills. However, in contrast to the previous models, they found that both paths were most active during the skill acquisition and less active during execution of mastered skills. They were able to further subdivide the skill acquisition period into two categories: 1) The *naïve* period, is the first day the animal is introduced to the motor skill. 2) The *early* period which is the second day the animal practices the motor skill. The *late* period describes the period of automatic execution of already mastered skills (Kupferschmidt et al. 2017.

If we were to conceptualize these timepoints with the example of learning to ride a bike, the naive period would be the first day the person attempts to ride the bicycle, the early period would be the second day the person practices riding, and the late period would be when bicycle riding mastery has been achieved.

Interestingly, Kupferschmidt (2017) found that the associative path shows low activity during the naïve period, increases to its highest activity during the early period, and then drops to low activity during the late period. The sensorimotor path shows its highest activity immediately during the naïve period, and slowly decreases during the early period to the lowest activity in the late period.

To address whether these changes in path activation were due to presynaptic modulation of corticostriatal terminals, Kupferschmidt compared firing rates of the soma in mPFC and M1 to the firing rates of the

presynaptic terminals of the associative and sensorimotor paths. They found that the firing rate changes in the cortical soma lagged behind the changes observed in the presynaptic terminals, indicating that presynaptic changes occurred first.

While Kupferschmidt's findings are able to dissociate the associative and sensorimotor paths during motor learning, they do not address whether the direct and indirect paths in the DMS and DLS exhibit similar changes in firing. In order to answer this question, used time correlated single photon counting with a machine similar to that used by Kupferschmidt and colleagues. We transfected mice expressing cre recombinase in A2A-receptor-expressing neurons and D1-receptor expressing neurons with AAV9 Flex GCaMP6f virus into either the DMS or DLS, and implanted bilateral imaging fibers in the same site (**Figure 24**). Mice were recorded with a high speed video camera framelocked to the sampling rate of the time correlated single photon counting machine. This enabled us to acquire simultaneous recordings from the left and right DMS or DLS at millisecond precision, providing a means to correlate locomotor behavior with GCaMP6f changes in fluorescence. In mice implanted with bilateral fibers, we were also able to examine striatal synchrony during a variety of behavioral tasks.

MATERIALS AND METHODS

Experiment 1. Double fiber freely moving behavior in DLS

Mice

Adult 8 week old male D1-Cre (GENSAT FK-150) and A2A-Cre (MMRRC 036158) mice were housed in a reverse light cycle room. All behavioral experiments were performed in the dark cycle of the mouse. All procedures were conducted in accordance with Institutional Animal Care and Use Committee (IACUC) of the New York State Psychiatric Institute.

Viral injection and fiber Implant Surgery

Mice were injected with buprenorphine (0.05- 0.1 mg/kg) prior to anesthesia and anesthetized with isofluorane (1-4%). Marcaine diluted 50% in saline was injected under the scalp to provide local anesthetic. The body temperature of the mouse was maintained for the duration of imaging with a heating pad. The depth of anesthesia was monitored by both the animal's response to toe-pinch every 5 min and

observation of respiratory rate. Once the proper depth of anesthesia was reached, the animal was placed in a small animal stereotactic apparatus on top of a heating pad and Puralube vet ointment was applied to the eyes to prevent vision loss. All surgical procedures were performed in a sterile manner. Marcaine (0.5%) with saline 1:2 (0.25%) (2 mg/kg), was injected subcutaneously along the midline of the scalp as a local anesthetic. Before the incision, the hair over the scalp area was removed with NAIR and sterilized with a gentle scrub with Betadine on a sterile cotton swab, followed by 70% ethanol, repeated 3 times. The scalp was then removed with surgical scissors, membranes over the skull were removed by scraping, and the exposed bone was dried with compressed air. A 1 mm hole was then made over the dorsal striatum with a high speed dental drill (Midwest Stylus 360). Any bleeding from the bone or dura was stopped with an application of collagen foam (Avitene Ultrafoam, Bard Davol). A glass pipette attached to a Nanoject II (Drummond Scientific) was filled with AAV9 Flex GCaMP6f virus (UPENN Viral Core) (300 nl of 10^{13} viral units/ml), and attached to the stereotax. A volume of 300ul of virus was injected into the dorsal striatum (1 mm AP, 1.0 mm ML, over several depths (DV: 3.0mm, 2.5 mm, 2,2mm) with 3 minutes of delay per depth. The glass pipette was then withdrawn from the brain and an imaging fiber was then implanted into the dorsal striatum at the location of the injection (1 mm AP, 1.0 mm ML, 2.5mm DV (DLS) and 1 mm AP, 1.0 mm ML, 1.0mm DV (DMS)). The fiber was then secured to the skull with dental acrylic (Parkel Metabond). The mouse was then transferred to a heated cage to recover.

Time correlated single photon counting

To measure neural firing patterns in the two striatal pathways, mice were tethered the TCSPC machine (custom built from Becker Hickl parts). GCaMP6f was excited with a 473 nm picosecond pulsed laser (Becker Hickl). Mice were tested while freely moving and awake on the selected behavior task while GCaMP fluorescence was measured by the TCSPC in a population of neurons within 300 μm of the implant. Photon counts were recorded by TCSPC Image software from Becker Hickl.

Data analysis

High speed videos were analyzed and behaviors were scored by hand and annotated onto the recordings from the TCSPC machine. The following behaviors were observed to be correlated to calcium transient peaks: initiation of forwards movement, initiation of backwards movement, initiating rearing, initiating

sitting, nose poking, right turns, left turns, walking backwards, grooming, digging, body shaking, responding to air puff, swimming. Calcium transients were evaluated with a custom Matlab script.

Behavioral Tasks

Before all tasks mice were brought to the behavior room 1 hour before testing.

The home cage

Mice housed in a standard 75sq/in plastic cage with bedding were tethered to the TCSPC machine and the camera was set to record through the clear side of the cage. The light in the behavior room was set to red light only. Mice were allowed to move freely in their home cage for 10 minutes while being recorded.

The cylinder

Mice were placed in a 6inch diameter clear Plexiglas cylinder. The floor was covered in clean bedding prior to experiments. The mice were tethered to the TCSPC machine and the camera was set to record through the clear side of the cylinder. The light in the behavior room was set to red light only. Mice were allowed to move freely in the cylinder for 10 minutes while being recorded. The cylinder was washed and bedding was changed between mice.

The treadmill

The treadmill apparatus is a 1 m long 10 cm wide moving treadmill. The back legs of the mice are held in the hand and the mice are balanced so that only their front paws are on the treadmill (**Figure 25**). The mice are trained to walk forwards for a period of 8 days followed by a break from days 8 to 13 without training. On the thirteenth day, forward walking training continues, and reverse walking training starts. During each day of testing the mice perform 10 trials of walking forwards for 10 seconds followed by 10 seconds of rest. During reverse training the mice perform 5 trials of forward walking followed by 5 trials of reverse walking. During the behavior tasks the mice are tethered to the TCSPC machine and a camera is positioned in front of the treadmill to record the mice. The light in the behavior room was set to red light only.

The Rotarod

This behavior was performed as described in Deacon 2013. On the rotarod, the mice walk on the horizontal rotating axis as the rotations per minute increases. The rotarod was set with a start speed of 4rpm and a rate of acceleration of 20 rpm. The acceleration started 10 seconds after placing the mouse on the rotarod. The mouse was held by the tail and placed on the rotarod facing away from the direction of rotation. This enables the mouse to walk forwards to stay on the bar. Mice are tested on both the treadmill and rotarod (until they fall or stop walking and hold onto the bar for a complete rotation) for five consecutive days while tethered to the TCSPC machine. While running through these behavioral tasks, mice were recorded on slow motion video, synced with TCSPC, to allow correlations between the firing patterns and behavior to be studied. The light in the behavior room was set to red light only.

The parallel-bars

The parallel bars were constructed and behavior was performed as described in Deacon 2013. Two parallel plastic bars of 1m length and 4mm diameter were fixed 30mm apart to posts at each end and elevated 60cm above the floor. Mice were tethered to the TCSPC machine and an overhead camera was set to record. The light in the behavior room was set to red light only. Each mouse was placed in the center of the parallel bars. The experiment was concluded when the mouse would move to the end of the bars and climb onto a post.

The high-bar

The high-bar was constructed and behavior was performed as described in Deacon 2013. A plastic bar of 1m length and 3mm diameter was fixed between two posts and elevated 60cm above the floor. Mice were tethered to the TCSPC machine and an overhead camera was set to record. The light in the behavior room was set to red light only. Each mouse was placed in the center of the high-bar. The experiment was concluded when the mouse would move to the end of the bar and climb onto a post.

RESULTS

Experiment 1. Double fiber recordings of synchronous and asynchronous firing.

We found evidence of synchronous and asynchronous activation of the dSPNs and iSPNs in the DLS during several behaviors. We tested the mice on 4 different behavioral paradigms: the corridor test, home

cage, the cylinder, and swim tests. We found that synchrony of peaks during behaviors in the behavioral paradigms could be classified into four broad categories. Unilateral right peaks, unilateral left sided peaks, synchronous right and left peaks, and asynchronous left and right peaks (**Figure 26**). While we did not find behaviors that were purely associated with one specific type of peak, we found associations between the behaviors and types of peaks.

Unilateral right and left peaks were most associated with turns in the either the contralateral direction or the ipsilateral direction. Shaking of the body was most associated with bilateral synchronous peaks. Asynchronous peaks were most associated with the periods of rearing and

Experiment 2. Recording from dSPNs and iSPNs in DLS during the treadmill task of motor skill learning.

Our results show that SPN in the DLS show high levels of activation during motor learning on the treadmill. We found that this activation tapers off as the mice practice treadmill walking (**Figure 27**). Mice showed a significant decrease in firing rate when performing the forward walk from day 6 to day 7 in both pathways. After training for a 7 days of reverse walking training, the mice became proficient at reverse walking, and a significant decrease in firing rate was observed (two-way ANOVA $P<.05$). Interestingly, while both the direct and indirect path show similar levels of reduction in firing, the indirect path starts at a lower baseline. In the indirect pathway at the start of reverse walking, the neurons did not fire as frequently as they did in the direct pathway (**Figure 27)**. The low firing rate suggests that perhaps learning to walk forwards also helped the mice with learning to walk backwards.

Experiment 3. Recording from iSPNs in the DLS and dSPNs in the DMS during the rotarod task of motor skill learning.

We found that on the first day of training, activation of dSPNs and iSPNs in the DMS was relatively low. The level of activation in the direct and indirect path was significantly higher on day two than on day 1 ($P<0.05$, two tailed t test) (**Figure 28**). In the DLS, rotarod activity was highest on day 1 and showed a trend to decrease on the second day of training. However, our results did not reach significance (**Figure 28**). Technical difficulties prevented us from recording from the dSPNs in the DLS and iSPNs in the DMS.

Experiment 4. Recording from iSPNs in the DLS during the parallel and high-bar bar tasks of motor learning.

Similar to our findings in the rotarod, in the DLS, we found dSPN and iSPN activity was at a maximum on the first day and reduced by the second day of training. However this trend did not reach significance (**Figure 29**).

Experiment 5. Recording from iSPNs in the DLS during the high-bar bar task of motor learning.

In the DLS, we found dSPN and iSPN activity was at a maximum on the first day and reduced by the second day of training. However this trend did not reach significance (**Figure 30**).

Figures

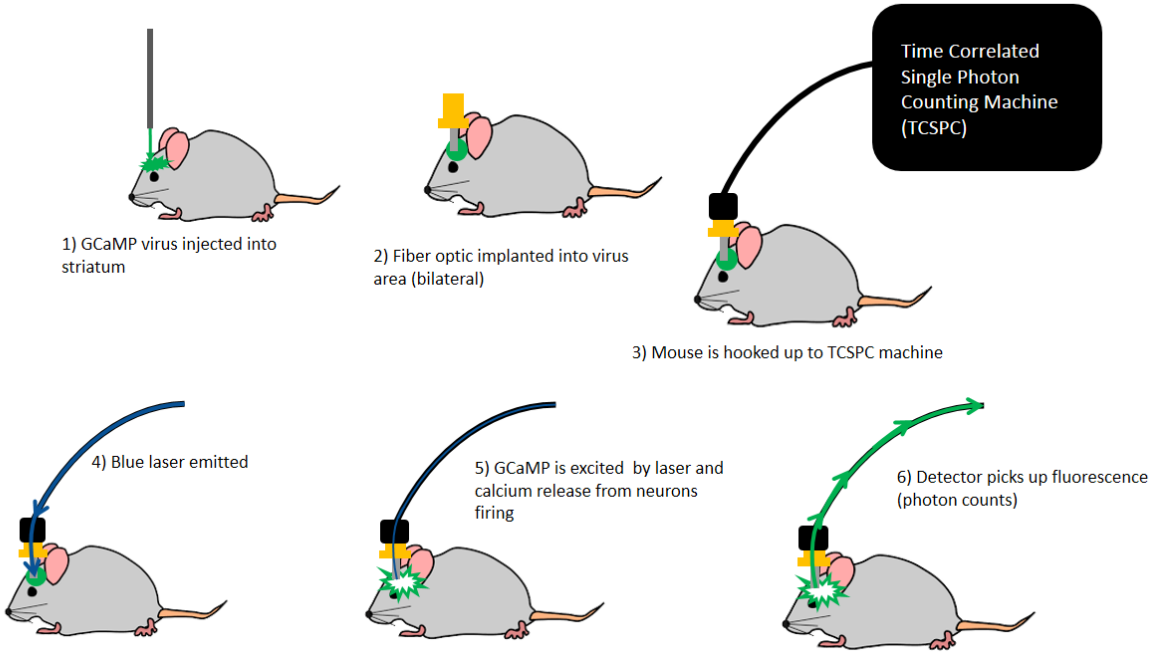

Figure 24. Diagram of experimental technique. 1) AAV90.FLEX.GCaMP6f virus is injected into the striatum. 2)A fiber optic is implanted into the same area during the same surgery. 3) The mouse is tethered to the TCSPC machine. 4) Blue laser light is pulsed into the brain with picosecond frequency. 5) GCaMP6f is excited by the laser and attains a high green fluorescence confirmation when it binds calcium in active neurons. 6) Green fluorescence emitted by GCaMP6f travels through the fiber and is captured by the detector.

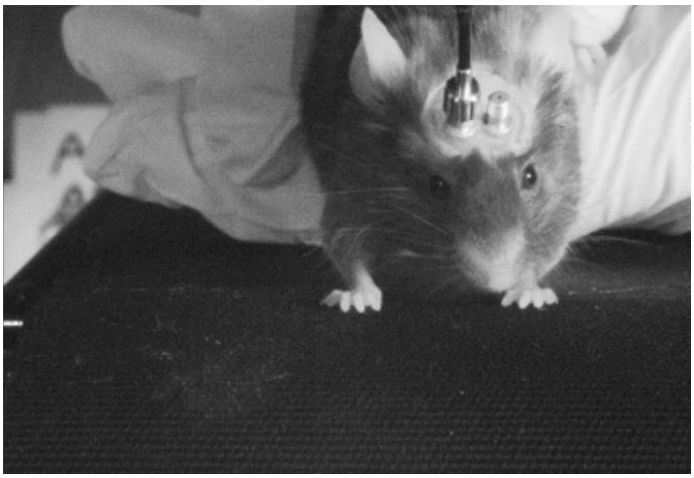

Figure 25. Mouse on the treadmill. The mouse is held in the hand with the back legs supported by the investigator. The front paws rest on the treadmill allowing forwards and backwards walking.

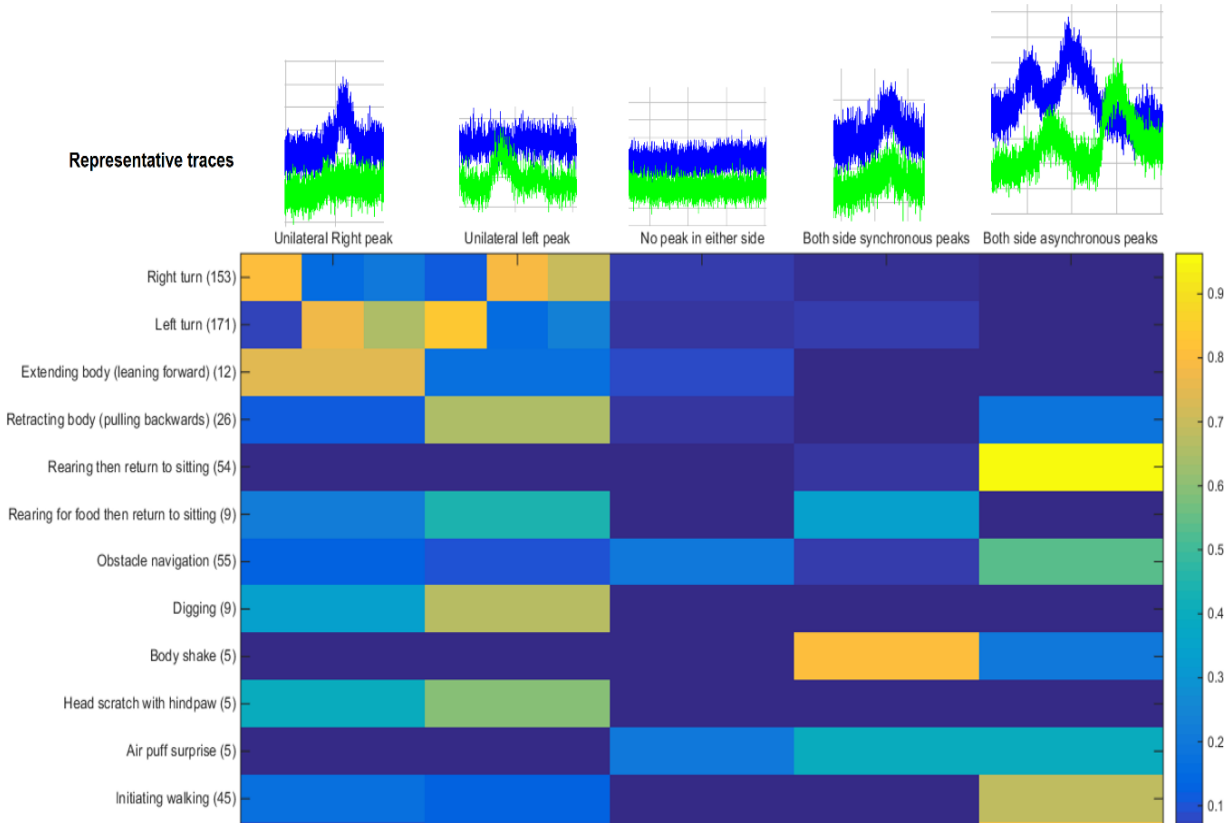

Figure 26. Synchronous and asynchronous behaviors correlate with different types of peaks. The blue recording represents the right striatum and the green recording represents the left striatum. We observed 13 different behaviors listed on the left side of the figure and 5 different types of neuronal synchrony shown on the top. We then calculated a heatmap based on how the behaviors correlated with the different categories of peaks.

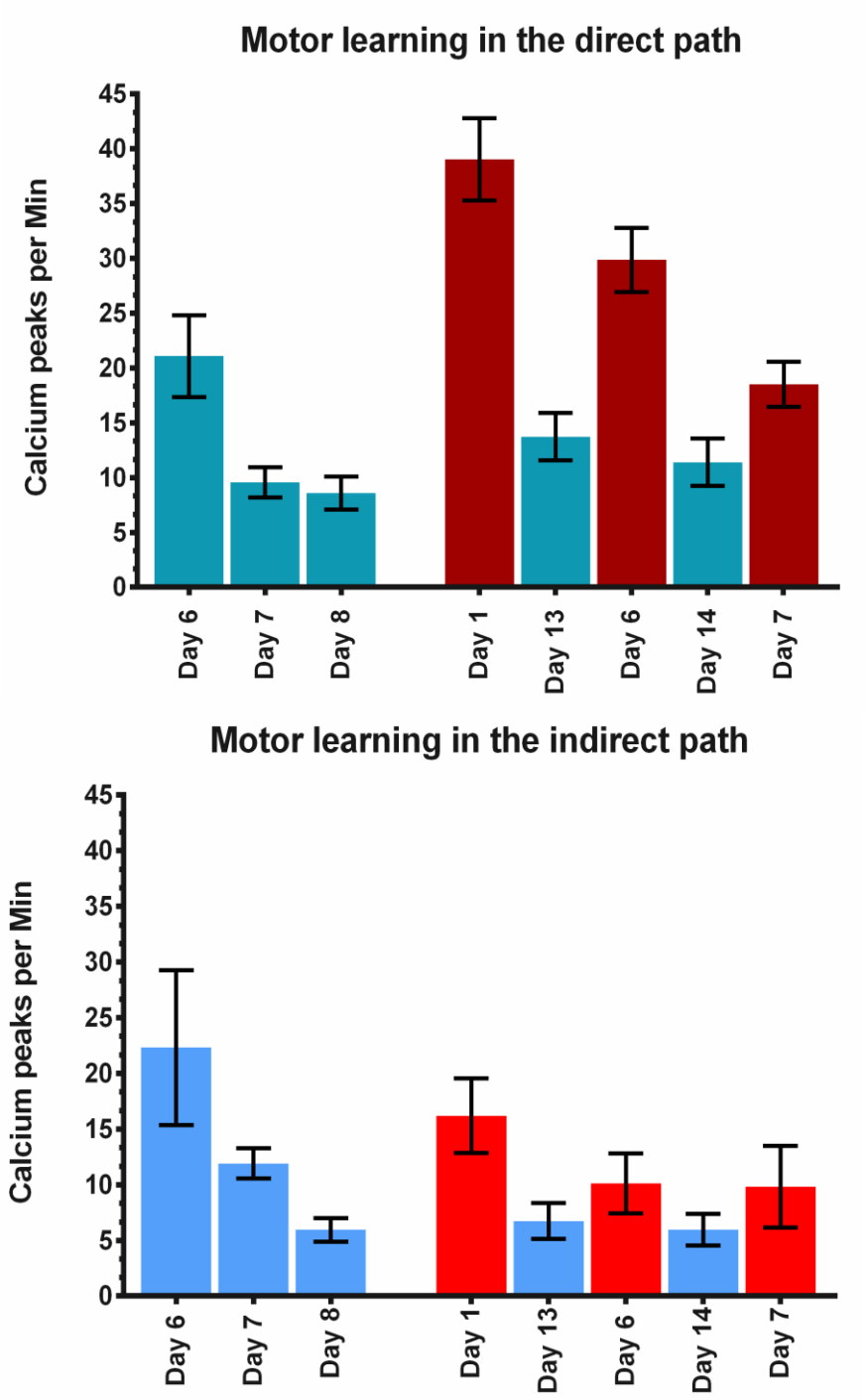

Figure 27. Treadmill motor skill learning in the direct and indirect paths. Top calcium peaks in the indirect path during forward walking show a decrease between day 6 and day 7 and this reduction is maintained throughout day 14 (two-way ANOVA P<.05). Calcium peaks during reverse walking (dark red) show a decrease from day 1 through day 7. Bottom: Calcium peaks in the indirect path during forward walking show a decrease between day 6 and day 7 and this reduction is maintained throughout day 14. Calcium peaks during reverse walking (dark red) show a decrease from day 1 through day 7. Forward and reverse walking were not done on the

Figure 28. Rotarod D1 (direct path) and A2A (indirect path) calcium peaks per minute. The number of peaks in the D1-Cre DMS mice showed a significant increase in direct path firing between day 1 and day 2, indicating increased recruitment of the associative path (Two tailed T test). The A2-Cre mice (DLS) showed a non-significant trend toward high activation of the indirect path on day 1 and reduced activation of the indirect path on day 2 indicating reduced activity in the sensorimotor path (Two tailed T test).

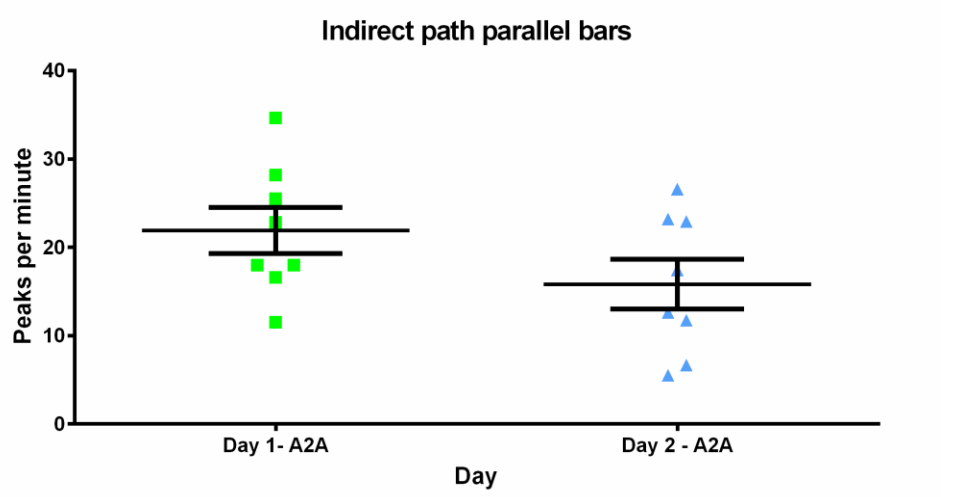

Figure 29. Parallel bars calcium peaks per minute A2A mice. The A2-Cre mice showed non-significant trend toward high activation on day 1 and reduced activation on day 2 indicating reduced activity in the sensorimotor path. Recorded from fibers implanted in the DLS. (Two tailed T test)

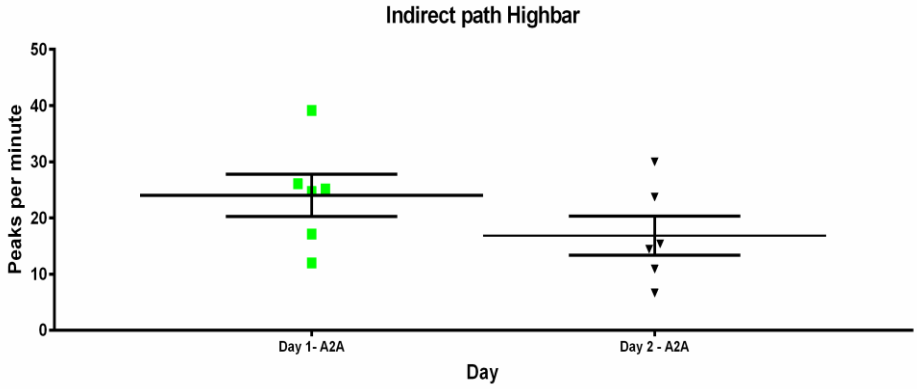

Figure 30. **Highbar peaks per minute in A2A mice.** The A2-Cre mice showed non-significant trend toward high activation on day 1 and reduced activation on day 2 indicating reduced activity in the sensorimotor path. Recorded from fibers implanted in the DLS. (Two tailed T test)

Discussion

This is to our knowledge the first evidence of synchronous and asynchronous activity between the right and left dorsal striatum, as determined by both amplitude and frequency of firing during goal oriented behaviors in mice (**Figure 26**). During the execution of motor patterns, unilateral peaks and bilateral asynchronous peaks were much more common than synchronous peaks. Unique behaviors were also correlated to unique co-ordination of firing between right and left hemispheres. Different behavioral patterns showed unique firing patterns suggesting recruitment of diverse neuronal populations. These findings would be consistent with recordings showing specific neurons are tuned to fire during specific parts of an action sequence and that neuronal activity is concatenated during motor learning (Jin et al. 2014).

This is also the first evidence that the firing rate of the dSPNs of the direct path significantly decreases during motor learning in the DLS on the treadmill (**Figure 27**). We also found a trend toward decreasing firing rate of the indirect path neurons in the DLS on the rotarod, parallel bars, and highbar (**Figures 28-30**). Similar to Kupferschmidt et al. (2017), we found that the DLS showed the highest activity at the start of motor learning and that this level of activity rapidly reduced over subsequent days of training. We also found that iSPNs in the DMS showed low activity on the first day of training that rapidly increased by the second day of training. However, the recordings in the DMS showed a trend towards increasing on the second day of learning on the rotarod that did not reach significance (**Figure 28**). This would be relatively consistent with the findings from the sensorimotor terminals from Kupferschmidt et al. (2017): however, while Kupferschmidt measured changes in the presynaptic corticostriatal neurons of the associative path projecting to SPNs in the DMS, and the corticostriatal neurons of the sensorimotor path projecting to neurons in the DLS, we were able to record from the next step in the circuit, the post synaptic SPNs of direct and indirect paths that comprise the associative and sensorimotor paths. We believe that this reduction in firing could be due to refinement of the populations of neurons that are involved during motor learning. This potential refinement could be explained by the neuronal ensemble hypothesis, that neuronal circuits undergo refinement during learning (Fingelkurts et al. 2004). This is supported by evidence showing specific neurons are active during different action sequences during motor pattern

learning (Jin et al. 2014). This is also supported by optical recordings showing that action sequences are encoded by specific neuronal ensembles (Klaus et al. 2017).

Our findings suggest that the presynaptic changes that have been shown to underlie the changes in the firing rate of the sensorimotor and associative path corticostriatal neurons likely control the firing rate of the postsynaptic SPNs in both the direct and indirect paths. There may be a potential common mechanism underlying these changes, but while we were able to record these changes in firing in vivo, we were not able to determine if these changes were due to pre- or postsynaptic alterations or a combination of both.

It is possible that DA and cannabinoid modulation plays an important role the changes in dSPN and iSPN firing that we observed. Previous studies have shown that DA changes in synaptic plasticity in corticostriatal and thalamostriatal synapses play a role in motor learning (Budzillo et al. 2017). DA and endocannabinoids control filtering in corticostriatal synapses and play a role in refining the information transmitted from the motor cortex to the striatal synapses. By mediating up and down state changes, DA also plays a direct role in the balance of direct and indirect path firing (Kreitzer 2009)

Future directions

We used a small number of experimental subjects as related in the Methods, and in future experiments, we plan to increase the number of mice sampled, which we likely allow these changes to reach significance. Now that the problems with the reverse light cycle room have been fixed (the light switches were deactivated), we plan to repeat the parallel bars, high bar, and rotarod for the full 7 days of motor training. Coordinated signaling by DA, glutamate, and endocannabinoids have been shown to play an important role in striatal plasticity (Wong et al. 2015). Long term depression of corticostriatal and thalamostriatal synapses was shown to be driven by retrograde transmission of endocannabinoids acting at CB1 receptors (Wong et al. 2015), and has been implicated in motor learning and action initiation (Jin and Costa 2015, Hilario and Costa 2008). We plan on using DA and cannabinoid antagonists during these tasks to investigate if they disrupt the firing rate of the dSPNs and iSPNs and to determine if they will impair motor skill learning.